A dissertation submitted for the degree of
Doctor of Philosophy

Numerical Simulations of Core-Collapse Supernovae in Massive Binary Systems

大質量連星系内での重力崩壊型超新星爆発に関する数値シミュレーション

February 2017

Ryosuke HIRAI

平井 遼介

Numerical Simulations of Core-Collapse Supernovae in Massive Binary Systems

大質量連星系内での重力崩壊型超新星爆発に関する数値シミュレーション

February 2017

Waseda University
Graduate School of Advanced Science and Engineering
Department of Pure and Applied Physics,
Research on Theoretical Astrophysics

Ryosuke HIRAI

平井 遼介

Abstract

Merger events of close compact binaries involving black holes and neutron stars have become one of the main focuses of astrophysics in the last few years. Especially the detection of gravitational waves from a binary black hole by LIGO has accelerated the progress. Thus it is important to understand the formation mechanism of such systems, which is poorly understood compared to the merger process itself. The "standard" theory for the formation of close compact binaries is that a massive binary system survives two supernova explosions and also shrinks its orbit via a common envelope phase. There are many obstacles to finally become a close compact binary. One of them is how to successfully eject the envelope in the common envelope phase. A system will merge prior to supernova if they cannot eject the envelope. Another obstacle is how to survive the impact of the two supernova explosions. A binary system will disrupt if more than half of the mass is lost by the explosion. Mass transfer or common envelope episodes can help decrease the ejecta mass before the explosion, but on the other hand neutron star kicks or the impact of supernova ejecta colliding with the companion can help disrupt the binary by introducing extra momentum or mass stripping off the companion.

In this thesis I study the impact of supernovae in massive binaries and what we can learn from their observations using various numerical simulations. We first carried out two dimensional hydrodynamical simulations to explore the largest possible impact of supernova ejecta hitting the companion star in a massive binary. Assuming a red supergiant model as the companion, we simulated the so-called "ejecta-companion interaction" and calculated the amount of unbound mass and the momentum given to the star. As a result we found that $\sim 25\%$ of the mass may become unbound due to the heat excess injected to the star by shock heating when placed close as possible to the exploding star. This is large enough to help disrupt binaries which will have otherwise survived without the mass stripping. The kick velocity was comparable to the orbital velocity, which will also help destroy the system. The effects becomes smaller as we increased the separation. We also revealed that the unbound mass is strongly correlated to the impact density, and proposed a simple model that may explain the physics of the mass stripping process.

Then we applied our numerical procedure to a more realistic binary system that may represent the progenitor of a specific supernova iPTF13bvn. We first carried out binary evolution calculations to construct binary models consistent with observational constraints, and performed two dimensional hydrodynamical simulations of the ejecta-companion interaction again. Due to the wide separation and compact nature of the main sequence star compared to red supergiants, the unbound mass and induced momentum was negligible. Although this is not large enough to alter the further evolution of the binary, we found out that the shock heating may puff up the companion star to noticable radii, lowering the surface temperature.

Latest observations could not find such a puffed up companion nor any of the predicted companion models. We therefore carefully re-assessed the observational constraints and all evolutionary scenarios proposed so far. We found that the current favourite common envelope model does not seem to explain the formation of the progenitor well. Instead, the progenitor of iPTF13bvn may have been a binary with a massive black hole component. Future observations may be able to distinguish between the models.

We are further planning to carry out systematic studies of ejecta-companion interaction in general cases. We have studied methods to accelerate self-gravitational hydrodynamic simulations that will make these systematic studies possible.

Contents

"If I have seen further than others, it is by standing upon the shoulders of giants."
Isaac Newton (1643–1727)

1
Introduction

1.1 Binary Stars: The Astrophysical "Binoculars"

Ever since its discovery, binary systems (or "double stars") have always been in the forefront of astronomy and observational technologies. Mizar (ζ Ursae Majoris) was probably the first known double star, discovered by Galileo's colleague Benedetto Castelli on January 15th 1617, just a few years after the invention of the telescope[1] (Dick, 2013). This system was discovered directly by resolving both of the stars, which is now called "visual" binaries. Castelli discovered another double star in Monoceros in the same month, and in the same year Galileo discovered a triple system in the Trapezium of Orion, later confirmed by Huygens and Herschel. Many more double stars were found in the following century, but mostly by accident during searches for other objects. It was still hard to distinguish whether the two stars are simply just aligned on the line of sight or really physically related to each other, although John Michell pointed out in 1767 that the probability of them being physically connected should be high (Michell, 1767). William Herschel was one of the first to observationally confirm the physical bond and recognized these systems as a new class, and he gave the name "binary star" in his catalogue of double stars (Herschel, 1802). This had motivated many astronomers to look for more binary stars, and thousands of systems were discovered in the following century using the most advanced optical telescopes in those days.

As our knowledge in physics and the available observational devices advanced, many other methods were developed to find binaries. In 1889, Edward Charles Pickering used the spectroscope and found that some of the spectral lines of ζ Ursae Majoris (Mizar) periodically splitted into two lines. This was associated with the orbital motion in a binary, being the first "spectroscopic" binary to be discovered. Soon after, this new method was used to observe a known variable star Algol (β Persei), and it was confirmed to be a close binary eclipsing each other. This was not only the second

---

[1] The discovery of the double star used to be attributed to an Italian astronomer Jean Baptiste Riccioli (Aitken, 1918), but it is now debated whether he even did find a double star.

spectroscopic binary, but the first "eclipsing" binary to be found. Spectroscopy has greatly improved our ability in finding binaries, and it has also dramatically increased the amount of information we can obtain from observation.

The advent of X-ray astronomy revealed the existence of yet another class of binary systems named "X-ray binaries". The X-ray emission was thought to come from the accretion of matter from a companion star onto a compact stellar object such as neutron stars and black holes. One of the most well studied X-ray binaries Cygnus X-1, discovered in 1964, has now provided us a strong support for the existence of black holes. In the meanwhile, radio astronomy was developing rapidly too, and led to the discovery of stars emitting periodic pulses, namely, pulsars. Pulsars were later known to be rotating magnetized neutron stars. In 1974, Russell Alan Hulse and Joseph Hooton Taylor Jr. found that the arrival time of the pulses from the pulsar PSR1913+16 had periodic variations, and concluded that it was due to the presence of another pulsar orbiting it (Hulse and Taylor, 1975). This famous "Hulse-Taylor binary" was carefully observed for a long period, and led to the indirect confirmation of gravitational waves. The presence of a companion is useful to make very accurate measurements of the mass. Some famous neutron stars had precisely measured masses beyond previous expectations ($\sim 2\mathrm{M}_\odot$), and placed very strong constraints on dense matter physics (Demorest et al., 2010; Antoniadis et al., 2013).

Gravitational wave astronomy is now the current forefront on the search of new classes of binaries. On 11th February 2016, the LIGO team announced that they detected gravitational waves from the coalescence of a binary black hole (Abbott et al., 2016c). There were two confirmed gravitational wave events within their ~ 4 month operation (GW150914 and GW151226), both of which were mergers of black holes with masses $\sim$ 10–30$\mathrm{M}_\odot$ (Abbott et al., 2016c,b). Black holes in this mass range were not known before, and raised new problems to their astrophysical origin (Abbott et al., 2016a). The waveforms of the merger events themselves can be used to validate or refute various gravitational theories. LIGO and other gravitational wave detectors which are planned to operate in the future (e.g. Virgo, KAGRA, LIGO-India) are expected to detect more of these events and also hoped to find binary neutron star or neutron star-black hole binary mergers too.

Apart from individual observations, surveys of whole populations of binaries can also provide us valuable information through their statistical properties such as multiplicity fractions or distributions in mass, period, eccentricity etc. There have been many kinds of surveys carried out so far, with different sizes, methods, targets, aims. Petrie (1960) surveyed 1752 stars of spectral type B, A, F and M and found that roughly half of the stars had variable radial velocities regardless of their mass. Only the relatively close and inclined binaries have observable radial velocities, so the intrinsic binary fraction should be higher, and Poveda et al. (1982) argued that all stars have a companion if we take into account wide binaries. Some systems were known to have tertiary or even more companions, and several surveys were carried out to investigate the fraction of these higher order multiple systems (Duquennoy and Mayor, 1991; Tokovinin, 1997, 2014; Fuhrmann and Chini, 2015). According to the recent results, roughly a third of binary stars are in higher order multiple systems[2], mainly triple. An important feature is the difference in multiplicity and binary parameter distributions

---

[2] The fraction of systems with $n = 1, 2, ...$ components were 55:33:8:4:1 for F/G stars (Tokovinin, 2014).

Table 1.1: Summary of recent multiple fraction measurements.

Spectral type	Mass[1]($M_\odot$)	Multiple fraction	Reference
Brown dwarf	0.02–0.04	$< 11\%$	Garcia et al. (2015)
	< 0.1	$\sim$ 10–30%	Burgasser et al. (2007)
M dwarf	0.04–0.45	21–27%	Janson et al. (2014)
	0.12–0.59	26–38%	Bergfors et al. (2010)
	0.15–0.67	26–31%	Ward-Duong et al. (2015)
	0.12–0.70	24–30%	Janson et al. (2012)
G dwarf	0.90–1.10	42–46%	Raghavan et al. (2010)
A dwarf	1.7 –7	70–100%	Kouwenhoven et al. (2005, 2007)
B star	3–16	15–61%	Chini et al. (2012)
O star	> 16	$> 82\%$	Chini et al. (2012)
	> 16	$\sim 100\%$	Sana et al. (2014)

[1] Where there were no mentions on the mass in the original paper, we have converted the spectral type to mass using Table 5 of Kraus and Hillenbrand (2007).

among different masses of stars. In Table 1.1 I have summarized results of some of the recent surveys on stellar multiplicity. A clear trend of the multiple fraction on mass can be seen. It should be noted that heavier stars have higher binary fractions, and tend to have more companions. These facts could imply something on their formation scenarios or even evolution models since binaries can be destroyed on the course of their evolution. Mass ratio distributions also seem to have mass dependences, and some studies suggest that it could be explained by a flat mass ratio distribution in total mass (Goodwin, 2013). However, the distributions of binary parameters (mass ratio, period, eccentricity etc) should be treated carefully, since there is not enough data and many observational biases exist. Future surveys are expected to resolve these problems and give us precise distributions of parameters, and even their age and/or environmental dependences. Especially the *Gaia* mission is anticipated to discover ~30 million binaries, which will dramatically increase the amount of data available (Gaia Collaboration, 2016; Eyer et al., 2013). Just like X-ray, radio, gravitational wave astronomy had opened new windows in the binary field, big data is now our new window.

As we have seen here, the improvement in observational instruments and techniques have always led to discoveries of new classes of binaries and at the same time raised new problems and interests. On the other hand, we have also seen that binary stars can be used as a useful laboratory to unravel the mysteries of nuclear physics, gravitational physics, stellar astrophysics etc. We are using telescopes to seek for binaries, but at the same time using binaries to probe the secrets of nature. In particular, the binaries containing compact objects have lots to tell us. It is thus very important to understand the nature of binaries. However, many aspects of the nature of binaries are still very abstract, including their formation, evolution and death. In the following sections I will briefly review current establishments on binary evolution theory and the motivations of my work.

1.2 Stellar Evolution

The theory of stellar structure and its evolution is considered to be well established compared to other fields in astrophysics. Although this is not totally correct, it is true that current stellar evolution theory can explain many of the observed aspects to some extent. Here I will briefly review the standard theory (Kippenhahn and Weigert, 1990; Eggleton, 2011).

1.2.1 Single Stars

The main information we can obtain from observing stars is the flux (brightness, magnitude) and the spectrum (colour). If one can infer the distance to the star by using other techniques (e.g. parallax), we can calculate the stars absolute magnitude or luminosity from the apparent magnitude. The spectrum can be used to infer the surface effective temperature, and if the resolution is high enough, the chemical composition. In order to compare theoretical models with observation, it is customary to describe the evolution of stars using tracks on the so-called “Hertzsprung-Russel diagram (HR diagram)” or “colour-magnitude diagram”. A usual HR diagram takes the effective temperature in the horizontal axis and the luminosity in the vertical axis, as a log-log plot. On the other hand, a colour-magnitude diagram takes the colour (e.g. B-V) for the horizontal axis and apparent magnitude for the vertical axis. Both diagrams are used for similar purposes, but the latter is easier to plot and often used by observers. One of the interesting features of an HR diagram is that when you plot all stars in an observed cluster, the majority of the stars lie on a diagonal strip running from the bottom right towards the upper left. Stars which lie on this strip are called “main sequence” stars. On the other hand, there are stars that are off the main sequence, in various areas on the HR diagram, given different names according to the location. It is now known that each position on the HR diagram corresponds to different evolutionary stages of a star. In modern observationary studies it is a natural procedure to infer the age and mass of stars using the position on the HR diagram. Thus it is important to understand this correspondence.

The formation of stars is thought to be initiated by the gravitational collapse of gas clouds. This starts at the right end of the HR diagram, just outside the so-called “forbidden zone” (Hayashi, 1961). The cloud will contract down the “Hayashi track”, vertically in the HR diagram. For stars with masses $> 0.5\mathrm{M}_\odot$ it will eventually bend to the left on the “Henyey track”. Once the central density and temperature reaches high enough values, it will start burning hydrogen. It is also suggested that the cloud cores can fragmentate during the collapse and this may be the seeds of binary systems (reviews by Bodenheimer et al., 2000; Goodwin et al., 2007). Although the details of star formation are still not well understood, the stellar structure after hydrogen ignition is in a rather “clean” state and does not depend on the formation process. Stellar evolution studies mainly take this point as the initial condition and call it “zero age main sequence (ZAMS)”. In Fig.1.1 the grey dotted line indicates the location of ZAMS stars on the HR diagram.

The nuclei that can be burned depend strongly on the density and temperature of the matter. Since the burning criteria are distinct among nuclei due to the well separated energy levels, the evolutionary stages of stars can be roughly separated

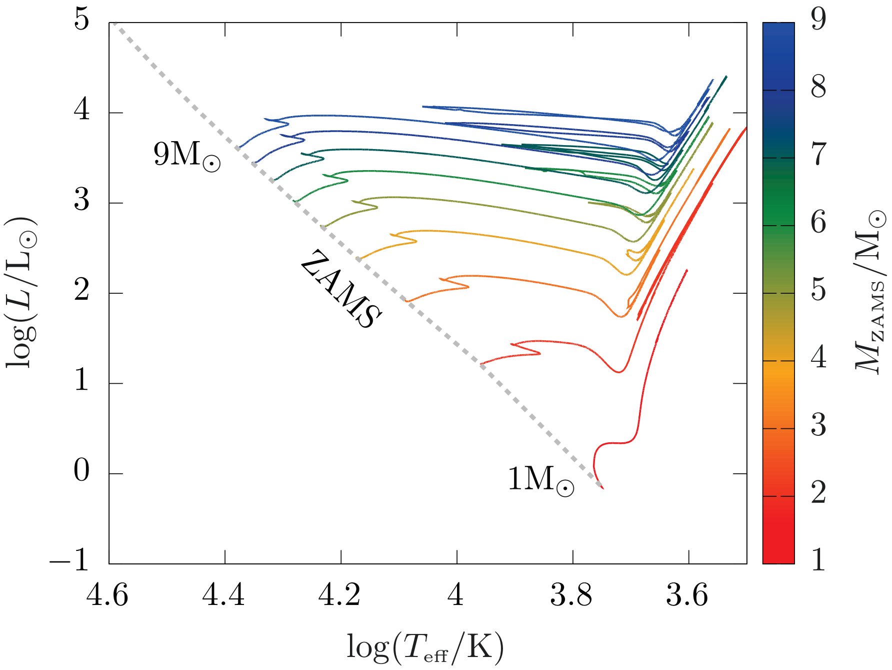

Figure 1.1: Evolutionary tracks of solar metallicity stars with various masses. Dashed line indicates the main sequence. Calculations were carried out using `MESA`.

according to the type of nuclei being burned. The first stage is the hydrogen burning stage, in which hydrogen is fused into helium via the CNO cycle or pp chains. This stage is the main sequence stage, and is the most long-lasting phase in stellar evolution (e.g. $\sim 10^{10}, 10^{8}, 10^{7}$yr for $1, 3, 10\mathrm{M}_\odot$ stars respectively). Stars slowly evolve to the upper right during the main sequence as we can see in Fig.1.1. Towards the end of the main sequence, the track abruptly moves to the left, creating a "hook" feature. This occurs when the central hydrogen abundance is $X_\mathrm{H} \sim 0.05$, and only lasts $\sim$ 3–5% of the whole hydrogen burning timescale.

When the central hydrogen content is depleted, there is no longer any energy generation at the centre, and the hydrogen fusion takes place off the centre. In this phase there is an isothermal helium core surrounded by a hydrogen envelope that is burning fuel at the bottom shell-like region. This phase is called the "hydrogen shell burning" phase, and the envelope rapidly expands on a thermal timescale while the core contracts. Stars can expand up to $\sim$ 10–100 times its original radius, moving to the far right in the HR diagram. The expansion is so rapid compared to the other stages in their evolution, that there is a significant deficiency of observed stars in this stage. This deficiency is called the "Hertzsprung gap".

Low-mass stars ($\lesssim 2\mathrm{M}_\odot$) will simply contract and eventually be supported by electron degeneracy. Heavier stars will ignite helium before becoming degenerate, entering the red giant phase. A red giant star has a deep convective envelope and evolves along the Hayashi track, following complicated paths depending on the implemented physics. It is during this expansion that most binary interactions take place that I will discuss in the next section. Massive stars with masses $\gtrsim 8\mathrm{M}_\odot$ will burn heavier elements such as C, O, Ne, Mg, Si at the centre after the helium burning phase. The elements that can be burned depend on the stellar mass, but no nuclear fusion process can create elements heavier than Fe. By this time the core will have a stratified structure of each element, and because the energy production at the centre ceases after the creation of Fe, the pressure support will disappear, leading to core-collapse.

1.2.2 Binary Interactions

The previous subsection was a general overview of the evolution of an isolated single star. However, we already know that the majority of stars are members of binary or higher order multiple systems, and the evolution of such stars can be significantly different from that of single stars. Especially for massive stars that cause core-collapse supernovae, almost $\sim 100\%$ of them are members of binaries and $\sim 70\%$ of them are expected to interact during their lifetimes (Sana et al., 2012). It is therefore important to know what kinds of binary interactions there are and how they can affect the evolution of each star and the system.

An important framework when discussing binary interactions is the "Roche potential" (Roche, 1873; Kopal, 1959; Kruszewski, 1966; Eggleton, 2011). Let us consider a system corotating with a binary system with component masses M_1 and M_2. One can express the force $\boldsymbol{f}$ acting on a test particle at $\boldsymbol{x}$ in this system by

$$\boldsymbol{f} = -\nabla\phi_R \tag{1.1}$$

$$-\phi_R = \frac{GM_1}{|\boldsymbol{x}-\boldsymbol{x_1}|} + \frac{GM_2}{|\boldsymbol{x}-\boldsymbol{x_2}|} + \frac{1}{2}|\boldsymbol{\omega}\times\boldsymbol{x}|^2 \tag{1.2}$$

where $\boldsymbol{\omega}$ is the angular velocity of the binary orbit, and $\boldsymbol{x_1}, \boldsymbol{x_2}$ are the positions of the centre of the stars. ϕ_R is an effective potential of the combined force of gravity and centrifugal forces. In Fig.1.2 I show a plot of the Roche potential of a binary with a mass ratio $q \equiv M_2/M_1 = 0.3$. Contour lines are drawn at the bottom. The two large holes are the gravitational potential wells of the stars, but as you get away from the stars the potential drops because the centrifugal forces dominate. There are several features in this potential which are of particular importance. As they are clear from the figure, there are five points where the forces balance and there is no acceleration to the particle. These points are named "Lagrangian points" and each of them has different roles.

L_1: The *first* Lagrangian point is located between the stars, on the line connecting the centres of the two bodies. The equipotential surface containing the L_1 point is called the "Roche lobe"[3]. The Roche potential takes a saddle shape around this point.

L_2: The *second* Lagrangian point is also on the line connecting the two bodies, but on the other side of the smaller mass star from the heavier star. The Roche potential takes a saddle shape again here. This point usually decides the radius of a circumbinary disc.

L_3: The *third* Lagrangian point is also on a saddle point collinear with the first and second Lagrangian points, but on the other side of the heavier star from the secondary.

---

[3] Not to be confused with the Roche sphere and Roche limit. All have different definitions.

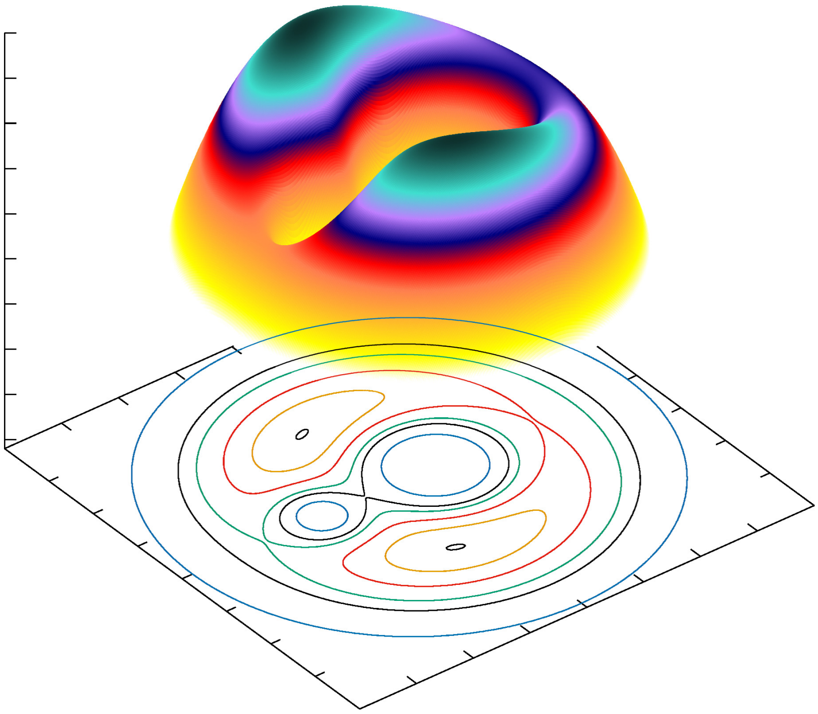

Figure 1.2: Shape and contours of the Roche potential for a binary with mass ratio $q = 0.3$.

L$_4$ & L$_5$: The *fourth* and *fifth* Lagrangian points are on the two hilltops of the Roche potential, and the distances to the two bodies are the same as the orbital separation. They are sometimes referred to as Trojan points, and are known to be conditionally stable. Many asteroids have been observed on the Trojan points of the Sun-Jupiter system.

In Fig.1.3 I have shown the locations of the Lagrangian points in the same system as in Fig.1.2. The thick black contour containing the L$_1$ point is the equatorial section of the Roche lobe. The Roche lobe takes a tear-drop shape, and decides the gravitationally bound region of the two bodies. A binary system is stable as long as the components reside within their Roche lobes. Once one of the stars starts expanding at advanced stages of their evolution, it may be possible that the stellar radius exceeds the size of their Roche lobes. When a stars overfills its Roche lobe, a part of the envelope can be transferred to the companion through the first Lagrangian point[4]. This form of binary interaction is called “Roche lobe overflow (RLOF)”, and can drastically alter the evolution of the stars and the system.

The rate of mass transferred by RLOF is one of the key factors that determines the evolution of a binary. In some of the first computations of binary evolution, the star was assumed to always reside inside their Roche lobes (Morton, 1960; Paczyński, 1966). This can simply be expressed by

$$R = R_{\rm RL} \tag{1.3}$$

$$\dot{R} = \dot{R}_{\rm RL} \tag{1.4}$$

---

[4] The critical lobe that determines the onset of mass transfer does not necessarily need to coincide with the Roche lobe (Paczyński and Sienkiewicz, 1972). Here we will simply assume that the critical lobe is the same as the Roche lobe.

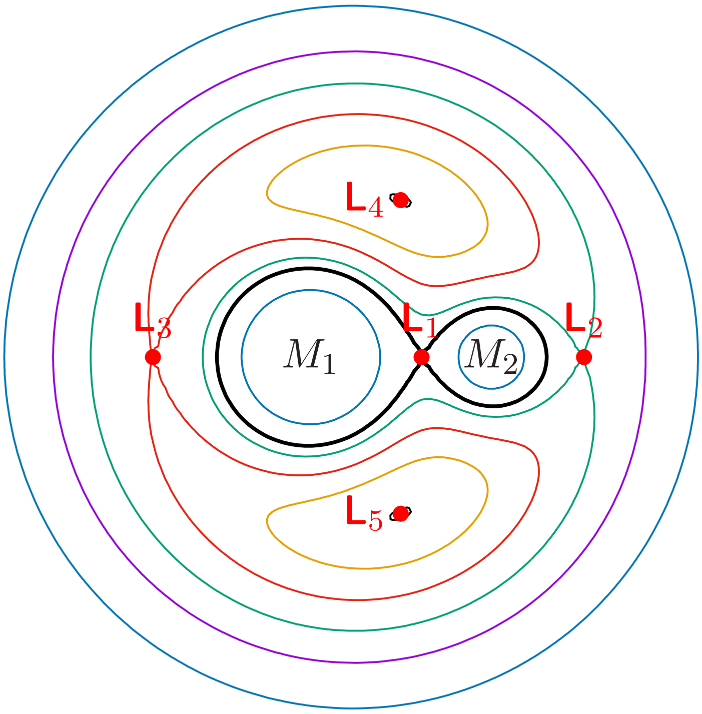

Figure 1.3: Contour of the Roche potential and the Lagrangian points.

where R is the radius of the star and R_{RL} is the effective radius of the Roche lobe. However, this assumption was only applicable if the donor star had a steep surface, i.e. the pressure scale height was sufficiently smaller than the stellar radius $H_p/R \ll 1$, and the mass transfer is (quasi-)stationary, i.e. $\ddot{M}_1 \approx 0$. Not all stars have well defined sharp rims, and the mass transfer is not stationary at all times. For example, the first mass transfer phase takes place when the heavier star evolves to its helium burning phase. When mass starts to be transferred to the companion, the Roche lobe radius will shrink due to the change in mass ratio, whereas the radius expands, so the stellar radius will exceed its Roche lobe. For this reason many studies have been carried out to derive more general expressions for the mass transfer rate (Paczyński and Sienkiewicz, 1972; Plavec et al., 1973; Lubow and Shu, 1975; Savonije, 1978; Meyer and Meyer-Hofmeister, 1983; Ritter, 1988; Kolb and Ritter, 1990).

The underlying ideas are similar among the works, assuming some sort of flow through the vicinity of the L_1;

$$-\dot{M}_1 = \int_F \rho_{\mathrm{L}_1} v_s dA \tag{1.5}$$

where F is the small intersection around the L_1 point perpendicular to the line connecting the centres of stars. The radius of this intersection is usually taken as $\approx H_p$. ρ_{L_1} and v_s are the density and sound speed of the flow through the nozzle F. The values for ρ_{L_1} and v_s are evaluated by using Bernoulli's theorem along the streamline through the L_1 point.

$$\frac{1}{2}v_0^2 + \Phi_0 = \int_E^{\mathrm{L}_1} \frac{dP}{\rho} + \frac{1}{2}v_{\mathrm{L}_1}^2 + \Phi_{\mathrm{L}_1} \tag{1.6}$$

where v is velocity, Φ is the Roche potential and the subscripts 0 and L_1 denote a point E sufficiently far away from L_1 ($v_0^2 \ll v_s^2$) and the L_1 point respectively.

In the earlier works (Paczyński and Sienkiewicz, 1972; Plavec et al., 1973; Savonije, 1978; Edwards and Pringle, 1987) the flow is assumed to be adiabatic, and use a polytropic approximation for the surface layers[5]. Since the local sound speed and density structure can be easily computed for polytropes, the mass transfer rate can be derived as a function of the polytropic index by taking the integration in Eq.1.6 over the surface layer of a polytrope sphere. Many modern stellar evolution codes employ the prescriptions by Kolb and Ritter (1990) in which they do not use a polytropic approximation but use the structure of the actually computed star. The formula of their mass transfer rate is separated into two parts;
1) optically thin mass transfer ($R \leq R_{\mathrm{RL}}$),

$$-\dot{M}_1 = \dot{M}_0 \exp\left\{-\frac{R_{\mathrm{RL}} - R}{\hat{H}_p}\right\} \tag{1.7}$$

$$\dot{M}_0 = \frac{2\pi}{\sqrt{e}} F_1(q) \frac{R_{\mathrm{RL}}^3}{GM_1} \left(\frac{\mathcal{R}T_{\mathrm{eff}}}{\mu_{\mathrm{ph}}}\right)^{\frac{3}{2}} \rho_{\mathrm{ph}} \tag{1.8}$$

$$F_1(q) = q f_1^{-3}(q) \{g(q)[g(q) - 1 - q]\}^{-1/2} \tag{1.9}$$

$$g(q) = \frac{1}{x_{\mathrm{L}}^3} + \frac{1}{(1 - x_{\mathrm{L}})^3} \tag{1.10}$$

$$f_1(q) = \frac{R_{\mathrm{RL}}}{a} \tag{1.11}$$

$$\hat{H}_p = H_p / \gamma(q) \tag{1.12}$$

$$H_p = \frac{\mathcal{R}T_{\mathrm{eff}} R_{\mathrm{RL}}^2}{GM_1 \mu_{\mathrm{ph}}} \tag{1.13}$$

where $q = M_1/M_2$ is the mass ratio, a is the separation, $x = (x_{\mathrm{L}}, 0, 0)$ is the position of the L_1 point and $\gamma(q)$ is a factor that accounts for the non-sphericity of the Roche equipotential surface

$$\begin{aligned} \gamma(q) &= 0.954 + 0.025 \log q - 0.038 (\log q)^2, \quad 0.04 \lesssim q \lesssim 1 \\ \gamma(q) &= 0.954 + 0.039 \log q + 0.114 (\log q)^2, \quad\quad 1 \lesssim q \lesssim 20 \end{aligned} \tag{1.14}$$

We have assumed that the donor star is the primary star.
2) optically thick mass transfer ($R > R_{\mathrm{RL}}$)

$$-\dot{M}_1 = \dot{M}_0 + 2\pi F_1(q) \frac{R_{\mathrm{RL}}^3}{GM_1} \int_{\Phi_L}^{\Phi_{ph}} F_3(\Gamma_1) \left(\frac{\mathcal{R}T_0}{\mu_0}\right)^{\frac{1}{2}} \rho_0 d\Phi \tag{1.15}$$

$$F_3(\Gamma_1) = \Gamma_1^{1/2} \left(\frac{2}{\Gamma_1 + 1}\right)^{\frac{\Gamma_1 + 1}{2(\Gamma_1 + 1)}} \tag{1.16}$$

$$\Gamma_1 = \left(\frac{\partial \ln P}{\partial \ln \rho}\right)_{\mathrm{ad}} \tag{1.17}$$

---

[5] Jędrzejec should be credited for the derivation of mass transfer rates using the polytropic approximation. All works are based on his master thesis in 1969.

The optically thin part enables the mass transfer rate to switch on and off smoothly, and also sometimes dominates the whole mass transfer (see Ritter, 1988). It should be noted that the Roche lobe radius $R_{\rm RL}$ used in the above expressions is usually the volume-equivalent radius because the shape of the Roche lobe is not a perfect sphere. It expresses the radius of a sphere that has the same volume as the volume of the Roche lobe. The value can be approximated by (for the primary lobe)

$$\frac{R_{\rm RL}}{a} = 0.38 + 0.2\log q \qquad (0.2 < q < 20) \tag{1.18}$$

$$\frac{R_{\rm RL}}{a} = \frac{2}{3^{4/3}}\left(\frac{q}{1+q}\right)^{1/3} \qquad (0 < q < 0.8) \tag{1.19}$$

within $\sim 2\%$ (Paczyński, 1966, 1971), or by

$$\frac{R_{\rm RL}}{a} = \frac{0.49q^{2/3}}{0.6q^{2/3} + \log(1+q^{1/3})} \tag{1.20}$$

within $\sim 1\%$ over the entire range of mass ratio (Eggleton, 1983).

The stability of the mass transfer should also be discussed to understand the mass transfer rate. There are several timescales that govern the mass transfer. It mostly depends on how the star retains equilibrium after the surface layer is removed from a star. Once the mass removal takes the star out of equilibrium it will first try to retain equilibrium on a dynamical timescale, and then relaxes on a thermal (or Kelvin-Helmholtz) timescale. On the course, the star will grow (expand) or shrink in response. The sizes of the Roche lobes also change due to the change in mass ratio. If the star remains enclosed in the Roche lobe after the small mass removal, the mass transfer will be stable, and the mass transfer process will proceed on the longer timescale in which it initiated (e.g. nuclear or gravitational wave). However, if the growth of the stellar radius exceeds that of the Roche lobe, the mass transfer will be unstable and the instability will grow on dynamical or thermal timescales. This may lead to stellar mergers or the so-called "common envelope phase" which I will discuss in detail in Section 4.4.1.

Stability criteria can be discussed by checking the mass-radius relations. We should compare the response of the radius by different processes in changing mass. The following exponents are commonly used (Webbink, 1985; Soberman et al., 1997; Tout et al., 1997).

$$\zeta_{\rm ad} \equiv \left.\frac{\partial \ln R}{\partial \ln M_1}\right|_{\rm ad} \tag{1.21}$$

$$\zeta_{\rm eq} \equiv \left.\frac{\partial \ln R}{\partial \ln M_1}\right|_{\rm eq} \tag{1.22}$$

$$\zeta_{\rm L} \equiv \frac{\partial \ln R_{\rm RL}}{\partial \ln M_1} \tag{1.23}$$

$\zeta_{\rm ad}$ expresses the radial response to adiabatic mass loss i.e. the chemical abundance and entropy profiles are assumed to be constant upon the mass removal. $\zeta_{\rm eq}$ is the radial response assuming that the star is in thermal equilibrium. $\zeta_{\rm L}$ is the change in the Roche lobe radius due to the change in mass ratio. In order to maintain stability,

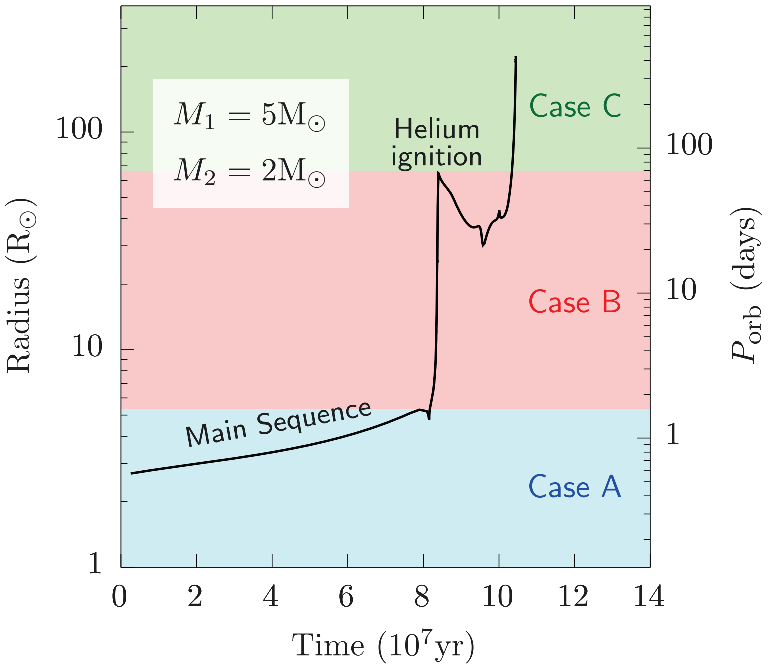

Figure 1.4: Radial evolution of a $5\mathrm{M}_\odot$ star. The corresponding regions of primary radius for different cases of mass transfer are colour shaded. The right axis is the orbital period of a binary that will start RLOF at that radius assuming a $2\mathrm{M}_\odot$ companion. (Similar to Figure 1 in Paczyński (1971).)

the star needs to shrink faster than the Roche lobe. Thus if $\zeta_{\mathrm{L}} < (\zeta_{\mathrm{ad}}, \zeta_{\mathrm{eq}})$ is satisfied, the mass transfer will be stable and proceed on the nuclear timescale. If $\zeta_{\mathrm{ad}} < \zeta_{\mathrm{L}}$ it will proceed on a dynamical timescale and lead to non-conservative mass transfer. If $\zeta_{\mathrm{eq}} < \zeta_{\mathrm{L}} < \zeta_{\mathrm{ad}}$ the mass transfer will proceed on the thermal timescale.

Which timescale governs the mass transfer depends strongly on the evolutionary stage of the star. Kippenhahn and Weigert (1967) classified the mass transfer process according to the stage in which RLOF initiated (see also Lauterborn, 1970, for English explanations), as below

case A: Mass transfer during central hydrogen burning (on the main sequence)

case B: Mass transfer after core hydrogen burning but before helium ignition (Hertzsprung gap)

case C: Mass transfer after helium ignition (giant branch)

Fig.1.4 illustrates the different cases of mass transfer for a $5\mathrm{M}_\odot$–$2\mathrm{M}_\odot$ binary. The orbital period needs to be less than ~ 1.5 days in order to experience case A mass transfer. Roughly only $\sim 10\%$ of the binaries are included in this case. On the other hand, the number of binaries that experience Case B or Case C mass transfer are roughly $\sim 45\%$ each. Case B mass transfer is sometimes further divided into two stages; cases Br and Bc depending on whether the envelope is radiative or convective (Eggleton, 2011; Vanbeveren et al., 2012). Case Br is roughly the left half of the Hertzsprung gap and case Bc the right half. In general, the mass transfer rate can become very large for case A/Br mass transfer, occuring on a thermal timescale. It will not stabilize unless the mass ratio is inverted and then it will proceed on the nuclear timescale. Case Bc/C mass transfer is unstable, and is considered to lead to common envelope phases. There are also possibilities that there are several episodes of mass transfer in the same binary. When case A mass transfer is followed by a case B mass transfer, it is called case AB (Ziółkowski, 1969; Horn, 1971). It is also possible that an almost naked helium star that had lost its envelope via case B mass transfer will fill its Roche lobe again during the helium burning stage. This two-stage mass transfer is called case BB (De Greve and De Loore, 1977; Delgado and Thomas, 1981). There is also a minor case where case A is followed by case C, called case BC (De Loore and Doom, 1992).

In more simplified evolution calculations, such as in population synthesis studies, the integration in Eq.1.15 cannot be computed because they do not solve stellar structures. Instead, they use a much more simplified form that does not take into account the structure of the envelope (Hurley et al., 2002). The rate is given by

$$\dot{M}_1 = F(M_1)\left[\ln\left(\frac{R}{R_{\rm RL}}\right)\right]^3 \mathrm{M_\odot yr^{-1}} \tag{1.24}$$

$$F(M_1) = 3\times10^{-6}[\min(M_1, 5.0)]^2 \tag{1.25}$$

when the mass transfer is stable.

These mass transfer rates are not known whether they express nature well. It becomes even more complicated if the orbit is eccentric, and we do not even know whether the mass transfer is conservative or not[6]. The evolution of systems in contact are also unknown although they are known to exist. There are also other binary effects besides RLOF, such as tidal interactions, orbital shrinking by gravitational waves, wind accretion, magnetic braking, supernovae and so on, all of which contain large uncertainties in our current understandings. It is still difficult to extract information on binary evolution directly from observations due to its long timescale compared to our lifetimes. Thus it is common to study binary interactions qualitatively by “population synthesis”. They use simple parametrized evolution models to calculate the evolution of millions of binaries. The final distribution of various quantities can be compared with observed distributions and used to calibrate the value of parameters. However, there are too many parameters that can be varied, so there is always a degeneracy between them. Much more fundamental work is required to understand binary interaction processes.

1.3 Supernova

1.3.1 Classification of Supernovae

Supernovae are one of the most energetic explosions in the universe. They are classified into several types according to their spectral features (Filippenko, 1997). The starting point is whether they show hydrogen features in their spectrum. All supernovae which lack hydrogen are called “Type I”, and those which do show hydrogen features are

---

[6] There are some possible evidence of non-conservative mass transfer from recent observations (Maeda et al., 2015).

"Type II". This distinction was first noticed by Minkowski (1941), based on many other features as well such as the shape of the light curve. It seemed first that type I supernovae have very similar characteristics, whereas type II had more diversity. Type II supernovae were further classified into IIP and IIL by their light curve shapes (Barbon et al., 1979), and then a new subclass IIn ("n" stands for narrow lines) was added to account for the slowly evolving supernovae (Schlegel, 1990). Outliers of type I supernovae that were dimmer than the typical type I's were also found later on (Wheeler and Levreault, 1985; Chevalier, 1986), so the usual type I's were renamed to type Ia and the peculiar ones were named type Ib (Elias et al., 1985). Soon after, the peculiar type Ib supernovae were classified as type Ic (Wheeler and Harkness, 1986; Wheeler et al., 1987). There is another tricky class in which at first they seem to be type II, but as time goes on they lose their hydrogen features and transition to type Ib-like supernovae. By definition these are type II, but because they should be physically similar to type Ib they were named type IIb (Ensman and Woosley, 1987; Filippenko, 1988). I have summarized the current classification strategy of supernovae in Fig.1.5. Now there exists some minor subclasses of some types, due to the upsurge in number of observations. Type Iax is an underluminous subclass of type Ia, but it comprises 5–30% of all type Ia's and is becoming a firm class (Foley et al., 2013). Type Ibn is simply an analogy to type IIn, which exhibits narrow line features (Pastorello et al., 2007, 2008), but are much rarer. There are many more sub-categories of peculiar supernovae, such as broad-lined type Ic (Ic-bl) or double-peaked type Ib etc. There is also a relatively new class of "super-luminous supernovae", which is 1–2 orders of magnitude more luminous than normal supernovae (Gal-Yam, 2012).

The physical origin of the explosions are not clear, but it seems that type Ia and the rest have clearly different mechanisms. Type Ia supernovae have an especially long-standing debate of their explosion mechanism. Many of the observational clues (universality, no remnant, lack of hydrogen etc) point out that the direct origin is the thermonuclear runaway explosions of CO white dwarfs (WDs) exceeding Chandrasekhar mass. The debate is on how we can increase typical WD masses ($\sim 0.6\mathrm{M}_\odot$) up to the Chandrasekhar mass ($1.44\mathrm{M}_\odot$). One possible scenario is to transfer mass from a non-degenerate star companion via RLOF. When the mass transfer rate is in the range that it is high enough to accrete efficiently on the WD but low enough so as not to cause recurrent novae (which is in quite a narrow range), the WD can stably increase its mass and eventually reach the Chandrasekhar mass. This scenario is called the "single-degenerate (SD)" scenario, since it involves only one degenerate star. The other popular scenario is the "double-degenerate (DD)" scenario in which two WDs collide. If the combined mass of the WDs exceed the Chandrasekhar mass, they have a chance to explode. Both scenarios have deficits, and the problem has not been settled. Either way, the progenitor should be a binary system.

All the other types of suernovae are considered to be consequences of the core-collapse of massive stars ($\gtrsim 8\mathrm{M}_\odot$). Once the core of a massive star starts collapsing, the central density will reach nuclear density at some point. The infalling matter will be "bounced" away, creating an outgoing shock. If the shock can penetrate the envelope, it will be observed as a supernova explosion. There will be a remnant left at the centre, which will eventually cool down to become a neutron star or maybe a black hole. The diversity in the observed features probably comes from the differences in the progenitor star. Unlike the WDs in type Ia supernovae, massive non-degenerate stars

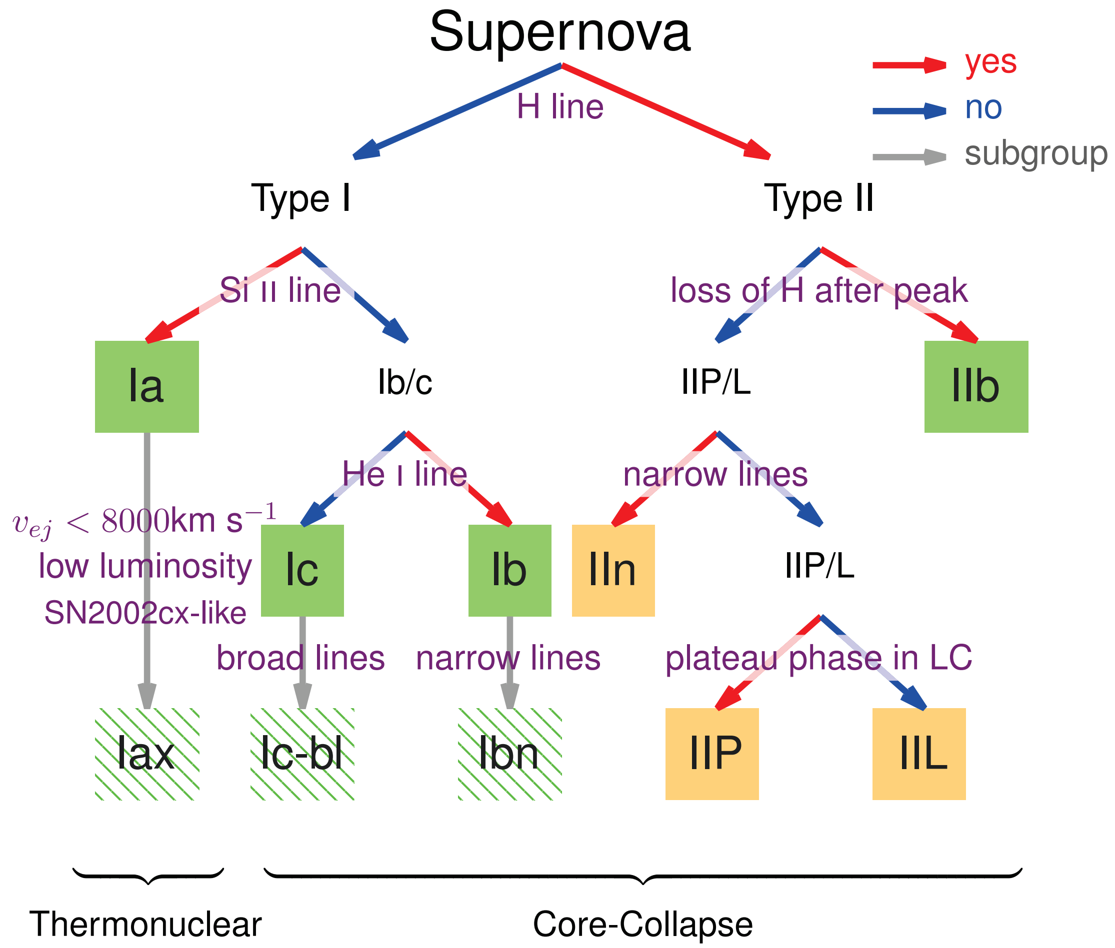

Figure 1.5: Classifications of supernovae. Supernova types in the green boxes are also called "stripped-envelope supernova", whereas the hydrogen envelope remains in the orange ones.

can have any kind of structure depending on its mass, metallicity, binarity etc. For example, the progenitors of type IIP/L/n supernovae (orange boxes in Fig.1.5) must have a large hydrogen envelopes remaining, but type Ib/c, IIb supernovae must have got rid of the entire or part of its envelope by the time of explosion. High metallicity stars can shed their envelopes by strong stellar winds, and may be progenitors of some of these "stripped-envelope supernovae". However, there are some cases that cannot be explained just by stellar winds, and binary interactions may be necessary. After all, we know that the majority of massive stars are in multiple systems and $\sim 70\%$ of them will interact during their lifetimes, so it is natural to consider that the majority of core-collapse supernova progenitors have experienced binary interactions too.

1.3.2 Supernovae in Binaries

As we have seen here, supernova is strongly related to binarity, either type Ia or core-collapse. In this thesis, I especially focus on the core-collapse supernovae in binaries. Unlike type Ia supernovae, where the exploding WD will disappear after the explosion, core-collapse supernovae leave compact remnants, meaning that if the remnant is bound to the companion, the system will carry on being a binary. These binaries can be the progenitors of X-ray binaries or luminous red novae, and if they can survive a second supernova in the system, they will become compact binaries such as binary neutron stars, binary black holes, black hole-neutron star binaries. Close binaries which are likely to interact or merge within Hubble time are of particular importance. Such systems have become one of the main focuses in astrophysics in the last few years, especially since the detection of gravitational waves from binary black holes (Abbott et al., 2016a,b,c). Although we have only detected binary black holes so far, binary neutron stars are also expected to be found in future operations, and can provide us more information if there are any electromagnetic counterparts.

Despite its importance, the formation scenario of compact binaries are not well established. Currently, there are three main pathways propsed in creating close compact binaries; massive binaries experiencing supernovae and common envelope evolution (Belczynski et al., 2002; Kalogera et al., 2007; Kinugawa et al., 2014; Belczynski et al., 2010), chemical homogeneous evolution of close massive binaries (Marchant et al., 2016; Mandel and de Mink, 2016), and dynamical formation in dense clusters (Portegies Zwart and McMillan, 2000; O'Leary et al., 2016). Among these scenarios, chemical homogeneous evolution is mainly aimed for binary black hole formation. Dynamical formation requires extreme environments and may not account for the seemingly high detection rate of gravitational waves. Thus the first scenario is called the "standard" scenario for compact binary formation. However, there are still many uncertainties in this scenario, mainly in the common envelope phase which is necessary to shrink the orbit.

The outcomes of the two supernova episodes are also uncertain. Roughly speaking, a binary system will break up if over half of the total mass is lost by the explosion. Wide binaries will certainly be destroyed because usually the more massive star in the binary will explode, and the mass expelled will be greater than half of the total mass. Closer binaries will experience mass transfer, and the more massive star will be smaller in mass than the secondary at the time of explosion, making it easier to survive. However, the natal kick given to the neutron star due to the asymmetry in the ejecta can help destroy the binary even if the expelled mass is small. Supernova ejecta may also strip mass off the companion or induce momentum, both of which makes the situation worse. The even bigger problem lies in the second supernova, since the mass of the secondary will be much larger than the compact remnant unless it loses its envelope via common envelope episodes. The ejecta mass will easily exceed half the total mass in these cases.

The effects of the supernova impact on the companion has been first studied analytically by (Wheeler et al., 1975). They simplified the process by assuming that the supernova ejecta is a plane slab as in Fig.1.6. The companion is divided into concentric cylindrical shells from the axis connecting the two stars of the binary, described by cylindrical coordinates normalized by the stellar radius,

$$x = b/R, \xi = z/R \tag{1.26}$$

where b is the radius of the concentric shells and z the axial coordinate. The mass

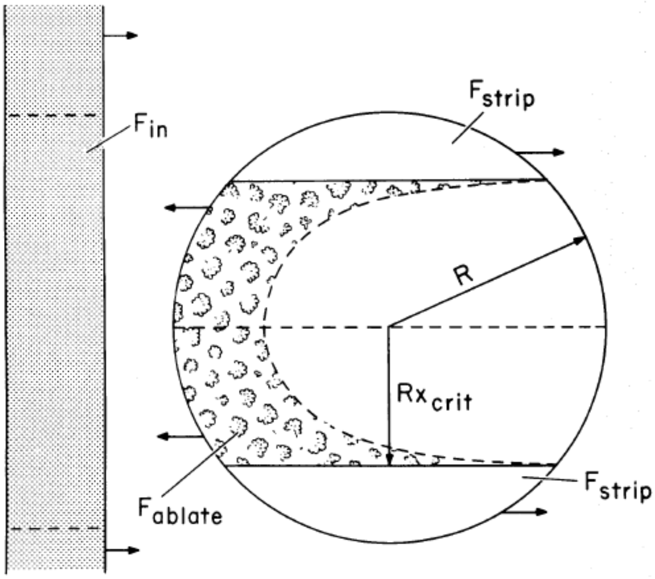

Figure 1.6: Schematic picture of the supernova ejecta colliding with a companion star as a plane slab (Wheeler et al., 1975).

contained in the shell at x per unit area can be calculated as

$$M'_c(x) = 2\rho_c R \Phi_1(x) \tag{1.27}$$

$$\Phi_1(x) = \frac{1}{\rho_c}\int_0^{\sqrt{1-x^2}} \rho\sqrt{x^2+\xi^2}d\xi \tag{1.28}$$

where ρ_c is the central density. The mass interior to x can be calculated as

$$M_c(x) = 4\pi R^3 \rho_c \Phi_2(x) \tag{1.29}$$

$$\Phi_2(x) = \int_0^x x'\Phi_1(x')dx' \tag{1.30}$$

As the slab hits the star, each cylindrical shell will accelerate the stellar matter using its original momentum. If there is no interaction between the shells, each shell will achieve a velocity

$$v(x) = \frac{M_{\mathrm{SN}} v_{\mathrm{SN}}}{M'_{\mathrm{SN}} + M'_c(x)} \tag{1.31}$$

where $M_{\mathrm{SN}}, v_{\mathrm{SN}}$ are the mass and velocity of the ejecta, $M'_c(x) = M_{\mathrm{SN}}/4\pi a_0^2$ is the mass per unit area of the ejecta and a_0 is the orbital separation. Shells will be knocked out if this achieved velocity exceeds the local escape velocity $v_{\mathrm{es}}(x)$. This condition can be expressed as

$$\frac{\Phi_1(x)}{2\Phi_2(1)} \leq \frac{1}{4}\frac{M_{\mathrm{SN}}}{M_c}\frac{R^2}{a_0^2}\left(\frac{v_{\mathrm{SN}}}{v_{\mathrm{es}}} - 1\right) \equiv \Psi \tag{1.32}$$

where M_c is the total mass of the companion, and Ψ is a parameter that expresses how capable the ejecta is to strip off the envelope. There should be a critical radius

$x_{\rm crit}$ in which all the matter outside this radius will be taken away. $x_{\rm crit}$ will satisfy the equality in Eq.1.32, and will be a monotonic function of Ψ. The amount of stripped mass will be expressed as $F_{\rm strip} = 1 - M_c(x_{\rm crit})/M_c$.

It will be unlikely that no matter in the layers inside $x_{\rm crit}$ will remain bound to the star. Due to the shock driven into the companion upon collision, some of the surface matter will obtain energies that can escape the gravitational potential. If we assume that the shock penetrates the envelope up to ξ, a fraction $F_{\rm es}(x, \xi)$ of the matter in the cylindrical shell will be heated. Momentum conservation gives

$$v(x, \xi) = \frac{M'_{\rm SN} v_{\rm SN}}{M'_{\rm SN} + M'_c(x) F(x, \xi)} \tag{1.33}$$

for the velocity of the heated matter. The condition for the matter to escape the gravitational well is that the thermal energy exceeds the binding energy $v^2(x, \xi) > v_{\rm es}^2$. If we take the maximum penetration length in which this inequality holds as $\xi_{\rm max}$, the fraction of mass that can escape $F_{\rm es}(x) \equiv F(x, \xi_{\rm max})$ can be expressed as

$$F_{\rm es}(x) = \frac{M'_{\rm SN}}{M_c(x)'} \left(\frac{v_{\rm SN}}{v_{\rm es}} - 1 \right) \tag{1.34}$$

We shall call the mass unbound in this way as "ablated", then the fractional amount of ablated matter will become

$$\begin{aligned} F_{\rm ablate} &\equiv \frac{R^2}{M_c} \int_0^{x_{\rm crit}} 2\pi x M'_c(x) F_{\rm es}(x) dx & (1.35) \\ &= R^2 \frac{M'_{\rm SN}}{M_c} \int_0^{x_{\rm crit}} \left(\frac{v_{\rm SN}}{v_{\rm es}} - 1 \right) 2\pi x dx & (1.36) \end{aligned}$$

The total unbound matter will be $F_{\rm eject} = F_{\rm stip} + F_{\rm ablate}$, and is a function of Ψ and the stellar structure. In other words, you can use this formula to calculate the amount of unbound matter given a stellar model, mass and energy of the explosion and an orbital separation. However, this simplified model ignores some important aspects that may become important in some situations. For example, for close binaries the geometry of the ejecta will not be a slab. Interactions between the shells have not been taken into account. A bow shock will surely form in front of the companion, and will deflect some of the ejecta away. These kinds of effects cannot be treated in this simplified model, and to properly evaluate their importance, multidimensional hydrodynamical simulations should be carried out.

1.4 Motivation of this Thesis

Compact binaries are one of the central interests in astrophysics now, and it is important to understand their formation. For compact binaries containing neutron star components in particular, we need to know how the binary can avoid disrupting because of the sudden mass loss by supernova explosions. In this thesis I will investigate the direct and indirect impacts of supernovae in massive binaries using numerical simulations. I mainly focus on the effects of the supernova ejecta hitting the binary companion, which I call "ejecta-companion interaction". I will also discuss some binary evolution scenarios to explain the formation of the progenitor of a particular supernova iPTF13bvn.

This thesis is structured as follows; in Chapter 2 I will discuss the upper limit of ejecta-companion interaction using two-dimensional hydrodynamical simulations. Then I will introduce a study on observational features of ejecta-companion interaction in iPTF13bvn in Chapter 3. Our predictions were unfortunately refuted by the latest observations, so I will discuss the possible alternative evolutionary paths of the progenitor of iPTF13bvn using stellar evolution simulations in Chapter 4. A more general study of ejecta-companion interaction is certainly required, and in Chapter 5 I will explain the numerical tools that we have prepared for future simulations. An overview of the numerical methods and codes are given in the appendix.

"Life is pleasant. Death is peaceful. It's the transition that's troublesome."
Isaac Asimov (1920–1992)

2

Upper Limit to Ejecta-Companion Interaction

2.1 Introduction

It is known observationally that about half of the observed stars are members of binary or higher order multiple systems (Raghavan et al., 2010; Duchêne and Kraus, 2013). The fraction increases with the primary star mass and reaches up to 69 % for O stars (Sana et al., 2012). These massive stars are supposed to end up exploding as core-collapse supernovae (CCSNe). It is hence natural to expect that the majority of CCSNe should take place in binaries.

Binary interactions may be crucially important for the evolution leading to core-collapse (Podsiadlowski et al., 2004). In particular, mass transfer will be essential to the spectral type of the supernova (SN) explosion. In fact, it is argued that type Ib and Ic SNe mainly occur in interacting binaries (Smith et al., 2011). It has also recently been reported that the late time photometry of iPTF13bvn, a type Ib SN, cannot be reproduced by single star progenitors, but can naturally be explained by binary progenitor models (Fremling et al., 2014; Bersten et al., 2014; Eldridge et al., 2015; Eldridge and Maund, 2016). This may be proof that type Ib SNe are actually occuring in binaries. The aftermath of the explosion could be no less important for the evolution of the binary system itself as well as of the companion star. It is well known that the binary system is disrupted if more than half of the total mass is expelled. This criterion is easily fulfilled when the primary star explodes unless it has lost most of its mass before explosion. Even if the amount of mass expelled is less than half the total mass, the system may still be disrupted due to neutron star kicks. The companion star will then carry on its life as a single star. If the binary survives the SN explosion, it will have a highly eccentric orbit (Pijloo et al., 2012). Some observational facts of a high mass companion actually surviving the SN explosion are known (Seward et al., 2012; Geldzahler et al., 1980). Most high mass X-ray binaries (HMXBs) and low mass X-ray binaries (LMXBs) must have undergone SN at some time in their formation, which means a certain fraction of binaries need to survive from explosion.

Collisions of the supernova ejecta (SNE) with the companion star may also affect the evolution of the latter if the binary separation is small enough. Wheeler et al. (1975) were the first to estimate the mass removed from the companion star by the impact. They considered momentum conservation in a simple analytical model to express the amount of mass removed with a single parameter and estimated that up to 15% of the companion mass will be ejected.

Numerical computations were also carried out by Fryxell and Arnett (1981), confirming the results by Wheeler et al. (1975). Their two-dimensional computational grid of 32×32 was rather coarse by the current standard. They also assumed a planar shell as a model of SNE, which may not be a good approximation for small binary separations, where the spherical geometry of SNE is not negligible. Livne et al. (1992) followed, assuming a red giant companion of 1 $\mathrm{M}_{\odot}$. They treated the SNE as a spherical shell and used a finer mesh, enough to describe the envelope with fine zoning (typically 107×65). They found that almost the entire envelope of the red giants were stripped off by SNE. The result may be applied not only to type Ib SNe but also to type Ia SNe.

The impact of SNE on companion stars have been better studied for Type Ia SNe (Marietta et al., 2000; Pan et al., 2013; Liu et al., 2013b; Kasen, 2010) in the single degenerate (SD) scenario, where a carbon-oxygen white dwarf accretes mass from its low-mass binary companion (Nomoto, 1982). Carrying out numerical calculations with high resolutions, these authors placed strong constraints on the structure of companion stars in the SD scenario.

In this chapter, we perform similar simulations, but assuming more massive stars for both the primary and secondary stars, which will be appropriate for CCSNe. Unlike for type Ia SNe in the low-mass binary, there is no standard model for CCSNe. In fact, the masses and structures of the primary and secondary stars as well as the binary separation are almost free parameters, since there are not many observational constraints. We pay particular attention to the upper limit on the mass removed from a massive companion and its dependence on orbital separation. For the analyses of the results, we perform additional simulations of experimental nature, modifying the density and/or velocity of SNE artificially. It turns out that these are indeed helpful to pin down which physical quantity is most essential in determining the amount of removed mass.

This chapter is structured as follows: In section 2.2, we describe the models and numerical method we used. The main results are shown in section 2.3, and discussions are given in section 2.4. Finally, we summarize our results in section 2.5.

2.2 Models & Numerical Method

In this chapter we numerically investigate the impacts of the SNE against the companion star in a massive close binary. We employ two-step strategy: the explosion of the primary star is computed in spherical symmetry, ignoring the existence of the secondary star, to obtain the structure of the SNE (Step 1); the collision of the SNE obtained in step 1 against the companion star is simulated under the assumption of axisymmetry (Step 2). Details of each step are given below.

2.2.1 Numerical Method

We use a two dimensional hydrodynamic code "yamazakura" for all computations performed in this work (Sawai et al., 2013). It is a time-explicit Eulerian code based on a high resolution central scheme (Kurganov and Tadmor, 2000). Spherical coordinates are employed and axisymmetry but no equatorial symmetry is assumed. In Step 1 we further impose spherical symmetry, putting the origin of the coordinates at the centre of the primary star and ignoring its rotation as well as the orbital motion and the gravity of the companion star. In Step 2 the existence of the primary star is ignored, with the origin of the coordinates coinciding with the centre of the companion star. The symmetry axis is directed to the primary star and rotation of the companion star as well as the orbital motion is neglected. The self-gravity of the companion star and SNE in the computational domain is included by solving the Poisson equation with the boundary conditions set by multipole expansion. An ideal equation of state with an adiabatic index $\gamma = \frac{5}{3}$ is applied throughout.

2.2.2 Binary Parameters

The masses of the primary and companion stars are set to $M_1 = 10\mathrm{M}_\odot$ and $M_2 = 10.7\mathrm{M}_\odot$, respectively. Note these are not the masses at birth of the binary system but the values just prior to the SN explosion of the primary star. These values are chosen so that the primary star would be massive enough to produce a SN explosion and the mass ratio should be close to unity, in which case the companion star radius R_2 could be largest for a given separation a.

The a/R_2 ratio is expected to be one of the most essential parameters that determine the amount of mass removed by the ejecta (Wheeler et al., 1975). In order to maximize the impact of SNE on the companion star we choose the separation of binary as small as possible under the restriction that the companion should not cause Roche lobe overflow (RLOF). Assuming that the secondary star fills the Roche lobe, we obtain the minimum separation a_{min} from the Eggleton relation (Eggleton, 1983):

$$a_{\mathrm{min}} = \frac{0.6q^{\frac{2}{3}} + \ln(1 + q^{\frac{1}{3}})}{0.49q^{\frac{2}{3}}} R_2, \tag{2.1}$$

where $q = M_2/M_1$ is the mass ratio. The period of the Keplerian motion with this separation is approximately 5 years, which is significantly long compared to the characteristic timescale of the collision of SNE with the companion star, $\sim R_2/v_{\mathrm{ej}} \sim$ a few weeks. Here v_{ej} is a typical velocity of SNE. It is hence justified to neglect the orbital motion in Step 2.

It is one of the main objectives in this work to find the dependence of the removed mass on the binary separation. For this purpose we have carried out several simulations with different separations $a = (1.0, 1.1, 1.2, ..., 2.5) \times a_{\mathrm{min}}$.

2.2.3 Step 1: Primary Star Explosion

Since we are not interested in the still unknown SN mechanism, we artificially produce a SN explosion in this study by injecting internal energy into the central region of the primary star. Such a procedure is often called the "thermal bomb" (Young and Fryer, 2007). For the progenitor, we use a pre-SN model of Heger & Wellstein 1999 (unpublished), which was computed according to the binary evolution models of Wellstein and Langer (1999), in which the "standard" Wolf-Rayet mass loss rate is reduced by a factor of 6 and mass transfer is taken into account. The mass and radius of the primary star are $M_1 = 10\mathrm{M}_\odot$ and $R_1 = 7.9 \times 10^5$km, respectively, just prior to the SN explosion. It has totally lost its H layer, and is a helium star since it has undergone a significant amount of mass loss.

We cover the primary star with a one-dimensional spherical grid. 1600 grid points are non-uniformly distributed in the radial direction. The inner boundary is chosen so that the central $1.4\mathrm{M}_\odot$, corresponding to a neutron star, should be excluded from the computational region. The outer boundary is set at approximately 40 times the stellar radius. 10^{51} erg of internal energy is added to the inner 10 grids. Self-gravity is included in this computation, although its effects are limited. We impose the reflective condition at the inner boundary whereas the outgoing boundary condition was used at the outer boundary.

After the shock wave breaks out of the stellar surface, the SNE continues to expand, converting internal energy to kinetic energy. Since the hydrodynamic code cannot handle vacuum, we artificially fill the volume outside the star with matter, which is so dilute that it should not affect the dynamics. When the SNE reaches the outer boundary of the computational domain, it expands almost self-similarly. We record the density, pressure, velocity at an arbitrarily chosen point near the outer boundary as a function of time so that we could use them in Step 2 as described shortly.

2.2.4 Step 2: Collisions of SNE on the Companion Star

As mentioned above, we place the companion star at the centre of a two-dimensional spherical mesh, whose axis is aligned with the line joining the centres of the two binary components. Neglecting rotation of the companion star and the orbital motion, we assume axisymmetry in this step. The computational domain extends from the radius of $r = 4 \times 10^6$km to $r = 8 \times 10^8$km, which is roughly twice the radius of the companion star. The central portion that contains $2.79\mathrm{M}_\odot$ is cut out to avoid too severe CFL conditions. We treat it as a point gravitational source and we impose a reflective inner boundary condition. The computational region is divided into 600 $(r) \times 180$ (θ) zones non-uniformly in the radial direction and uniformly in the θ direction. It is important to put the radial grid points appropriately in order to keep the star in hydrostatic equilibrium. We deploy at least 20 mesh points in each density scale height inside the star. On the other hand, we distribute the radial grid points uniformly outside the star, where we again put a dilute gas for numerical convenience. The locations of the grid points determined this way are shown in Figure 2.1.

For the companion star we adopt the non-rotating s11.0 model from Woosley et al. (2002), since no information is available on the companion in Heger & Wellstein 1999 (unpublished). This companion star model gives a mass ratio close to unity and gives the smallest value to $a_{\min}/R_2$ among available stellar models. In fact, its radius of the companion star is $R_2 = 4.08 \times 10^8$km and the a/R_2 ratio used in this study ranges from 2.7 to 6.7. Since it is a pre-SN model, i.e. the star is near the end of its evolution and has a loosely bound envelope, so the results of our simulation possibly serve as an upper limit for the amount of mass stripped in CCSNe of primary stars.

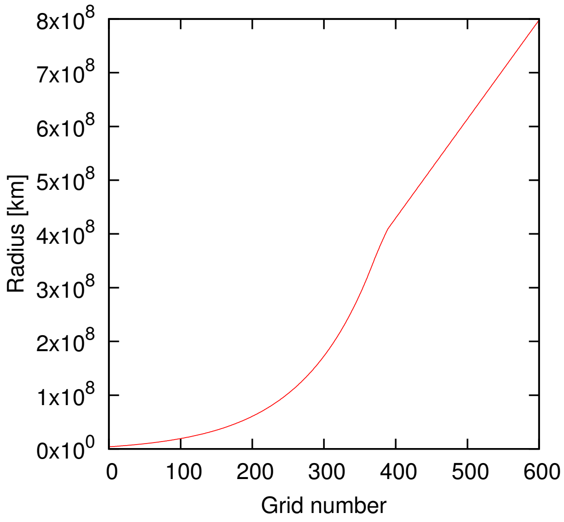

Figure 2.1: The locations of the radial grid points used in Step 2.

It is true that the companion model is actually a single star model and not consistent with the primary star model, and may not be a realistic binary system. But massive binaries that will produce a CCSN are very much diverse and our understanding of their evolutions is not yet complete. Moreover, binary-progenitor models available to us for the moment are not many, either. In this study, we therefore focus on the systematics of interactions between SN ejecta and the companion star, paying particular attention to the binary separation. Our simulations are experimental in this sense. Exploration of the dependences on the mass, structure and composition of the companion star for more realistic models will be left for future works.

As mentioned above, the companion star is adopted from pre-SN models and its central core has already started to collapse. The computational domain excludes the central collapsing core, however. It is confirmed that the remaining envelope is almost in hydrostatic equilibrium and does not change significantly for at least 200 days after mapped onto the two-dimensional computational grid, which is shown in Figure 2.2.

SNE is injected from one hemisphere of the outer boundary with its spherical geometry being taken into account properly. We estimate the density, pressure and velocity of SNE from the data obtained in Step 1, assuming that the SNE continues to expand self-similarly from the outer boundary of Step 1 to that of Step 2. The free boundary condition is applied to the other hemisphere of the outer boundary. Simulations start from the time, when the outermost part of the SNE touches the surface of the companion star.

To follow Lagrangian motions of fluid elements in our Eulerian hydrodynamics code and find which portions of the companion star are stripped by SNE, we deploy tracer particles in the companion star as well as in the SNE. The tracer particles are moved with the fluid velocities at their instantaneous locations, which are obtained by the hydrodynamical computations, and do not affect the dynamics of SNE and stellar matter. Each particle is labelled whether it originates from the star or ejecta and whether it escapes out of the computation domain before the termination of simulations or not. These information are extremely useful to understand how the mass-stripping takes place in the collision of SNE and the companion star.

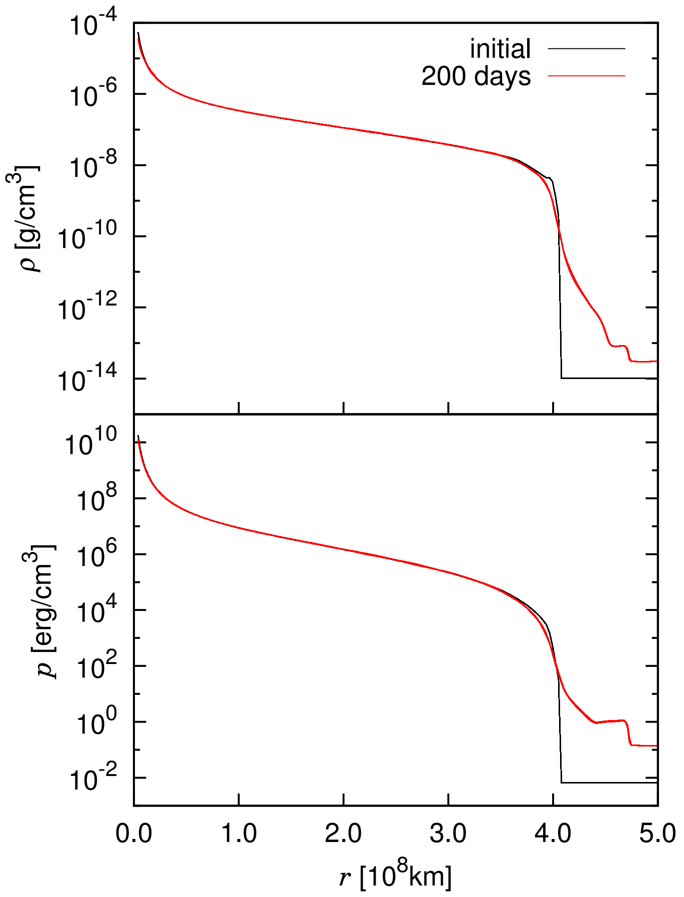

Figure 2.2: Density (*upper*) and pressure (*lower*) profiles of the companion star model. The initial profile (black line) is compared with the profiles of the star after being relaxed on the two-dimensional computational grid for 200 days (red line).

2.3 Results

In the following the numerical results for each step are given in turn.

2.3.1 Step 1: Primary Star Explosion

We artificially initiate the SN explosion in the primary star by depositing thermal energy near the inner boundary. The pressure excess then drives the shock wave outwards into the envelope. The deposited energy of 10^{51}erg, the canonical value for CCSNe, is large enough to expel the outer envelope, since its binding energy is much smaller. The shock wave continues to propagate outward unhindered and breaks out of the stellar surface after 30 s.

Figure 2.3 shows the propagation of the shock wave in the stellar envelope. It is clear that a dense shell is formed after the shock wave. It is also discernible that a reverse shock is produced when the forward shock passes through the boundary of C/O and He. It is known that the deceleration of matter by negative pressure gradients then induces a Rayleigh-taylor instability in the vicinity of the CO/He boundary. We ignore such multi-dimensional effects in the present study, anticipating that the dynamics of collision of the SNE and the companion star, particularly the removed mass, will not be affected severely by the small-scale perturbations.

After the shock break-out, the stellar envelope starts to expand into inter-stellar matter (ISM) as an SNE. It is initially accelerated by its own pressure, converting thermal energy to kinetic energy. When most of the thermal energy is consumed, the SNE expands ballistically until it sweeps up an amount of interstellar matter comparable to the SNE itself and the Sedov-Taylor phase commences. This is indeed observed in our simulation as shown in Figure 2.4. In the left panels the profiles of density, pressure and velocity are shown for different times after the shock break-out whereas in the right panels the rescaled distributions are compared. Self-similarity of the expansion is evident from the latter comparison. We assume in this study that this free expansion of SNE continues until it reaches the companion star.

The computation of Step 1 is terminated when most of the SNE leaves the computational domain. The temporal evolutions of density, pressure and velocity are recorded at distances $r = 8.11,\ 8.85,\ 9.65 \times 10^5$km from the centre of the exploding star. They are shown on the left panels of Figure 2.5. As the dense shell of SNE passes through these points, the density and pressure rise rapidly and decline gradually. The self-similarity in the expansion of SNE is also reflected in these profiles as demonstrated on the right panels, where we rescale the profiles by the distance r. We can see that the three lines almost exactly agree after this rescaling, which indicates that the SNE expands in a self-similar fashion. We utilize these rescaled profiles to set the initial and boundary conditions in Step 2.

2.3.2 Step 2: Collisions of SNE on the Companion Star

Dynamics of Collisions

We first describe the dynamics of the collisions of the SNE and the companion star for the base model, in which the binary separation is set to $a = a_{\rm min}$. The results for other models with different binary separations will be presented later on but qualitative

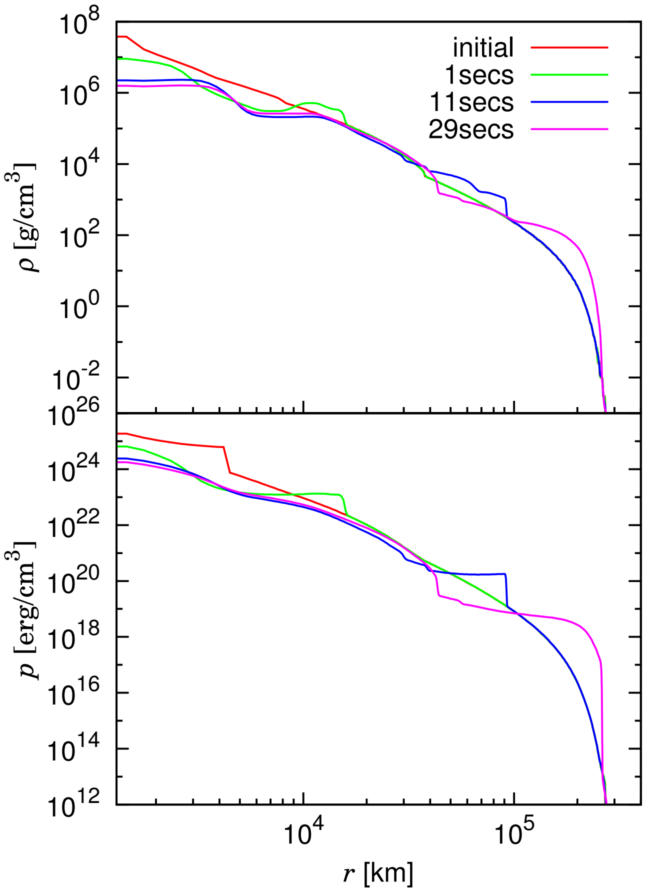

Figure 2.3: The shock propagation through the primary star. Density and pressure distributions are shown on the top and bottom panels, respectively. The CO/He boundary lies at $r = 3.8 \times 10^4$km, where there is a "hump" in the initial distribution.

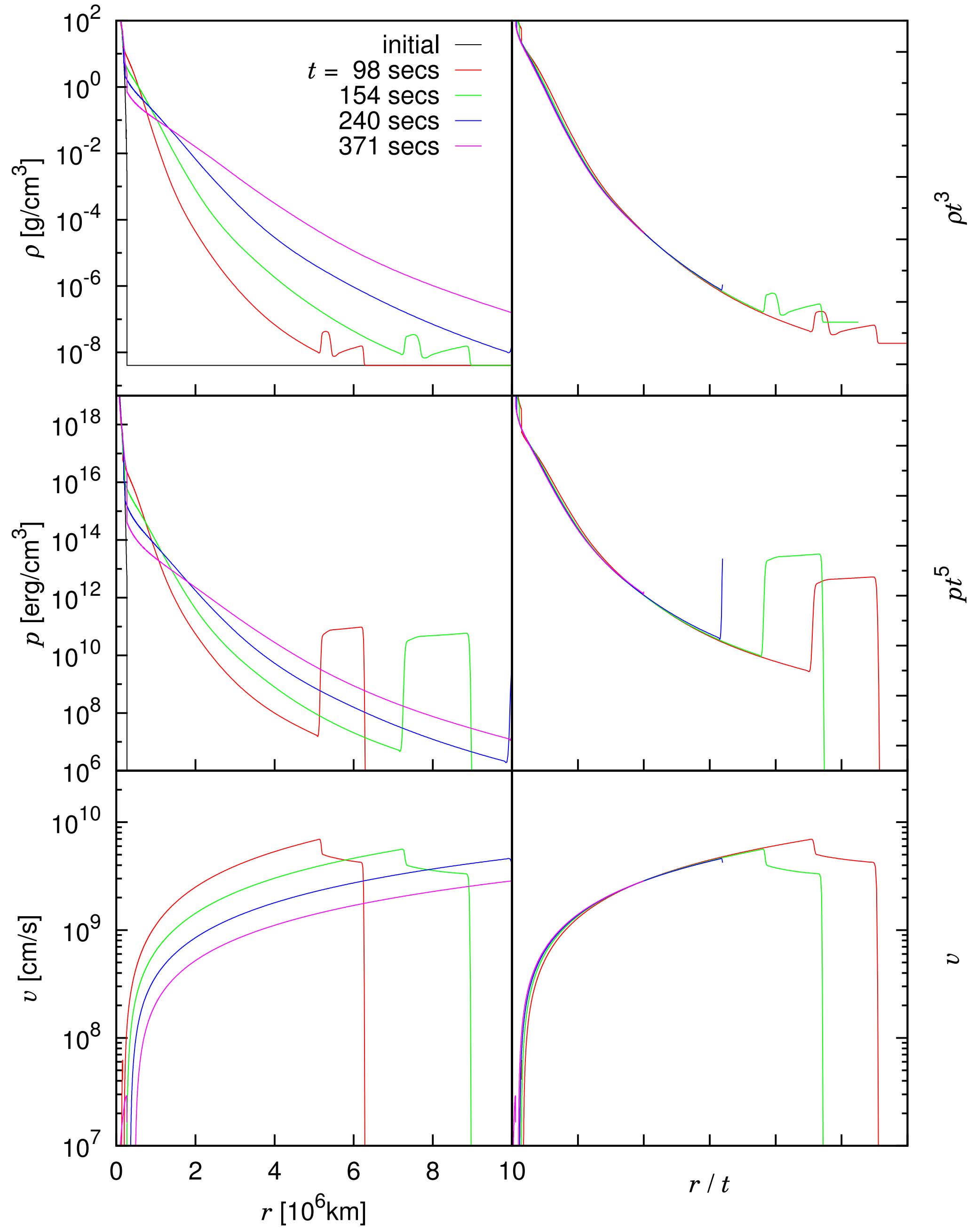

Figure 2.4: The spatial distributions of the SNE at various times. Left panels show the actual spatial distributions, whereas right panels display those rescaled by the time since SN explosion.

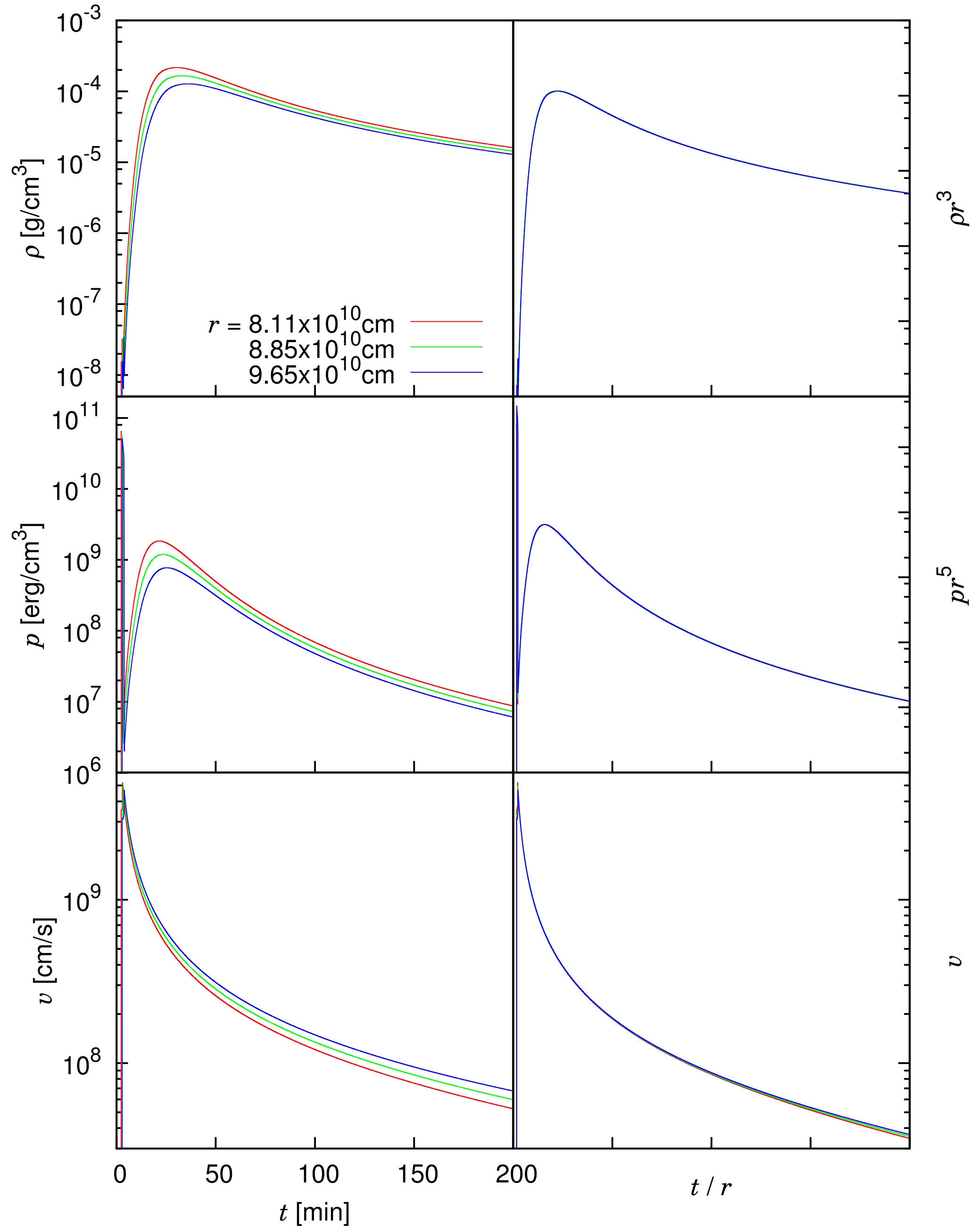

Figure 2.5: Profiles of density, pressure and velocity of the SNE. Left panels show the actual profiles at distances $r = 8.11, 8.85, 9.65 \times 10^{10}$cm from the exploding star. Right panels display the same quantities but scaled by the distance. We can see that the three lines agree almost exactly, which indicates a self-similar expansion.

features are common. The density and velocity profiles are shown at different times t elapsed since the SN exlosion of the primary star in Figures 2.6 and 2.7, respectively. The top left panels in these figures correspond to the initial state for Step 2. Note that the lengths of vectors are scaled for visibility and amplified by a factor of 50 for the right panels compared to the left panels because the velocity becomes quite small at these late stages.

We can see that as the SNE hits the companion star surface, a forward shock is formed and penetrates through the star. This shock wave heats the stellar matter as it propagates, and eventually reaches the other side of the star. The shock decelerates as it climbs the steep density gradient of the star toward the centre of the companion star. It then accelerates at the latter half, climbing down the density gradient from the centre to the stellar surface and depositing much smaller energies. Some of the heated matter starts to expand (Panels (d) and (e)). A reverse shock is also formed and becomes a bow shock in the SNE. It is almost stationary at the beginning as the ejecta flows past (Panels (b) and (c)). Once the ejecta density starts to decrease, however, it begins to expand leftwards into the SNE and eventually gets out of the computational domain (Panels (d) and (e)). After the forward shock penetrates the entire star, the whole star slowly expands almost spherically to reach a new equilibrium (Panel (f)).

The SNE does not strip the stellar matter directly as assumed in the previous papers (Wheeler et al., 1975). This is mainly due to the presence of the bow shock, which deflects the ejecta away. Most of the removed mass is instead ablated off with the internal energy deposited by the forward shock and is also pulled off by the rarefaction wave generated by the reverse shock. These results are consistent with the previous findings for low mass companion stars in type Ia SNe (Marietta et al., 2000; Pan et al., 2013; Liu et al., 2013b; Kasen, 2010). The shock break-out of the opposite side of the companion star also produces some mass ejections there.

The above statements are more clearly vindicated in Figure 2.8, where the positions of tracer particles are displayed at the same instants as in Figures 2.6 and 2.7. In the upper half of each panel the particles originating from the star (blue) are distinguished from those from the SNE (red) by colours. The lower half, on the other hand, shows whether it is "bound" to the companion (light blue) or not (grey). The definition of the boundedness will be given in the next subsection in detail. We can see that as the shock propagates through the star, the heated matter becomes unbound initially. Although the central region quickly becomes bound again thereafter, the outer part remains unbound and expands almost radially, an indication of thermal ablation. On the opposite side of the star, only the low-density matter near the stellar surface becomes unbound by the shock passage because the shock is weakened by that time due to the pull-back by the rarefaction wave. The central bound region then restores a spherical shape after a long time. The unbound region continues to expand, on the other hand, and eventually reaches the edge of the computational domain. Since we cannot determine for sure the fate of the particles that have left the computational region, we stop the simulation there. This constraint led to the termination time of 122 days for the closest separation model and that down to 105 days for the models with the farthest separations.

Figure 2.8 also points out that there is almost no ejecta contamination going on on the companion star surface. At the end of the simulation, all bound particles are of companion star origin. This indicates that we will not be able to observe imprints of the primary star on the surviving companion after SN.

Removed Mass

In previous studies on type Ia SNe (Marietta et al., 2000; Pan et al., 2013; Liu et al., 2013b), the stripped mass is estimated from the total energy defined locally as

$$\epsilon_{\rm tot} = \frac{1}{2}v^2 + \epsilon_{\rm int} + \phi, \tag{2.2}$$

where v is velocity, $\epsilon_{\rm int}$ the specific internal energy and ϕ the gravitational potential. If this energy is positive, which is equivalent to having a velocity exceeding the local escape velocity, the fluid element there is judged to be unbound. We shall call this the "escape criterion". The removed mass is the sum of these unbound masses. It should be noted, though, that the removed mass defined this way is time-dependent particularly at early times because the pressure inside the star is still large and interactions among fluid elements cannot be neglected. It takes rather long for the removed mass calculated by this criterion to settle to the final value as shown in Figure 2.9, in which the temporal evolution of the removed mass is shown.

We find that an alternate criterion is more useful to estimate the removed mass. It is based on Bernoulli's principle, which claims under certain conditions that particles along a streamline conserve the following quantitity

$$\epsilon_{\rm ber} = \frac{1}{2}v^2 + \epsilon_{\rm int} + \frac{p}{\rho} + \phi, \tag{2.3}$$

where p is the pressure density and ρ the mass density. Strictly speaking, the principle is valid only in steady systems. Regardless, we assume that a fluid element is unbound if $\epsilon_{\rm ber}$ is positive. Note that $\epsilon_{\rm ber}$ should eventually approach $\epsilon_{\rm tot}$ when the pressure becomes negligible. The removed mass is defined as the sum of masses of unbound fluid elements determined this way. We refer to this scheme as the "Bernoulli criterion" in the rest of this work.

In Figure 2.9 we compare the removed masses obtained by the two criteria as a function of time for the base model with $a = a_{\rm min}$: the escape criterion is shown as the blue line whereas the Bernoulli criterion is displayed with the red line. It is evident that both lines approach the same asymptotic value, indicating that the two criteria give identical results when computed for long enough. More importantly, the red line reaches the final value earlier than the blue line, that is, the Bernoulli criterion is more efficient to estimate the removed mass. This is indeed important, since the computing resource is limited and in some models we cannot afford to run simulations long enough to see the settlement of $\epsilon_{\rm tot}$.

The shock heating of the matter facing the primary star, the main heating phase, lasts approximately 20 days. It takes about 70 days for the removed mass by the Bernoulli criterion to settle to the asymptotic value, which is the time scale for the forward shock to reach the other side of the star. This is merely a few % of the orbital period and supports our neglection of the orbital motion in this study. At this time, the whole star starts expanding almost spherically and the expansion carries on for a few more months, where the effects of orbital motion and possible stellar rotation may become non-negligible.

Table 2.1: Spatial resolutions adopted in convergence tests.

model	r-grids[1]	θ-grids[1]	M_{ub}[2] [$\mathrm{M}_\odot$]
base	600	180	2.594
ctr550	550	180	2.620
ctr500	500	180	2.627
ctr450	450	180	2.639
ctt150	600	150	2.629
ctt120	600	120	2.665
ctt090	600	90	2.704

[1] r-grids and θ-grids show the number of grids used in each direction.
[2] M_{ub} is the removed mass.

The amount of mass removed reached up to 25% of the original companion mass in the base model. This is a significant fraction for the later evolutions of both the companion star and the binary system itself. It can be regarded as an alternate scenario of mass loss from high mass stars other than binary interaction or stellar winds. In the base model we assume the smallest possible binary separation and the removed mass will be largest. The next question is obviously how the removed mass depends on the binary separation.

Numerical Convergence

Before proceeding to other models with different binary separations, we check here whether the spatial resolution employed in the simulation is appropriate. For this purpose we ran models with the same physical setup but with different spatial resolutions. The number of grid points was changed separately for r and θ directions. They are summarized in table 2.1.

The dynamics of these test runs are compared with the base model in Figure 2.10. The flow patterns hardly show any difference for the models with different grids in the r direction. On the other hand, as the grid becomes coarser in the θ direction, the shock waves are slightly broadened, while complex flow patterns particularly behind the companion star are changed even qualitatively. The removed mass, which is our main concern in this study, is hardly affected, however. Its values are listed on the table for each model. Note that the number of tracer particles is unchanged in these experimental computations. Although there is a clear trend that the removed mass decreases as the number of grid points increases, the variation is small, $\sim 1\%$, and does not affect our conclusion. We hence belive that the resolution employed in this study is appropriate.

Separation Dependence

In the base model, the binary separation is assumed to be $a = a_{\mathrm{min}}$. This is the smallest possible value and is most likely to be too small. We have hence performed the same

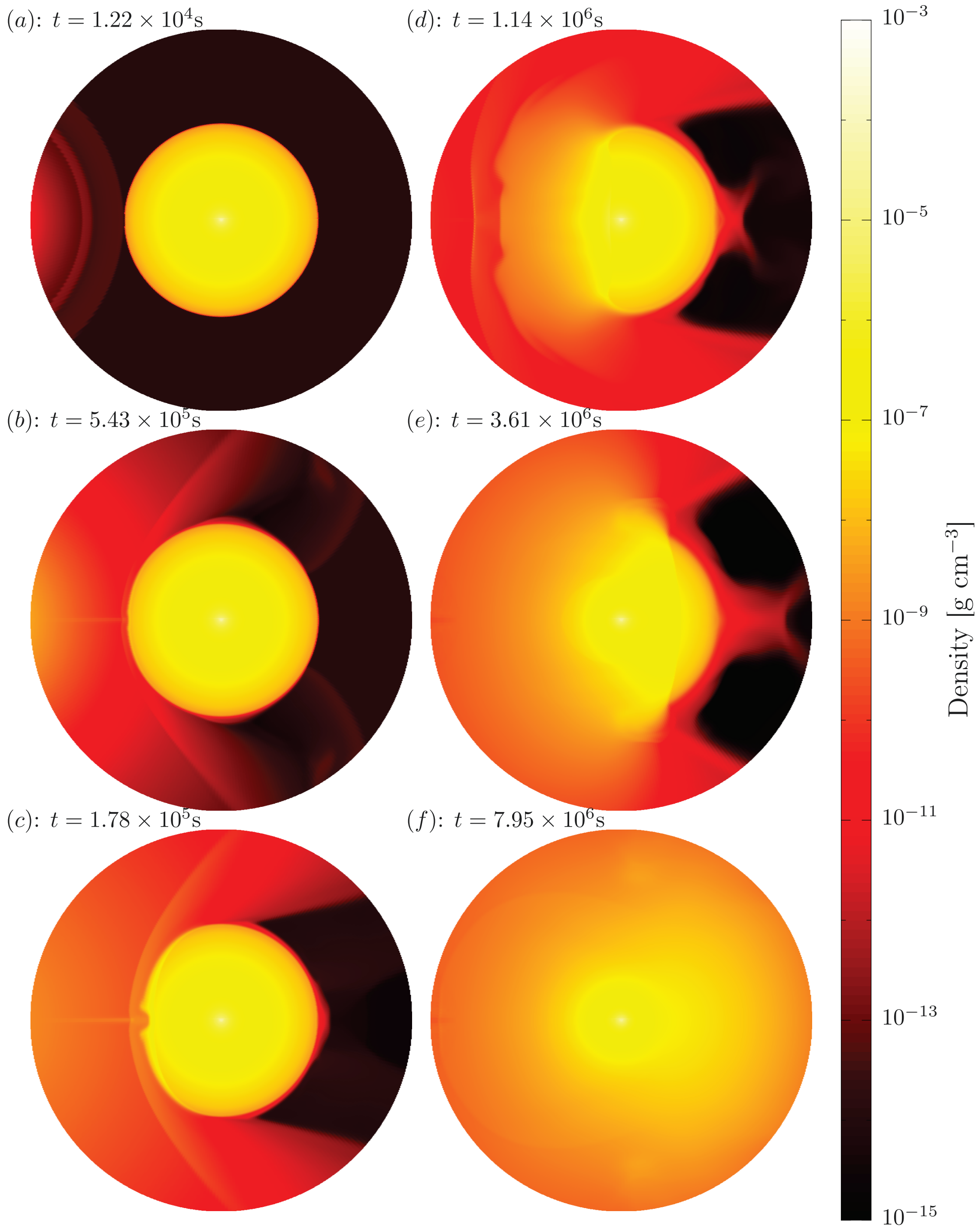

Figure 2.6: The density profiles at Step 2. The time elapsed since SN explosion is indicated for each panel. The radius of each circle is 8×10^{13}cm. The colour bar is in log scale.

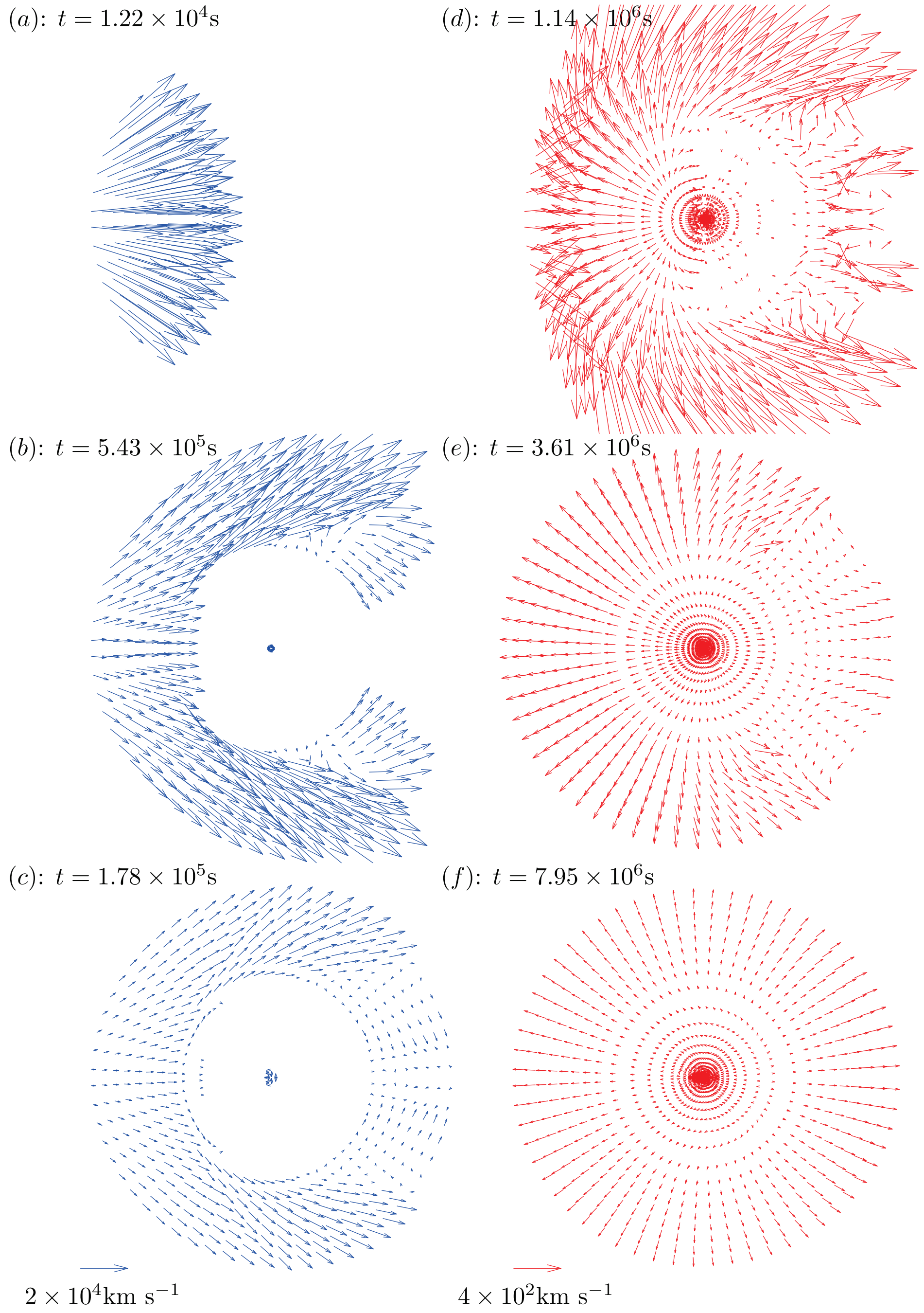

Figure 2.7: The velocity vectors at Step 2. Note that red arrows on the right panels have lengths amplified by a factor of 50 compared with blue arrows on the left panels.

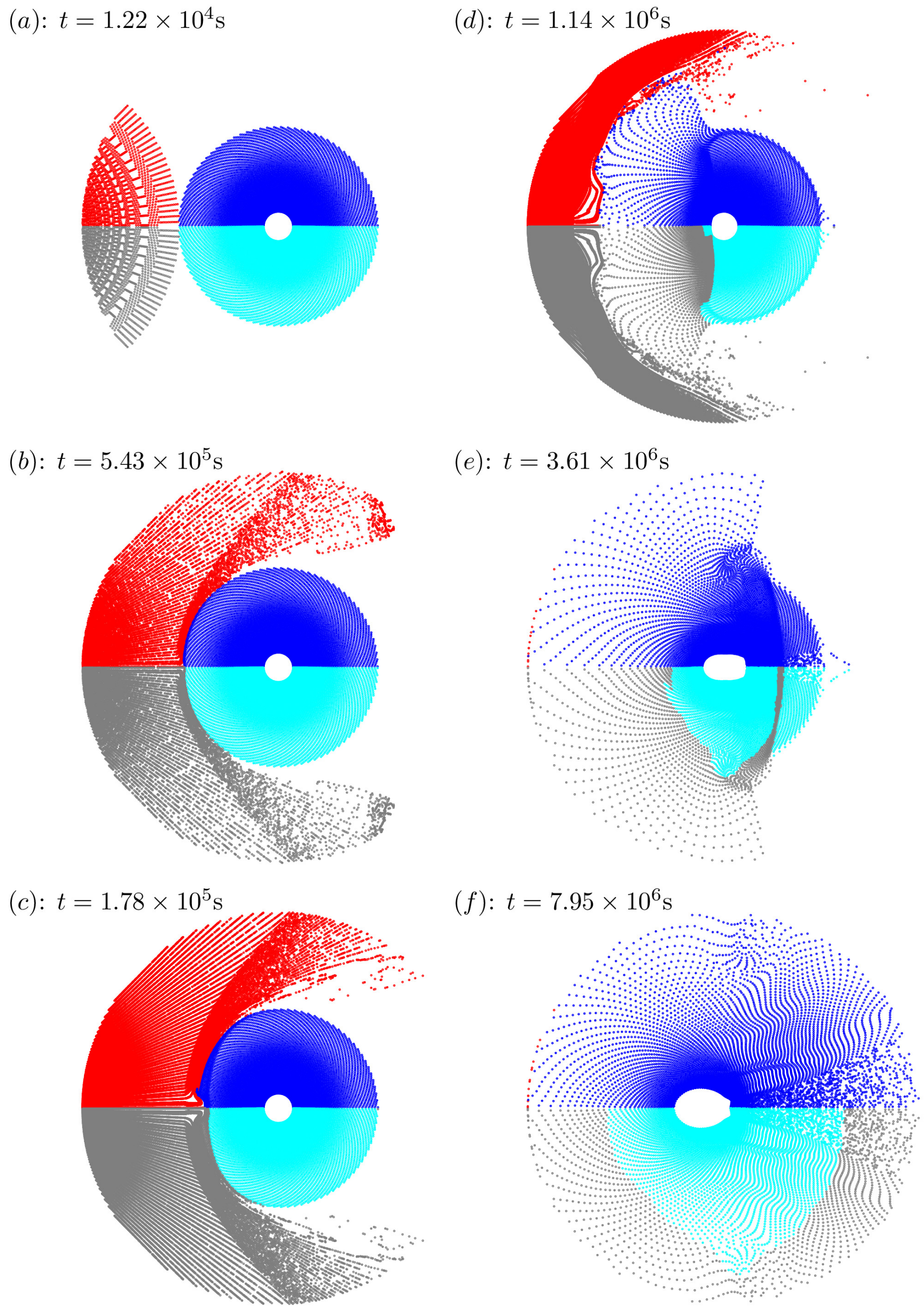

Figure 2.8: The tracer particles at various times. The upper half of each panel indicates in colour whether the particles originate from the SNE (red dots) or the companion star (light blue dots). The lower half shows in colour whether the particles are bound to the star (blue dots) or not (grey dots).

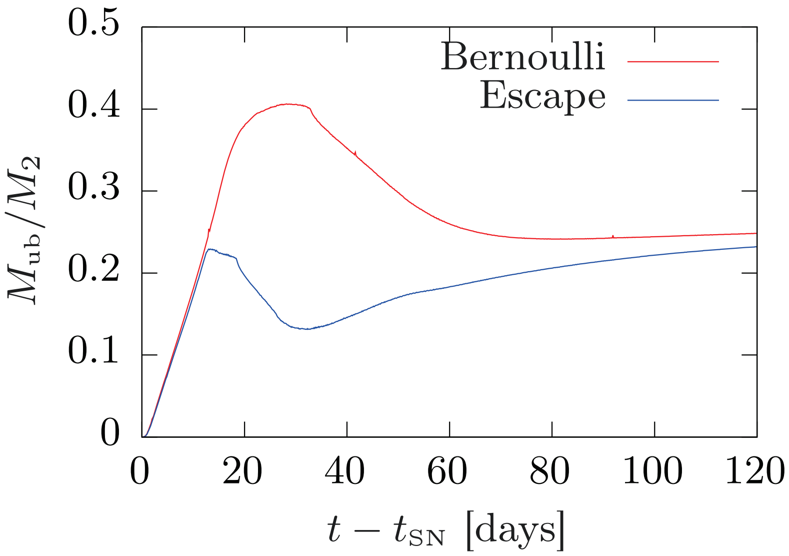

Figure 2.9: The removed mass as a function of time for the base model with $a = a_{\rm min}$. It is evaluated by two different criteria: the escape criterion (blue line) and the Bernoulli criterion (red line). See the text for details.

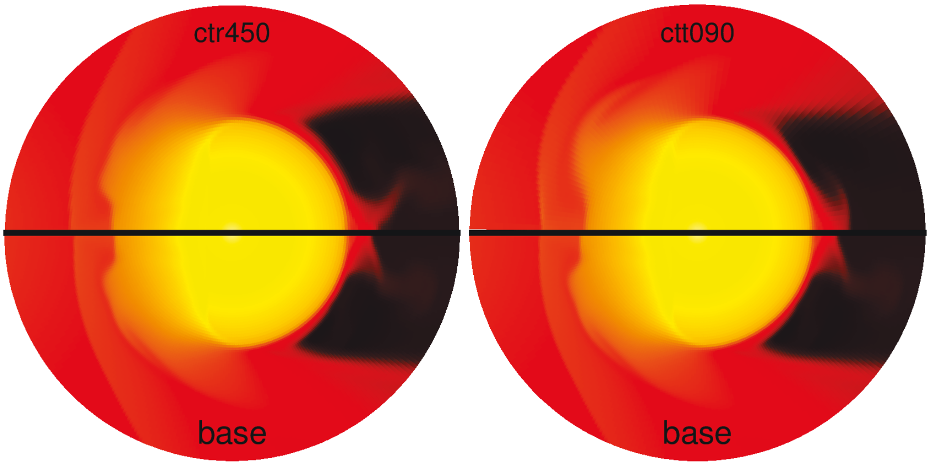

Figure 2.10: Density distributions for different resolutions. Snapshots at the time $t = 8.5 \times 10^5$ from models ctr450 (*left*) and ctt090 (*right*) are compared with that from the base model. The grids used for each model are given in table 2.1

simulation for several models varying the separation as $a = (1.1, 1.2, ..., 2.5) \times a_{\min}$ to see the dependence of removed mass on separation. As the binary becomes wider, the density of SNE at the impact against the companion star is decreased; the SNE is more extended specially and the collision lasts longer; since the solid angle of the companion star is also decreased, the total energy contained in the portion of SNE that collides with the companion star is reduced proportionately; the curvature of the dense shell in the SNE becomes less pronounced. All of these effects but the last one will tend to decrease the amount of the removed mass. The smaller curvature of the SNE may lead to smaller deflections by the bow shock and contribute to some direct stripping.

For other models with wider separations, forward and reverse shocks are formed when the SNE hits the surface of the companion (panel (a) of Figures 2.11 and 2.12) as was the case for the base model. The forward shock has smaller pressure and velocity, since the incident ejecta energy density is smaller. Since it takes the forward shock longer to sweep the entire star, the hemisphere of the companion star that faces the primary star and is shock-heated earlier has a highly extended envelope compared to the opposite hemisphere that is heated later, making the star take a very asymmetric shape (panel (b) of Figures 2.11 and 2.12). Since the shock heating is significantly weaker in the wide binaries, only the initially shocked regions become unbound and the total removed mass is smaller. As the forward shock reaches the opposite side of the companion star (panel (c) of Figures 2.11 and 2.12), much smaller amounts of matter become unbound near the surface.

The removed masses are calculated in the same way as in section 2.3.2 and are shown as a function of time in Figure 2.13 for some representative models. Other models have similar features. Although the removed masses tend to asymptotic values within a few months in all models, those with wider separations settle at earlier times. It will also take more time until the companion regains mechanical and thermal equilibrium in these models.

For the models with the widest separations, the heated but still bound matter reaches the outer boundary before the forward shock reaches the other side of the companion star. This may lead to errors in the estimation of the unbound mass, since the heating has not finished, and our Bernoulli criterion may not be applicable yet. To see the possible effects of the size of the computational domain, we performed test calculations with wider computational regions. We set the outer boundary to be 2×10^9 km in these simulations, which is 2.5 times the original size. The inner boundary and spatial resolution inside the companion star were chosen to be the same, while we increased mesh size in a geometric way outside. With this wider domain, we can continue the simulations longer.

Figure 2.14 shows a snapshot of the simulation with the new region, which is compared with the result for the original region. Although the position of the reverse shock is slightly different, there are no qualitative differences in the overall behaviour. The expansion of the bound region continued throughout our simulation, and even exceeded our wider boundary. This is approximately five times the original stellar radius and will keep on expanding for a while. The time evolution of the unbound mass is shown in Figure 2.15. Despite the fact that the expansion has not ceased, the unbound mass settles to a constant value at fairly early stages. Results for the original and larger domains differ by $\sim 16\%$ for the $a = 2.0 \times a_{\min}$ case, and $\sim 18\%$ for the

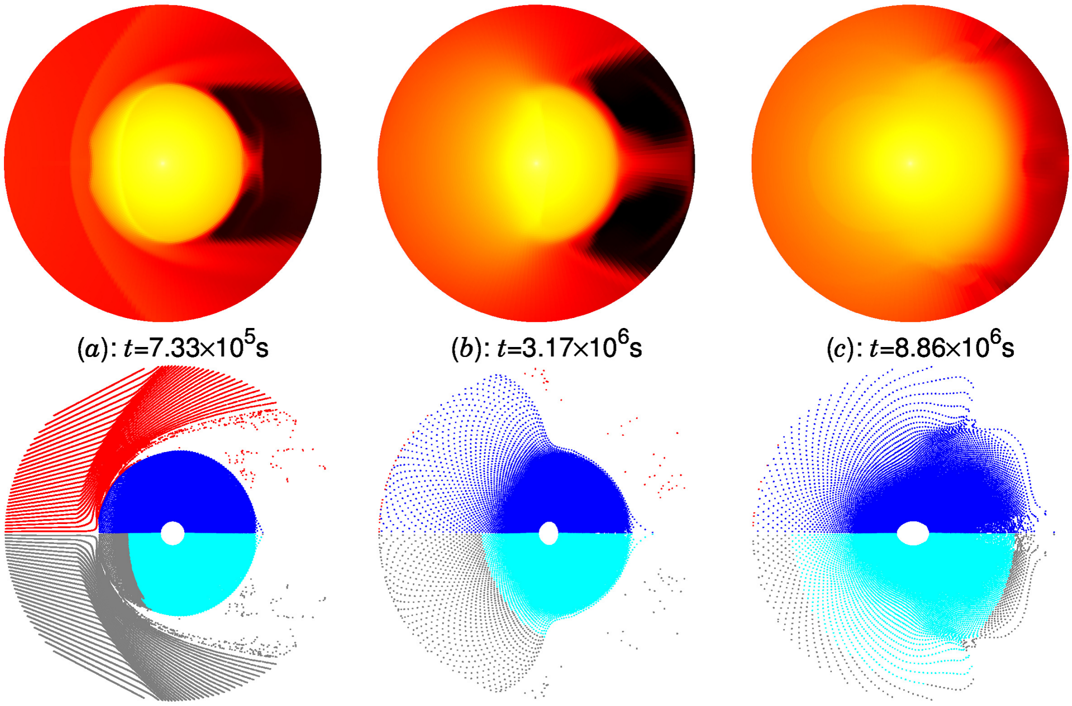

(a): t=7.33×10^{5}s (b): t=3.17×10^{6}s (c): t=8.86×10^{6}s

Figure 2.11: Time evolutions of the density distribution (*upper panels*) and tracer particle distribution (*lower panels*) for the model with $a = 1.5 \times a_{\rm min}$. The same colour bar is used for density as in Figure 2.6. The particles are classified with the same colours as in Figure 2.8.

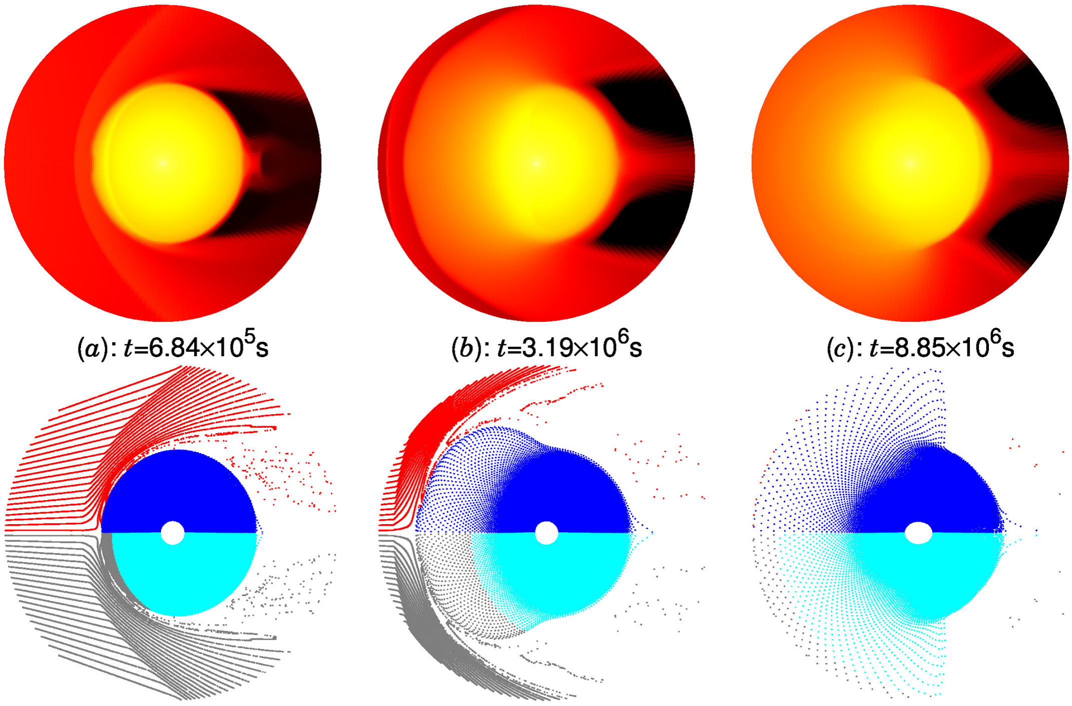

Figure 2.12: Time evolutions of the density distribution (*upper panels*) and tracer particle distribution (*lower panels*) for the model with $a = 2.0 \times a_{\min}$. The same colour bar is used for density as in Figure 2.6. The particles are classified with the same colours as in Figure 2.8.

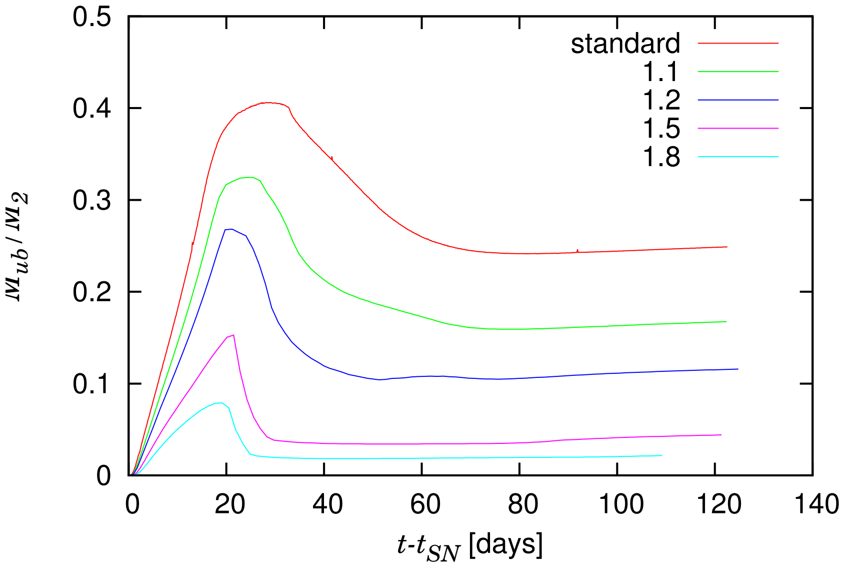

Figure 2.13: The time evolutions of removed mass are shown for several models. The removed masses are evaluated by the Bernoulli criterion. The time is measured from SN explosion. The termination times for the simulations shown here are 122, 122, 125, 121, 109 days respectively.

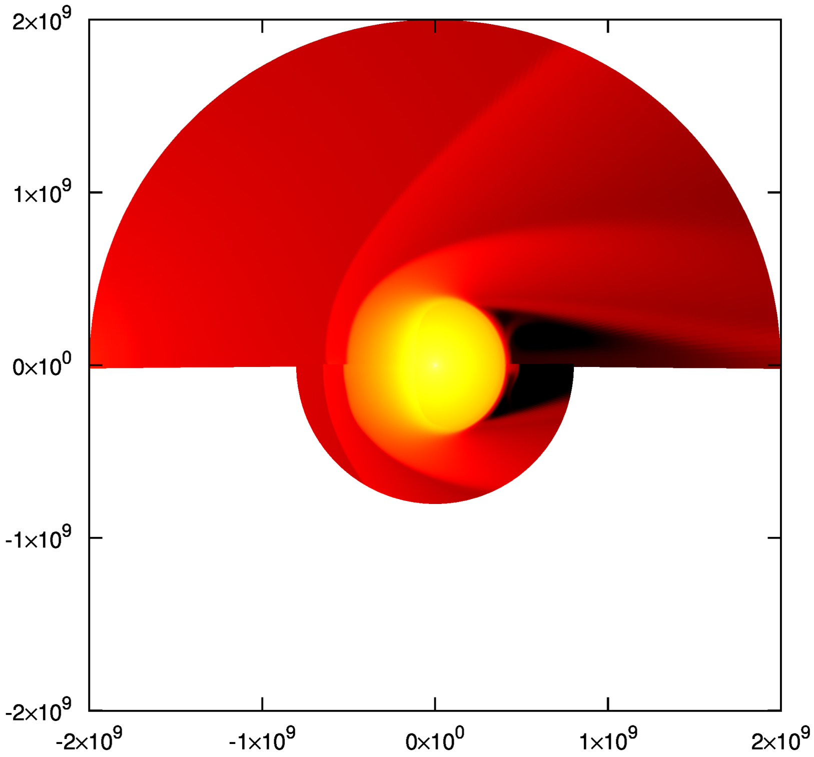

Figure 2.14: A comparison of density distributions in the larger-domain run (*upper half*) and the original domain run (*lower half*) for the $a = 2.0 \times a_{\rm min}$ model. The axes are in units of kilometres. The time is 2.22×10^6 s.

$a = 2.5 \times a_{\rm min}$ case. This indicates that the size of the computational domain does not affect the removed mass significantly, but that we need to wait for the shock to penetrate the opposite side of the companion to obtain precise amounts. It can also be observed that the unbound masses evaluated by both criteria do converge to the same asymptotic value at sufficiently later periods.

We plot the removed mass as a function of separation in Figure 2.16. The red circles indicate the results obtained here. Consistent with the previous studies on type Ia SNe in binaries, the removed mass decreases as the binary separation increases, following the power law:

$$\frac{M_{\rm ub}}{M_2} = C_{\rm ab} a^{m_{\rm ab}}, \tag{2.4}$$

where $M_{\rm ub}$ is the unbound mass, M_2 the companion mass, $C_{\rm ab}$ and $m_{\rm ab}$ fitting parameters. The solid line in Figure 2.16 is the best fit for the models with close separations and has $C_{\rm ab} = 0.26$ and $m_{\rm ab} = -4.3$. The absolute value of $m_{\rm ab}$ is slightly larger than the values -3.66 to -2.92 previously obtained by Pan et al. (2012) for main sequence and helium star companions, and -0.416 to -0.391 for red giant companions.

2.4 Discussions

As an attempt to understand the value of the parameter $m_{\rm ab}$, we conducted several experimental calculations varying several physical parameters of SNE. As mentioned

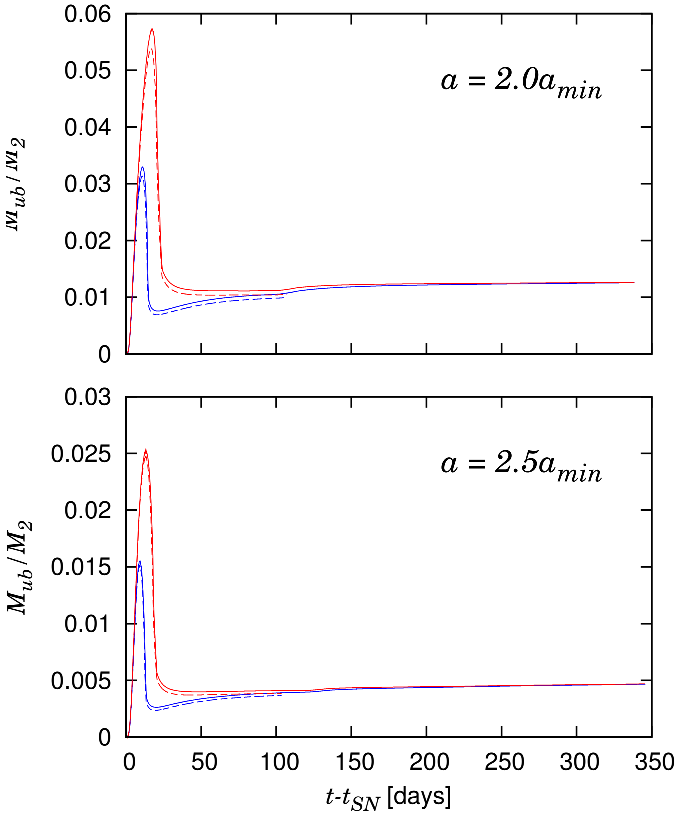

Figure 2.15: Time evolutions of the removed mass for the larger-domain runs. Results for the $a = 2.0 \times a_{\rm min}$ model is shown on the upper panel, and $a = 2.5 \times a_{\rm min}$ on the lower panel. Red lines show the removed masses estimated by the Bernoulli criterion, and blue lines by the escape criterion. Results of the original domain are also plotted with dashed lines.

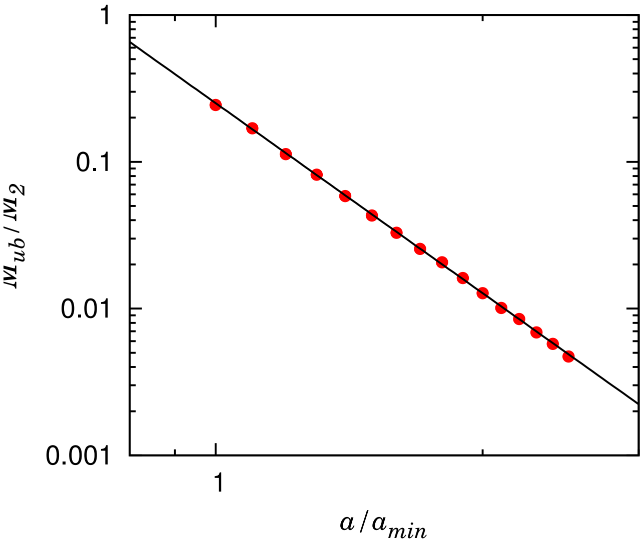

Figure 2.16: The removed mass as a function of binary separation. Red dots indicate the numerical results. The solid black line is a fit for the results ($\propto a^{-4.3}$).

already, the quantities that change with the binary separation are the solid angle of the companion, the density and pressure of SNE, and the time until the bulk of SNE flows past the companion star. The mass and energy contained in the solid angle also vary as a result of these changes. Since kinetic energy dominates in SNE, we ignore the dependence on the incident pressure and internal energy in the following.

We first pay attention to the incident density. As the binary separation increases, it decreases as a^{-3}. Since the solid angle of the companion also decreases as a^{-2}, the mass and total energy contained in the solid angle would be reduced even if the density were unchanged, which could have a big impact on the mass loss. In order to see the dependence of the removed mass on the incident density alone, though, we artificially amplified the density of the SNE by a factor of 1.2, 1.5, 1.8 and 2.0, without changing other physical values including separation. Note that this modification still increases the kinetic energy as well as the momentum of the SNE that collide with the companion. These experiments were carried out for models with separations of $(1.0, 1.3, 1.5, 1.8, 2.0) \times a_{\rm min}$.

Their results are shown in Figure 2.17, in which the removed masses are plotted against $(C_{\rm amp}(a/a_{\rm min})^{-3}) \propto \rho_{\rm ej}$, where $C_{\rm amp}$ is the amplification factor of density and the last factor $(a/a_{\rm min})^{-3}$ accounts for the decline in density according to expansion of the SNE. It can be seen that almost all models lie on a single line in the log − log plot, which has a power law index of 1.4. This suggests that the removed mass depends solely on $\rho_{\rm ej}$ irrespective of separation as

$$M_{\rm ub} \propto \rho_{\rm ej}^{1.4}. \tag{2.5}$$

This means that the mass and/or total energy injected into the solid angle of the companion star are not very important. These results seem to be at odds with the analytical estimates $M_{\rm ub} \propto M_{\rm SN} a^{-2}$ by Wheeler et al. (1975), in which $M_{\rm SN}$ is the total ejecta mass and corresponds to $C_{\rm amp}$ in our case. Models with the highest $\rho_{\rm ej}$ start to depart from the power law. This is because the removed mass becomes comparable to the remaining mass, thus modifying the escape velocity significantly.

Next we artificially multiplied v^2 by a factor of $1.2, 1.5, 1.8, 2.0$ as we did with density. The binary separation was fixed to $a = 1.3 \times a_{\rm min}$ this time, implying that the solid angle of the companion and hence the density of SNE are unchanged but the incident kinetic energy is still increased, which is expected to have a similar effect to the enhancement of density. We also tried different combinations of these two effects so that the kinetic energy of the entire SNE would be fixed.

The results for these tests are summarized in Table 2.2. It is evident from the vd-series, in which only the velocity was changed, that the removed mass increases as the velocity rises just as expected. Interestingly, the comparison between the vd-series and the dd-series, in which we varied density alone, reveals that if the change in kinetic energy is the same, changing velocity has a slightly larger effect on the amount of removed mass than changing density. This is also vindicated by the ef-series, in which both density and velocity were modified but the kinetic energy was fixed. The latter result may imply that increase in the incident momentum decreases removed mass as long as the incident kinetic energy is identical.

Now we know how the density and/or velocity of SNE affect the removed mass, our next question will be - why? We have observed that direct mass stripping was extremely inefficient in our models because the SNE is directed away from the com-

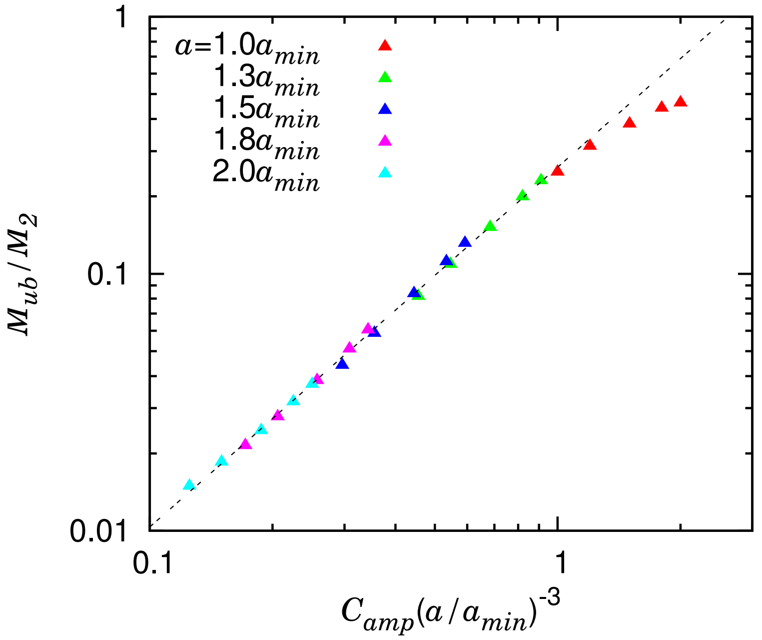

Figure 2.17: Removed mass vs incident density of SNE. Plots with the same colour are the results of models with the same separation. The dashed line shows a power law with a power-law index of 1.4.

Table 2.2: Results for the experimental computations

model	$\rho_{\rm ej}$	$v_{\rm ej}^2$	$E_{\rm ej}$	$M_{\rm ub}(\rm M_\odot)$
base	1.00	1.00	1.00	0.866
dd1.2	1.20	1.00	1.20	1.107
dd1.5	1.50	1.00	1.50	1.578
dd1.8	1.80	1.00	1.80	2.069
dd2.0	2.00	1.00	2.00	2.404
vd1.2	1.00	1.20	1.20	1.136
vd1.5	1.00	1.50	1.50	1.659
vd1.8	1.00	1.80	1.80	2.212
vd2.0	1.00	2.00	2.00	2.592
ef1.2	1.20	0.83	1.00	0.798
ef1.5	1.50	0.67	1.00	0.770
ef1.8	1.80	0.56	1.00	0.746
ef2.0	2.00	0.50	1.00	0.731

ρ, v^2 and $E_{\rm ej}$ are the values of the SNE normalized by the values of the base model but with $a = 1.3 \times a_{\rm min}$.

Ejecta	Star
ρ_1:variable	$\rho_2 = 1 \times 10^{-8}\mathrm{g/cm^3}$
$p_1 = 1 \times 10^{-2}\mathrm{erg/cm^3}$	$p_2 = 1 \times 10^{6}\mathrm{erg/cm^3}$
$v_1 = 3 \times 10^{8}\mathrm{cm/s}$	$v_2 = 0\ \mathrm{cm/s}$

Figure 2.18: Illustration of the Riemann problem.

panion star once the bow shock is formed. Most of the mass loss occurs instead by ablation owing to the shock heating of stellar matter. This means that the energy, not the momentum, imparted to the companion star is most important. Then the shock strength will be the physical parameter that we should look into, since it determines how much the star will be heated.

To see how the shock strength depends on the incident density, we consider a Riemann problem as presented in Figure 2.18. This is meant to be a very crude approximation to the collision of SNE against the companion star. The left side of the initial discontinuity represents the SNE, taking typical values of pressure and velocity from our simulation ($p_1 = 1\times10^{-2}, v_1 = 3\times10^{8}$). We vary ρ_1 to see how this affects the strength of the forward shock produced by collision. For the right state approximating the envelope of the companion star, we use average values of density and pressure from our companion model: $\rho_2 = 1\times10^{-8}, p_2 = 1\times10^{6}, v_2 = 0$. Here CGS units are adopted. We assume that the companion star is at rest. We employ the same assumption as in Cheng (1974) to determine the maximum value of ρ_1: the ejecta mass is distributed in a uniform shell with a thickness of $\frac{1}{3}$ the shock radius. This gives us the maximum density as a reference:

$$\rho_{\mathrm{ej}}^{\mathrm{max}} = \rho_{\mathrm{ej}}(a_{\mathrm{min}}) = \frac{27}{19}\frac{3M_{\mathrm{ej}}}{4\pi a_{\mathrm{min}}^3}, \tag{2.6}$$

where M_{ej} is the mass of SNE.

The solutions of the Riemann problem are given in Figure 2.19. The left panels show the pressure distributions and the right panels show the density counter part. Each row hold results for different initial conditions, i.e. $\rho_1 = \rho_{\mathrm{ej}}^{\mathrm{max}}$ for the top panels, $\rho_1 = \rho_{\mathrm{ej}}^{\mathrm{max}}/1.5$ for the middle panels, and $\rho_1 = \rho_{\mathrm{ej}}^{\mathrm{max}}/2.0$ for the bottom panels. The different colours of lines correspond to different times. We can see jumps in density and pressure at the positions of the forward shock propagating through the companion star and sweeping up mass. There is also a reverse shock propagating away from the companion into the SNE, which tries to push it back toward the star. A contact surface divides the SNE from the companion and density but not pressure has a jump there. The region between the forward and reverse shocks corresponds to the matter heated by one of these shocks. Figure 2.20 shows the pressure divided by the post-shock density ρ_{sh}, a measure of the shock strength, as a function of ρ_1. We again find a power law, whose exponent is rather sensitive to the value of ρ_2.

In our simulations, the forward shock initially has a rather flat front perpendicular to the symmetry axis. It maintains a nearly constant speed until the reverse shock starts to expand toward the primary star. This launch of the reverse shock is accompanied by the generation of a rarefaction wave, which in turn propagates towards the forward shock. It eventually catches up and sucks the energy that would otherwise be

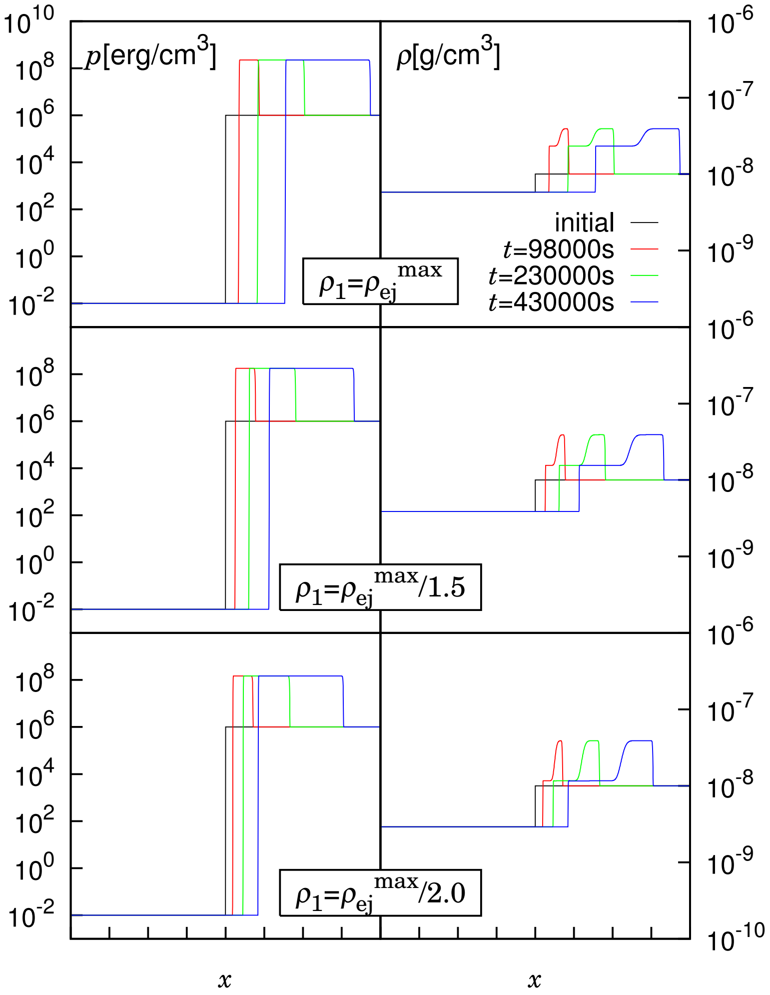

Figure 2.19: Solutions of the Riemann problem given in Figure 2.18. Left panels show distributions of pressure while right panels display those of density. *Top* : results for $\rho_1 = \rho_{\rm ej}^{\rm max}$, *Middle* : $\rho_1 = \rho_{\rm ej}^{\rm max}/1.5$ and *Bottom* : $\rho_1 = \rho_{\rm ej}^{\rm max}/2.0$. Different lines correspond to different times.

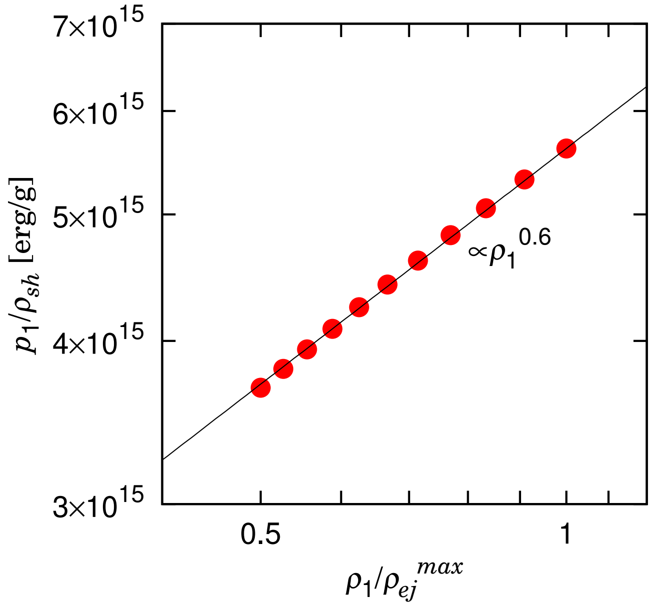

Figure 2.20: Pressure of the shock-heated region as a function of ρ_1.

injected to the shock. It is hence natural to expect that the total energy given to the companion is determined at this point.

Based on the above observation, we estimate the removed mass as follows. Figure 2.21 displays a schematic picture that gives the idea and notations we use here. Assuming that the shock front is a plane perpendicular to the symmetry axis, we approximate the shock-heated portion of the companion star by the shaded region in the picture. X is the distance from the stellar surface to the shock front and $M_{\rm heat}$ is the mass contained in this shocked region. We show in Figure 2.22 $M_{\rm heat}$ as a function of X calculated as

$$M_{\rm heat}(X) = \int_{r\cos\theta > X} \rho(r) dV. \tag{2.7}$$

It is probably by coincidence that this function can be fit by a simple power law very well, which allows us to approximate $M_{\rm heat}$ as

$$M_{\rm heated} \propto X^3. \tag{2.8}$$

If we assume that the shock propagates at a constant velocity, we have $X = v_{\rm sh}t$, in which t is the time after collision. As argued earlier, the main shock heating stops at $t = t_{\rm heat}$, when the reverse shock starts to expand outwards. We find in our models that $t_{\rm heat}$ roughly corresponds to the time, at which the instantaneous unbound mass reaches the maximum (see Figure 2.13), and that this time does not differ so much among models. Hence assuming that $t_{\rm heat}$ is constant, we obtain $M_{\rm heat} \propto v_{\rm sh}^3$ at $t = t_{\rm heat}$.

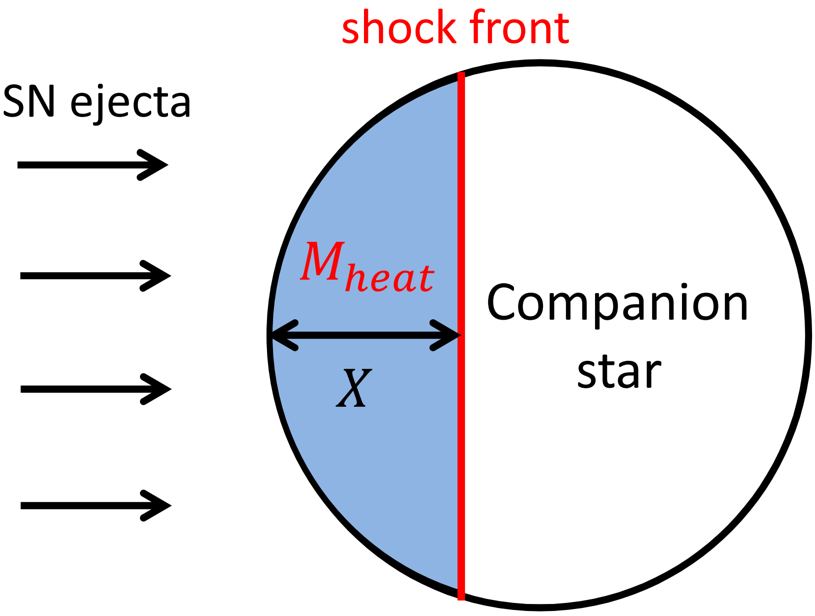

Figure 2.21: A schematic picture of shock propagation through the companion star. The shaded region is the shock-heated material, whose mass is referred to as $M_{\rm heat}$. The distance from the shock front to the stellar surface is denoted by X.

The total energy, $E_{\rm heat}$, deposited by the forward shock is estimated as follows,

$$\begin{aligned} E_{\rm heat} &= \epsilon_{\rm sh} \cdot M_{\rm heat}, \\ &\propto \rho_{\rm ej}^{0.6} \cdot v_{\rm sh}^3, \\ &\propto \rho_{\rm ej}^{0.6} \cdot (\rho_{\rm ej}^{0.3})^3, \\ &\propto \rho_{\rm ej}^{1.5}, \end{aligned} \tag{2.9}$$

where $\epsilon_{\rm sh}$ is the specific internal energy and is assumed to be proportional to $p_1/\rho_{\rm sh}$; in the second line we employed the relations $M_{\rm heat} \propto v_{\rm sh}^3$ just obtained and $p_1/\rho_{\rm sh} \propto \rho_{\rm ej}^{0.6}$ in Figure 2.20. In the third line, on the other hand, we made use of the approximation $v_{\rm sh}^2 \propto p_1/\rho_{\rm sh}$. This energy is redistributed in the removed mass via hydrodynamical interactions. It is hence natural to assume that the removed mass is proportional to $E_{\rm heat}$. This hypothesis finally leads us to the relation $M_{\rm ub} \propto \rho_{\rm ej}^{1.5}$, which is pretty close to the power law with $m_{\rm ab} \sim 1.4$ (see Eq.(2.5)) obtained in the simulations.

In our simulations, we cut out the central core of the companion star. Although this makes it difficult to accurately estimate the kick velocity imparted by the SNE, it is still possible to make rough estimations on this so called "rocket effect" (Cheng, 1974). We calculate the imbalance between the total momentum that flows in from the ejecta side and the momentum that flows out of the other side and find that it is $\sim 2 \times 10^{38}$g $\cdot$ km/s for the base model with $a = a_{\rm min}$. This should be equal to the momentum deposited to the remnant of the companion star. The kick velocity obtained this way is $v_{\rm kick} \sim 2 \times 10^{38}/(M_2 - M_{\rm ub}) \sim 100$ km/s, which is comparable to the orbital velocity ~ 50 km/s and could destroy the binary system. Note, however, this will be an upper limit, and it decreases as $\propto a^{-2}$ with the binary separation according to the solid angle of the companion.

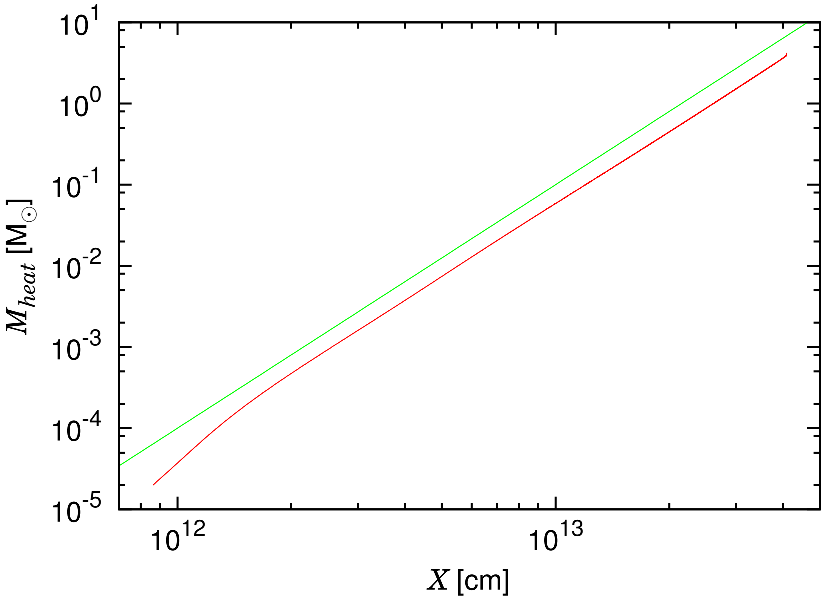

Figure 2.22: M_{heat} as a function of X (red line). The green line is a power law X^3.

2.5 Summary

We have performed hydrodynamical simulations of SNe in binary systems. The removed mass can reach up to approximately 25% of the original mass, and decreases according to a power law of the binary separation. The power is determined by the incident density, which decides the strength of the bow shock.

The effect of SNE hitting the companion star can become non-negligible at close separations. Such close separations can be created by common envelope evolution, or mass accretion from a tertiary star (de Vries et al., 2014). It is also known from observation that the orbital periods of massive binaries range $\sim$ 1 day to $\sim$ 3000 days, with a preference for short periods, meaning that binaries with close separations are popular (Sana et al., 2012). When such mass is removed from the companion star, it could alter the evolution from then on. It could change the type of SN if the companion is large enough to cause CCSNe, or could induce kicks.

Simulations with more realistic binary models will be useful for future detections of surviving companions in SNe such as iPTF13bvn, SN1993J etc. Observations of SN1993J suggest that the companion star was a B type star (Maund et al., 2004; Fox et al., 2014), which is more compact compared with the companion model in this study. Mass stripping off this compact companion star will surely be less efficient if placed at the same separation as in our simulations. This system may have been fairly close, though, since the companion must have a smaller stellar radius. Since the removed mass strongly depends on incident density and/or velocity rather than the a/R ratio, more mass might have been stripped off this companion by SNE despite its compactness.

We have not studied the further evolution of the binary as a system, in our simulations. The sudden mass loss should lead to high eccentricities, or could destroy the system. But if the system survives, the expansion of the companion may engulf the remaining neutron star, leading to common envelope evolution (Liu et al., 2013a).

This could create even closer separations, possibly forming HMXBs. After a short time, the secondary star will reach its end of evolution, and cause the second SN. If it is possible for the system to survive this explosion, it may lead to the formation of NS-NS binaries or NS-BH binaries. This study may be the first step to possibly reveal some necessary conditions in forming these compact binaries.

"Measure what is measurable, and make measurable what is not so."
Galileo Galilei (1564–1642)

3

Ejecta-Companion Interaction in iPTF13bvn

3.1 Introduction

Type Ib supernovae (SNe) are one of the hydrogen deficient subtypes of core-collapse supernovae, which are the final fates of massive ($M \gtrsim 8\mathrm{M}_\odot$) stars (Filippenko, 1997). Their lack of hydrogen indicates that they explode from stripped-envelope progenitors. Two major scenarios have been proposed to explain the removal of the hydrogen layers. One is by strong stellar winds for stars with zero age main sequence (ZAMS) masses $M_{\mathrm{ZAMS}} \gtrsim 25\mathrm{M}_\odot$ (Maeder, 1981). Such stars are called Wolf-Rayet stars, and are known that they sometimes shed their entire hydrogen envelope with the wind. The other possible scenario is mass transfer in close binaries (Podsiadlowski et al., 1992). Outer layers of the more evolved star in a binary can be transferred to its companion via Roche lobe overflow, or removed dynamically in common envelope phases. Debates continue about which is the more likely scenario.

iPTF13bvn was a recent SN of this particular type, first identified by the intermediate Palomar Transient Factory (iPTF; Law et al., 2009) on June 16.238 UT 2013. Its host galaxy is NGC 5806, which is at a distance ~ 21Mpc. Pre-explosion images of HST showed a candidate progenitor within a 2σ error of the SN site (Cao et al., 2013). It is not settled whether we were looking at the progenitor star itself or a combined flux of a binary, but nevertheless we can place strong constraints on the exploding star.

Groh et al. (2013) first proposed that a Wolf-Rayet star with a ZAMS mass of $31 - 35\mathrm{M}_\odot$ could be a possible progenitor for iPTF13bvn. This result was based on the absolute magnitude of the source in the pre-explosion image, and the strict upper limit on the radius of the progenitor ($\lesssim 5R_\odot$) due to early detection. In their case, the pre-SN progenitor mass was $\approx 10\mathrm{M}_\odot$. This possibility was ruled out by observations of the later phases of the bolometric light curve (Bersten et al., 2014; Fremling et al., 2014). Detailed hydrodynamical simulations of SNe with different progenitors showed that the observed light curve cannot be reproduced by a star with $M \gtrsim 8\mathrm{M}_\odot$. Instead, the preferred model was a He star with $M \approx 3.5\mathrm{M}_\odot$ which is difficult to produce by assuming only stellar winds. The limit on the stellar radius was also extended up to $\lesssim 150R_\odot$ by an additional set of simulations with extended thin envelopes by Bersten et al. (2014) (hereafter B+14). Their results strongly support the binary evolution scenario, and they also showed a possible evolutionary path that can produce such a low mass progenitor star and match the pre-SN HST observations consistently. The SN is estimated to fade below the brightness of the pre-SN primary star at about three years from explosion. A fainter secondary star may be observed shortly afterwards. If a companion star is really discovered, it will be the first case that the progenitor for a SNIb is confirmed to be a binary.

According to the binary evolution calculations by B+14, the secondary star is predicted to be an overluminous OB-type star. The combined optical flux of the primary and the secondary was consistent with the optical flux from the pre-SN image. However, the SN ejecta may change the observable features of the companion after the explosion by stripping mass, or heating the star to make it swell up (Hirai et al., 2014). This effect was not included in previous predictions although it may significantly alter its appearance.

In this chapter we investigate the possible effects of SN ejecta hitting the companion in iPTF13bvn, and how it may affect the observational features. Such events have been thoroughly studied for the single-degenerate scenario of Type Ia SNe (Marietta et al., 2000; Podsiadlowski, 2003; Pan et al., 2013; Liu et al., 2013b; Shappee et al., 2013), but not so much for massive binaries. Especially for relatively wide binaries, which does not fit in the picture of the single-degenerate scenario, not much attention has been paid. Here we first model binary systems that fit within the constraints placed by B+14 via stellar evolution calculations, and then carry out hydrodynamical simulations of the SN ejecta colliding with the companion star. To obtain the stellar structures at the time it becomes visible in the ejecta, we then performed additional stellar evolution simulations with extra heat distributed in the outskirts of the star. Parameters for the artificial heating was evaluated from the hydrodynamical simulations.

This chapter is structured as follows: Our choice of model parameters and numerical method are explained in Section 3.2, results of our evolution and hydrodynamical simulations are explained in Section 3.3, and we discuss our results in Section 3.4. We summarize our conclusions in Section 3.5.

3.2 Models and Numerical Method

B+14 revealed that the progenitor mass of iPTF13bvn should be in the range of $3-5\mathrm{M}_\odot$, presumably $\approx 3.5\mathrm{M}_\odot$. By detailed binary evolution calculations, they also placed constraints on the initial configuration of the binary system that can produce such stripped envelope progenitors in this mass range. According to their estimates, the initial primary star (progenitor) mass should be $15 \lesssim M_1^i \lesssim 25\mathrm{M}_\odot$, and the mass ratio $0.8 \lesssim M_2^i/M_1^i \lesssim 0.95$. Note that the lower bound of the mass ratio is not physically motivated, but set to avoid common envelope phases since they could not handle common envelope evolution with their stellar evolution code. These constraints overlap with the results by Eldridge et al. (2015), where the permitted primary mass was $10\mathrm{M}_\odot \lesssim M_1^i \lesssim 20\mathrm{M}_\odot$. The overlapping range may be most plausible. They further estimated the possible range of the final secondary mass, being $23 \lesssim M_2^f \lesssim 25\mathrm{M}_\odot$ if conservative mass transfer is implied. This range is expanded to $18 \lesssim M_2^f \lesssim 25\mathrm{M}_\odot$ if mass accretion efficiencies are taken in the range $0.5 \lesssim \beta \leq 1$ where β is the fraction of transfered matter that is accreted onto the secondary star (Benvenuto and De Vito, 2003). The luminosity of the secondary star ended up within the constraint placed by the pre-explosion image of iPTF13bvn.

In this work, we first attempt to construct a pre-SN binary model that fits within the observationally permitted range. We utilize the open source stellar evolution code `MESA` (version 7184; Paxton et al., 2011, 2013) to model each star in the binary. Binary evolution is treated by evolving two spherically symmetric one dimensional stars with a mass transfer rate applied by the "Ritter formalism" (Ritter, 1988). Orbital elements are also evolved consistently. We assume no rotation, no magnetic fields, and circular orbits for all models to maintain simplicity.

It is known that even for identical initial conditions, different stellar evolution codes give different results (Jones et al., 2015; Sukhbold and Woosley, 2014). Since the code employed in B+14 (a code by Benvenuto et al., 2013; Benvenuto and De Vito, 2003) was different from ours, we could not produce the same binary model as the example case in B+14 by taking the same initial conditions. Here we aim to reproduce similar pre-SN configurations as the one shown in B+14, so we take slightly different initial parameters. We also construct several other binary models for comparison. The selected binary parameters are listed in table 3.1, along with the final binary parameters at the moment of SN. For the non-conservative mass transfer models (with $\beta = 0.5$), the angular momentum loss parameter is given as $\alpha = 1$ (Benvenuto and De Vito, 2003). All models were calculated until it starts producing iron at the centre. The stars are assumed to explode within hours after iron production, and binary parameters are unchanged until explosion.

To the pre-SN binary model, we then apply the same method as in Hirai et al. (2014) to simulate the SN ejecta hitting the companion. A two step strategy is employed; 1) artificially explode the primary star on a one dimensional spherical grid, 2) simulate the effect of SN ejecta hitting the companion star on a two dimensional axisymmetrical grid. The hydrodynamical code "yamazakura" (Sawai et al., 2013) is used for all hydrodynamical simulations throughout this work. It is a mesh-based central scheme code with an iterative Poisson solver to solve self-gravity. An ideal-gas equation of state was applied with an adiabatic index $\gamma = 5/3$.

For the first step, $E_{\mathrm{bind}} + E_{\mathrm{exp}}$ of internal energy is added to the inner few meshes of the primary star model placed on a one dimensional computational domain to initiate an explosion like a thermal bomb (Young and Fryer, 2007), where E_{bind} is the gravitational binding energy of the star and E_{exp} is the explosion energy. In order to leave a residual neutron star after the explosion, we cut the central $1.4\mathrm{M}_\odot$ of the star out of the computational region, and set a reflective inner boundary condition. In this way, all the energy applied will be placed just above the neutron star and it will initiate a shock wave that propagates outwards through and out of the star. The explosion energy was taken as $E_{\mathrm{exp}} = 8 \times 10^{50}$erg from the estimate by B+14, which was obtained to fit the peak of the bolometric light curve and photospheric velocity evolution (See also Srivastav et al., 2014, for discussions on the explosion energy). A dilute circumstellar matter is placed around the star due to numerical reasons, with a

Table 3.1: Binary parameters of the stellar evolution calculations with `MESA`.

Model[1]	Age (Myr)	M_1 ($\mathrm{M}_\odot$)	M_2 ($\mathrm{M}_\odot$)	R_1 ($R_\odot$)	R_2 ($R_\odot$)	P (days)	a ($R_\odot$)
a1.0	0	19.0	18.0	5.65	5.47	2.45	25.5
	10.4	3.48	33.5	44.7	7.72	61.7	219
a0.5	0	19.0	18.0	5.65	5.47	2.45	25.5
	10.2	3.72	25.6	47.8	10.4	62.0	203
b1.0	0	18.0	17.0	5.47	5.30	3.50	31.7
	9.98	4.15	30.9	15.4	8.02	47.9	181
b0.5	0	18.0	17.0	5.47	5.30	3.50	31.7
	9.94	4.23	23.9	10.6	7.76	54.4	184
c1.0	0	15.0	14.0	4.93	4.74	3.30	28.7
	12.5	3.02	26.0	31.8	7.01	63.4	206
c0.5	0	15.0	14.0	4.93	4.74	3.30	28.7
	12.5	3.06	20.0	30.4	6.57	73.3	210

Numbers in the model names indicate values of the accretion efficiency parameter β (Benvenuto and De Vito, 2003) applied in our evolution calculations.

low density so as not to disturb the propagation of the SN ejecta. An outgoing outer boundary condition is employed so the ejecta can flow out freely. Ejecta profiles are sampled at a point far from the stellar surface (50 times the stellar radius), and it is checked that it follows a homologous expansion by comparing the time evolution at different points.

In the second step we place the secondary star model onto the origin of an axisymmetric $600(r) \times 180(\theta)$ spherical grid. The axis is taken along the line connecting the centres of both stars. Axisymmetry is justified due to the short timescale of SN ejecta flowing past the star ($\sim$ 1 day) compared to the orbital period ($\sim$ 60 days). Unlike Hirai et al. (2014), we do not leave out the central portion of the star since the companion star model is not so centrally concentrated. The density scale height is resolved with at least 10 meshes, with a total $\sim$ 150 radial gridpoints inside the star. Mesh sizes are then increased monotonically outside the star, until the radius of the computational region reaches up to $\sim$ 90% of the binary separation. Yet again we place a low density atmosphere around the star that is dilute enough so that it has negligible mass. Data from the first step is used to place the SN ejecta close to the companion as an initial condition. For the outer boundary condition, the ejecta data is extrapolated as a Dirichlet boundary on the side facing the primary, whereas a free boundary is applied on the opposite side.

Each mesh is marked as bound or unbound using the "Bernoulli criterion", in which matter is bound when

$$\frac{1}{2}v^2 + \epsilon + \frac{p}{\rho} + \phi < 0 \tag{3.1}$$

where ϵ is the specific internal energy and p is pressure, ρ is density and ϕ is the gravitational potential. We integrate over the bound region to evaluate the mass and

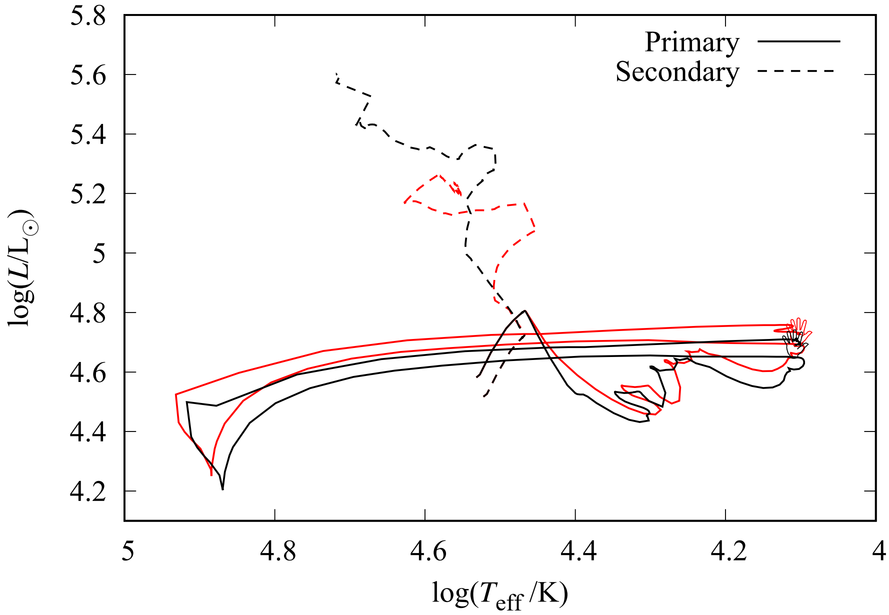

Figure 3.1: Evolutionary tracks of the stellar components in models a1.0 (black lines) and a0.5 (red lines). Solid lines show results of the primary stars, and dashed lines the secondary stars. The star signs label the position of the primary star at the point of SN.

position of the centre of mass of the remaining star. In order to see whether matter from the ejecta can mix with the original stellar matter, we also placed tracer particles that just follow the fluid motion. Each particle carries information of its mass and origin (stellar or ejecta), and is evaluated whether it is bound or not at each step.

3.3 Results

3.3.1 Stellar evolution

In this section we show results of our stellar evolution calculations. Figure 3.1 shows the evolutionary track on the HR diagram of both stellar components for models a1.0 and a0.5. They roughly resemble the track of the model presented in B+14. The overall evolution of the primary does not change much for different values of β, nor does the period of the system. On the other hand, the secondary mass and luminosity depends strongly on the value of β. However, the optical flux is dominated by the primary[1], so it is difficult to constrain the secondary luminosity from the HST pre-SN image. All other models followed similar evolutionary tracks on the HR diagram.

Every primary star model was deficient of hydrogen at the point of SN, which is a necessary condition to produce a type Ib SN. Final luminosities of the primary stars range $4.5 \lesssim L_1^f/L_\odot \lesssim 4.9$, which roughly fits in the allowed range to match the HST pre-SN flux. This is also the case for the companions, with luminosities

---

[1] Even though the secondary star has a higher luminosity, the primary has a stronger optical flux due to the lower temperature.

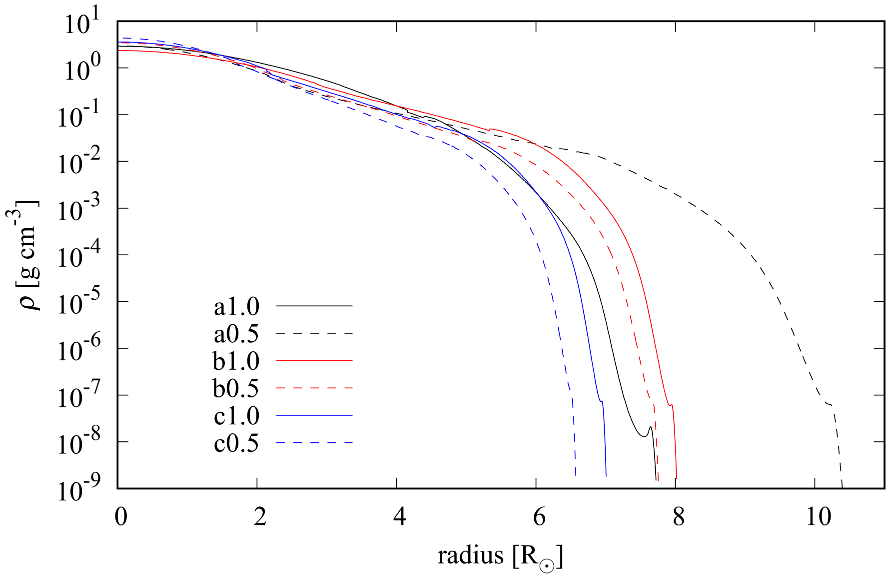

Figure 3.2: Density profiles of the companion star at the point of SN of the primary. Model names correspond to the names in table 3.1.

$4.9 \lesssim L_2^f/L_\odot \lesssim 5.6$. From the above facts, we assume that all of our models can be progenitor candidates of iPTF13bvn. Since the progenitor mass is most likely $\approx 3.5\mathrm{M}_\odot$, we will take model a1.0 to be our reference model. The b series have primary masses close to the lower limit of the observational constraint and the c series close to the upper limit.

Density-radius profiles for each companion star model are compared in Figure 3.2. All models have similar structures, with steep density gradients near the surface and slightly different radii according to their accretion histories.

Obviously, these are not the only models which can reproduce the observational characteristics of iPTF13bvn. Common envelope phases may have occured to produce the compact progenitor, or the orbit may have been eccentric to induce periodic mass loss. Single star models cannot be excluded if we consider stellar rotation (Eldridge et al., 2015). Our stellar evolution calculations do not include these effects, and it is out of the scope of this study to consider every possible scenario.

3.3.2 Supernova

Figure 3.3 shows snapshots of our hydrodynamical simulations of the collision of SN ejecta and the companion star in our reference model. Note that the scales are different in the left and right panels. The whole computational region is displayed in the right panels whereas we show a close-up view in the left panels. Panel *a* shows our initial condition, where the ejecta is just about to reach the companion surface. As the ejecta hits the surface of the companion, a forward shock is driven into the star, and a reverse bow shock is formed in front of the star which can be seen as density discontinuities in Panel *b*. The forward shock heats the outskirts of the star as it proceeds, but the propagation soon stops at a certain point because of the pressure gradient in the star. After the bulk of the ejecta flows past, the bow shock and the heated matter starts to expand outwards as can be seen in the lower half of Panel *c*. We can check whether the stellar matter is expanding, or it is just the bound region that is expanding by looking at the tracer particle distributions. Figure 3.4 shows the distributions of the tracer particles at times corresponding to Panels *b* and *c* in Figure 3.3. The upper half is colour coded according to the origin of each particle, red for ejecta matter that comes from the primary, and blue for secondary star matter. The lower half is colour coded whether it is bound (light blue) or not (grey). We can see that some of the particles from the stellar surface is stripped away along the axis, but the mass is very small. If there are any particles that are red in the upper half and light blue in the lower half, it means that ejecta matter has accreted onto the companion. However, most of the light blue particles in the lower half are blue in the upper half, which indicates that the enlargement of the bound region is not due to ejecta matter being accreted to the stellar surface, but the shocked stellar matter expanding because of the heat. A small amount of ejecta matter is mixed into the stellar matter, but their masses are extremely small. The bound region keeps on expanding in a spherical manner, eventually reaching the outer boundary of our simulation. Panel *d* in Figure 3.3 shows a snapshot at these later stages, where the bound region is almost spherical.

In Figure 3.5 we show the amount of unbound matter ($M_{\rm ub}$), and the displacement of the centre of mass ($\Delta x_{\rm COM}$) as a function of time since SN. As we can see from the upper panel, hardly any matter was stripped off nor accreted onto the star. The absolute values are comparable to the errors arising from the limitation in numerical resolution. This is consistent with previous works (Hirai et al., 2014; Marietta et al., 2000; Pan et al., 2010), where the unbound mass depends on the orbital separation as $\propto a^{m_{\rm ub}}$, where a is the separation. The exponent $m_{\rm ub}$ depends on the stellar structure, but simulations suggest values $-4.5 \lesssim m_{\rm ub} \lesssim -3$. Since our models all have relatively wide separations, it is natural that the amount of stripped mass was so small. The lower panel shows the motion of the centre of mass, which reaches a constant velocity in the direction opposite to the exploding star in about a few days. According to simple estimates (Cheng, 1974; Wheeler et al., 1975), this so-called “rocket effect” or “kick” velocity[2] should be very small in our present model, due to the wide separation with respect to the stellar radius. In our simulation, the kick velocity reached up to 1.75×10^4km h^{-1}, which was $\sim 30\%$ of the orbital velodity. This relatively large kick velocity may help destroy the binary or at least alter the eccentricity of the post-SN system. For model a0.5, the kick velocity was $\sim 5\%$ of the orbital velocity, which is almost negligible. All other models showed qualitatively similar results.

In Table 3.2 we list the amount of unbound mass and the kick velocity along with the final temperature and luminosity which is explained in Section 3.4.1. It is clear that the unbound masses were negligible in every model. The kick velocity was also negligible compared to the orbital velocities. There seems to be no strong correlation between the binary parameters to the unbound mass or kick velocity. This is because the stellar structure and SN ejecta profiles are different for each model, and the absolute values are all comparable to the numerical resolution.

---

[2] The kick velocity mentioned here is different from the natal kick imparted to the central neutron star in core collapse SNe.

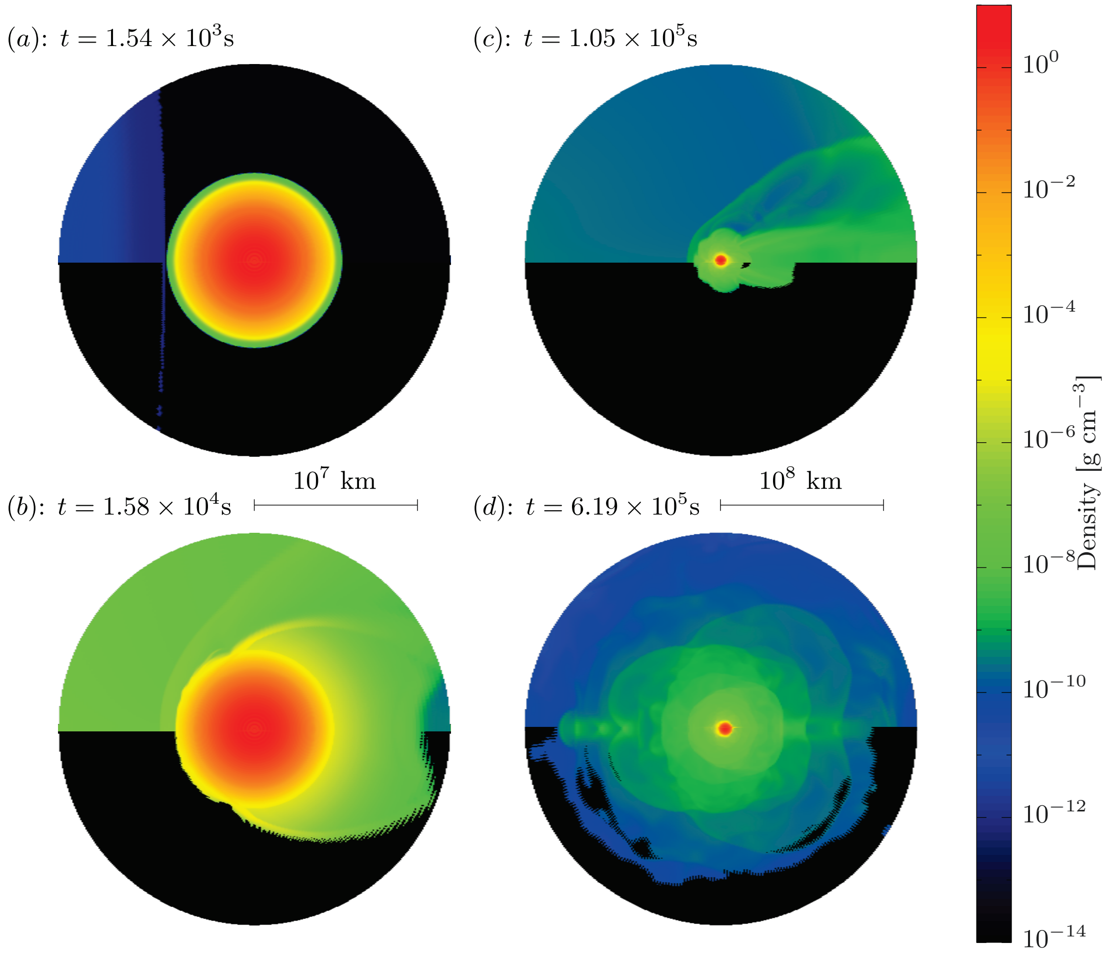

Figure 3.3: Density plots from the hydrodynamical simulations of the collision of SN ejecta and the companion star. Each snapshot is labelled with the time ellapsed since SN. Only the bound matter is coloured in the lower half of each panel. The SN ejecta is flowing in from the left side of each panel. The left panels have a radius of 1.3×10^7km, and right panels 1.3×10^8km.

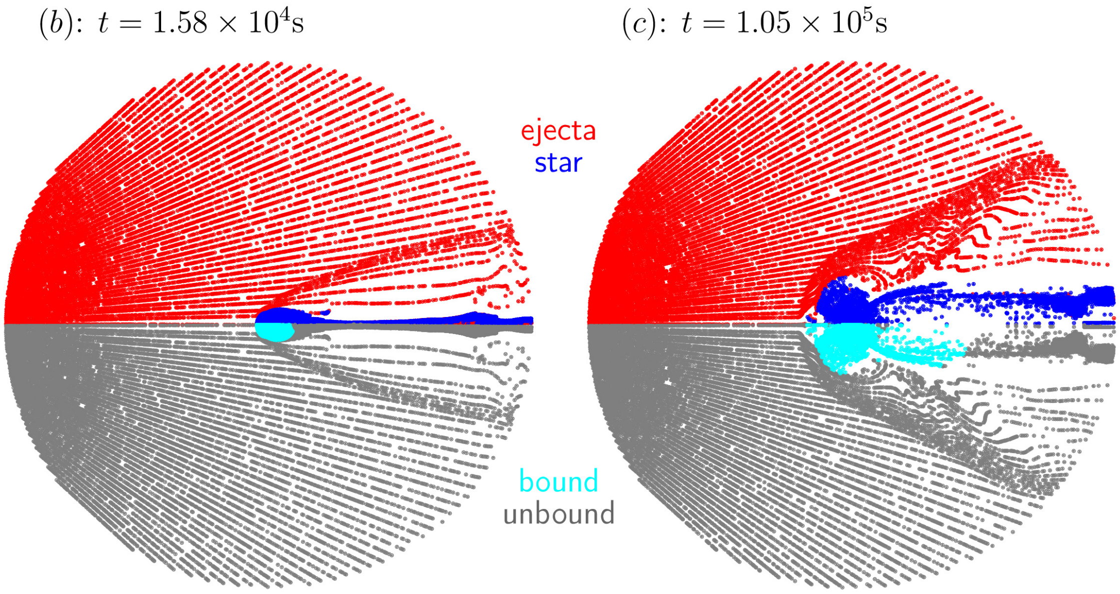

Figure 3.4: Distributions of tracer particles at various times. In the upper half of each panel, each particle is coloured red or blue if they originate from the ejecta or star respectively. In the lower half, particles are coloured light blue or grey depending on whethere they are bound or not. Particles that are red in the upper half and light blue in the lower half are ejecta matter that has mixed into the stellar matter. The radii of the circles are 1.15×10^8km.

3.4 Discussions

The dynamical effects of the ejecta hitting the companion star, such as mass stripping and momentum transfer seem to be limited. But the expansion of the outer layers of the star may become important when we observe the companion after the SN ejecta becomes faint enough. Such expansions have also been found in previous simulations (Hirai et al., 2014; Liu et al., 2013b). Here we explored the observable features of the companion star when it becomes visible.

3.4.1 Reddening due to SN Heating

In Figure 3.6 we illustrate the evolution of the total energy of the star, which we calculate as

$$E_{\rm tot} = \int_{V_{\rm b}} (\phi + \epsilon + v^2)\rho dV \tag{3.2}$$

where V_b is the bound region. The SN ejecta imparts energy to the star via shock heating, and the star adjusts its structure to restore mechanical equilibrium. After a few days, the total energy of the star reached a constant value. We consider that the heating process has finished here, and assume that the difference between the initial and final energy is the amount of energy injected to the star by the SN ejecta.

In our hydrodynamical simulations, the expansion of the star did not cease even at the end of our simulations (a few days) where the bound region reaches the outer

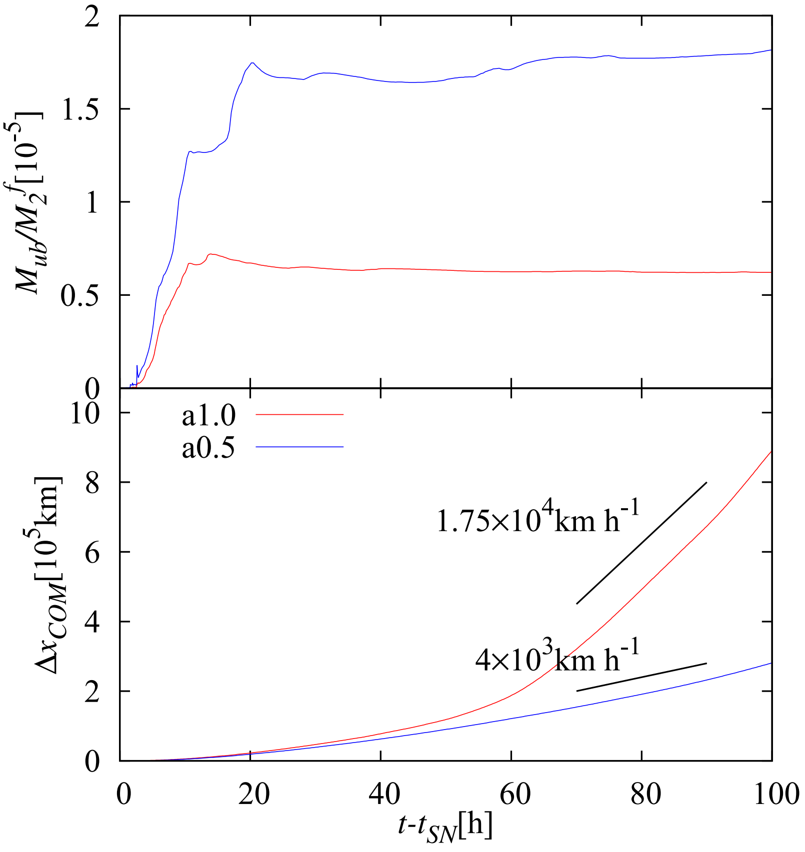

Figure 3.5: Time evolution of the fraction of unbound mass (upper panel) and the displacement of the centre of mass (lower panel). Red lines show results for model a1.0, and blue lines for a0.5. Black slopes in the lower panel show the approximate velocities of the centre of mass.

Table 3.2: Final states of the secondary star.

Model[1]	M_{ub} ($\mathrm{M}_\odot$)	v_{kick} (km h^{-1})	${v_{\mathrm{orb}}}^2$ (km h^{-1})	$\log(T_{\mathrm{eff}}/\mathrm{K})^3$	$\log(L/L_\odot)^3$
a1.0	2.1×10^{-4}	1.8×10^4	6.1×10^4	3.82	5.51
a0.5	4.7×10^{-4}	4.3×10^3	7.6×10^4	3.64	5.65
b1.0	1.1×10^{-4}	5.6×10^3	8.2×10^4	4.01	5.85
b0.5	3.1×10^{-4}	9.1×10^3	9.3×10^4	3.66	5.58
c1.0	0.9×10^{-4}	3.3×10^3	6.1×10^4	3.61	5.57
c0.5	2.2×10^{-4}	5.7×10^3	6.9×10^4	4.22	4.98

[1] Names of models correspond to those in Table 3.1.

[2] The orbital velocity prior to SN.

[3] T_{eff} and L are values estimated three years after SN.

boundary. The numerical cost is extremely expensive to wait for the star to recover equilibrium. Hence we use the stellar evolution code instead of the hydrodynamical code to estimate the state of the star for 100 years after SN. We believe that this is justified because the expansion was almost spherical in the hydrodynamical simulations. This is a similar procedure to previous studies that predicted the post-SN appearance of the companion in type Ia SN progenitors in the single degenerate scenario (Podsiadlowski, 2003; Pan et al., 2012; Shappee et al., 2013).

Starting from the companion model at the pre-SN stage of the *primary*, we artificially input energy into the outer layers as

$$\dot{\epsilon}_{\mathrm{heat}}(m) = \frac{\Delta E_{\mathrm{heat}}}{t_{\mathrm{heat}}\sqrt{2\pi\sigma^2}} \exp\left(-\frac{(m-\mu)^2}{2\sigma^2}\right) \tag{3.3}$$

where ϵ_{heat} is the artificial specific internal energy injection rate as a function of mass coordinate, ΔE_{heat} is the total energy input, t_{heat} is the duration of heating, and $\sigma = (M_2^f - m(r_{\mathrm{in}}))/6$, $\mu = (M_2^f + m(r_{\mathrm{in}}))/2$. r_{in} is the radial coordinate at the inner edge of the heating layer, where the shock could not proceed further inwards in the hydrodynamical simulations. Figure 3.7 illustrates the time evolution of the distribution of specific internal energy along the axis. The black line shows the initial condition, where we can see the ejecta approaching the stellar surface ($\sim 5.3 \times 10^6$km) from the left. The forward and reverse shocks can be seen as a steep wall in the red line, and they weaken their strengths as it proceeds into the star which can be seen in the blue line. The forward shock propagates up to $\sim 3 \times 10^6$km from the centre at most. We can see from the green line, the internal energy distribution near the end of our simulation, that the stellar matter interior to this point is almost unaffected by the shock. We therefore take $r_{\mathrm{in}} = 3 \times 10^6$km as the inner edge of the heating layer. ΔE_{heat} and t_{heat} are also set to the values taken from the hydrodynamical simulations ($\Delta E_{\mathrm{heat}} = 1 \times 10^{50}$erg, $t_{\mathrm{heat}} = 100$hrs). Our strategy of extra energy deposition is similar to Shappee et al. (2013) and Podsiadlowski (2003). The main difference is that we ignore the effects of mass stripping, since the amount of stripped mass in our hydrodynamical simulations are negligible (cf. table 3.2). Due to this assumption, all the energy from the SN ejecta is used to puff up the star, not to ablate away some surface matter.

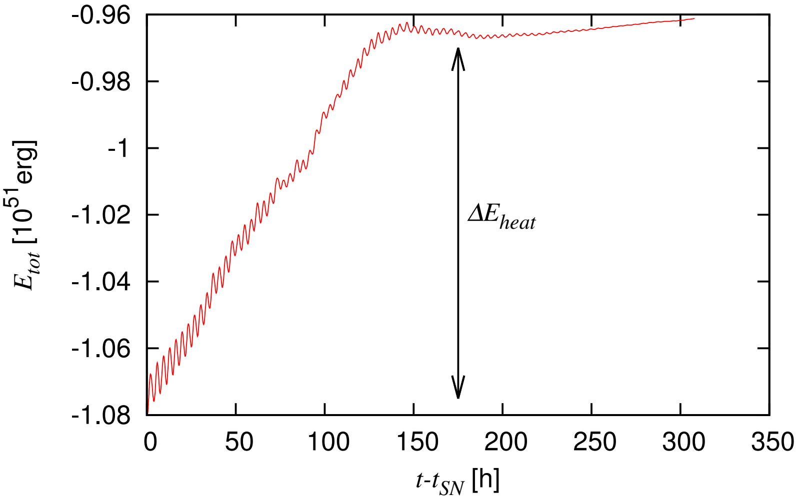

Figure 3.6: Evolution of the total energy of the star. Total energy is evaluated by Eq.3.2 at every time step. The difference between the initial and final energies are considered to be the heat imparted by the SN ejecta $\Delta E_{\rm heat}$.

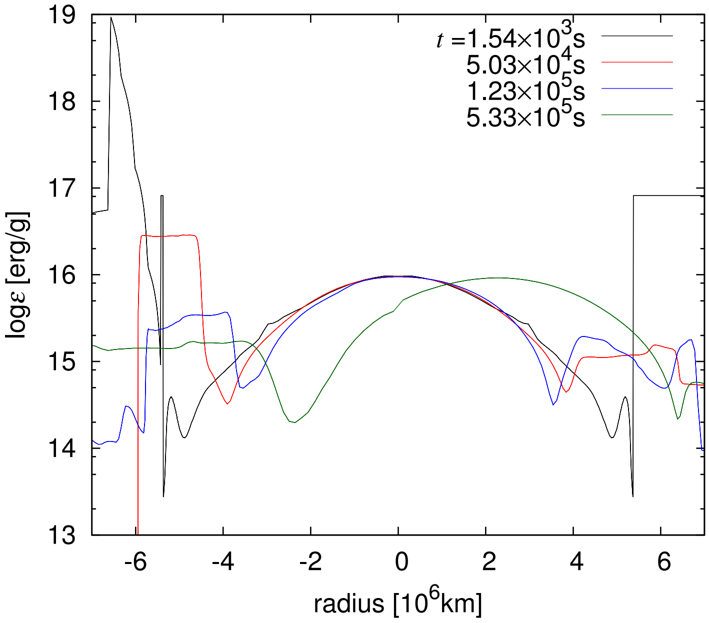

Figure 3.7: Time evolution of the distribution of specific internal energy along the axis. The direction of the axis is taken away from the exploding star.

The shock heating of the outer layers by the SN ejecta modifies the stellar structure, pushing out the outer layers like it did in the hydrodynamical simulations. In Figure 3.8 we show the evolutionary track of the artificially heated companion star on the HR diagram for 100 years after SN. The temperature decreases almost monotonically in the fiducial model (black line). During the heating phase, temperature and luminosity both drops but the luminosity eventually starts to increase due to the growing expansion speed. As soon as we switch off the artificial heating, the temperature and luminosity shows an almost discrete drop because of the disappearance of heat[3]. In the following few dynamical times, the radius and luminosity increases to restore hydrostatic equilibrium. We do not expect these large fluctuations in the early phase to be realistic, since it is highly affected by our methodology. Thus we only pay attention on the evolution after several dynamical times. After a year, the effective temperature will drop by an order of magnitude, and the luminosity slightly increases. It was roughly estimated in B+14 that three years is the time it takes for the SN light curve to decline below the brightness of the original progenitor. The time it takes for the companion to become visible depends on the declination of the SN light curve and the band used for the observation, but we expect that it is not so far from three years, maybe slightly earlier. At that time, it will be somewhere around the middle star sign in Figure 3.8, somewhat like a red supergiant. Even after it becomes visible, we expect the star to continue increasing its luminosity for a few decades.

Although we have carefully chosen our parameters $r_{\rm in}$, $\Delta E_{\rm heat}$, and $t_{\rm heat}$ to match our hydrodynamical simulations, there are still some uncertainties left. Results for the same simulation with different parameters are also shown in Figure 3.8. The final temperature strongly depends on $r_{\rm in}$, where larger values of $r_{\rm in}$ led to lower temperatures and lower luminosity. This is because if $r_{\rm in}$ is larger, the extra energy is injected into a much smaller volume, so it needs to expand more to retain equilibirum. Final states are also sensitive to the value of $\Delta E_{\rm heat}$, which can be seen in Figure 3.8 where results for different $\Delta E_{\rm heat}$ are plotted with different colours. Larger values of $\Delta E_{\rm heat}$ give lower temperatures and higher luminosities. We have also conducted the same simulation with different $t_{\rm heat}$ (black dotted line in Figure 3.8), but the differences were limited. As explained earlier, the early evolution is largely affected by our methodology, particularly on $t_{\rm heat}$, but the differences become indistinguishable within a few dynamical times after the heating phase. We are therefore sure that the long term evolution will not depend on our choice of $t_{\rm heat}$, and any earlier evolution (which is not observable anyway) should be studied by hydrodynamical simulations since it is highly unspherical. Regardless of the uncertainties in our assumptions, the secondary star will appear as a red star when it becomes visible with temperatures lower by a factor of ~2-10, off the main sequence. The parameter dependence of the luminosity is weak, just slightly increasing in some cases by less than a factor of ~2.

Estimates of the final temperature and luminosity for all models are listed in Table 3.2. All other models have considerably lower temperatures compared to their original states. The expansion depends strongly on the stellar structure so it may be possible to distinguish among models from observations.

---

[3] The artificial heat is applied all the way up to the surface, contributing to the surface temperature.

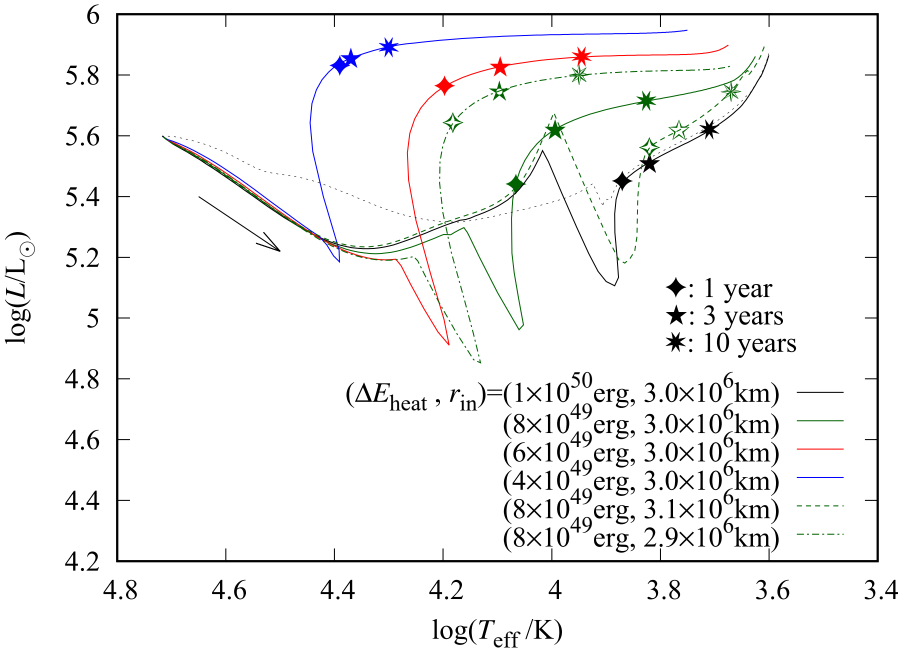

Figure 3.8: Evolution of the secondary star after SN of the primary for model a1.0. The original position is the left end of the lines, and the right ends are 100 years after SN. Star symbols mark the location at 1, 3 and 10 years since SN. Different colours show results with different ΔE_{heat}, and the dashed and dot-dashed lines show results with different r_{in}. The black dotted line shows the evolution of the star with the same heating parameters as the black solid line, but with $t_{\mathrm{heat}} = 0.2$ years.

3.4.2 Other Consequences

The expansion of the star exceeded the original binary separation in some of our models, which means that it may engulf the newly born neutron star. For such cases, the pulsar wind emitted by the neutron star may heat or strip the loosely bound envelope and distort the shape. If the neutron star becomes embedded in the expanded envelope, it might initiate a common envelope phase, possibly leading to much tighter orbits or the formation of Thorne-Żytkow objects (Thorne and Zytkow, 1977). It will be difficult to confirm whether the system has entered a common envelope phase by observations, but if the red super giant-like companion is found and no neutron star is detected for the following couple of years, it may be the first ever evidence of an ongoing common envelope phase.

3.5 Conclusions

iPTF13bvn is a candidate of the first case that the progenitor for a type Ib SN is confirmed to be a binary. There are several possible evolutionary paths that can both reproduce the SN light curve and the pre-SN photometry of iPTF13bvn, all containing a compact ($\lesssim 5\mathrm{M}_\odot$) He star primary and an overluminous OB secondary star. We have studied the effects of SN ejecta colliding with this secondary OB star, and we found that the surface of the star may swell up with the heat, becoming more red and luminous when it becomes visible in the SN remnant. The change in temperature and luminosity strongly depends on the parameters ΔE_{heat} and r_{in} that we used in the post-SN evolution calculations. But in any case the secondary will be found off the main sequence, with lower effective temperatures and a slight increase in luminosity which also depends on the time we detect it. Effects of mass stripping and kicks are limited, and will not affect the further evolution of the binary.

The radius of the secondary star becomes so large that it may engulf the primary-produced neutron star. In that case we might be able to observe the first ever ongoing common envelope phase as an absence of the neutron star in the vicinity.

We note that other evolutionary paths are possible if we include stellar rotation, common envelope phases or eccentric orbits. Theories that can deal with all of these cases have not been established yet and it is much out of the scope of this study (See Ivanova et al., 2013b, for a review on common envelopes). If we concern these possibilities, there is a much wider range of possible progenitors so further studies are certainly warranted.

“No amount of experimentation can ever prove me right; a single experiment can prove me wrong.”
Albert Einstein (1879–1955)

4

Revisiting the Formation Scenario of the Progenitor of iPTF13bvn

4.1 Introduction

iPTF13bvn is the only type Ib supernova (SN) so far known to have a corresponding pre-explosion image. Ever since the first detection by Cao et al. (2013), this pre-supernova (SN) image combined with information from the light curve has helped us deeply constrain the properties of the progenitor star. Hydrodynamical modelling and analytical fits to the light curve show that the ejecta mass was small, corresponding to a progenitor mass of $\sim$ 3–4M$_\odot$ (Bersten et al., 2014; Fremling et al., 2014; Srivastav et al., 2014). Such small mass progenitors are difficult to produce with single star evolution models, so it is now widely accepted that the progenitor had undergone binary interactions (Bersten et al., 2014; Fremling et al., 2014; Srivastav et al., 2014; Eldridge et al., 2015; Eldridge and Maund, 2016).

There are two main channels of binary interactions; Roche lobe overflow and common envelope (CE) phases. Roche lobe overflow is a form of stable mass transfer, in which a Roche lobe filling star spills some of its mass from the outer envelope to the companion star through the inner Lagrangian point. It is not clear how much of the transferred mass will be retained by the accretor, but the secondary will become massive in general. On the other hand, CE phases are the consequence of unstable mass transfer, where the companion star plunges into the envelope of the evolved primary. If there is enough energy in the system to eject the entire envelope of the primary, it will end up as a close binary consisted of the core of the primary orbiting its companion. If not, the plunged-in star will fall to the centre, and can be regarded as a stellar merger. This process was first introduced to explain the formation of X-ray binaries (van den Heuvel, 1976), but it is now commonly used to explain the formation of many close binaries with compact object components (Belczynski et al., 2002; Kalogera et al., 2007).

Earlier works on iPTF13bvn have favoured the stable mass transfer scenario for the formation of the progenitor (Bersten et al., 2014). The initial mass ratio should have been close to unity for the mass transfer to be stable, and in the end the secondary will be much larger as a consequence of the mass accretion. The final companion mass predicted in this scenario was $18 \lesssim m_2/\mathrm{M}_\odot \lesssim 40$, which will be bright enough so that we will be able to detect it three years after the explosion. But it turned out that the expected companion did not show up, ruling out this scenario (Folatelli et al., 2016). After this observation, the CE scenario has now become the current favourite. Eldridge and Maund (2016) has showed some evolutionary models with CE phases which can produce the compact progenitor which is consistent with the pre-explosion image, with a fairly small mass companion. However, the whole process and outcome of CE evolution is still poorly understood, and we should be careful about how we treat CE phases in calculations (Ivanova et al., 2013b, and references therein).

In this chapter we will revisit the observational constraints on the progenitor of iPTF13bvn, and check the relevance of the CE scenario. We find that the CE scenario has a difficulty in explaining the final radius of the progenitor, which may be critical. We then propose another possible scenario which involves stable mass transfer with a black hole (BH) companion, and show some evolutionary tracks that are consistent with observation. This chapter is structured as follows. We will first review the observational constraints on the progenitor of iPTF13bvn in section 2. In section 3 we will reconstrain the progenitor's position on the Hertzsprung-Russel (HR) diagram using the observational data. We will then discuss the relevance of the CE scenario in section 4 and suggest an alternative scenario in section 5. We will summarize and conclude our results in section 6.

4.2 Summary of Observational data

The rich observational data for the SN iPTF13bvn has enabled us to place strong constraints on the properties of the progenitor. In this section we will review and summarize the observational data and the analyses made in previous works.

4.2.1 Host Galaxy Properties

iPTF13bvn was first discovered by the intermediate Palomar Transient Factory in June 2013, in the galaxy NGC 5806. There is a wide scatter in the estimated host galaxy properties among various groups. For the extinction, Cao et al. (2013) suggest a host galaxy colour excess of $E(B-V)_{\rm host}= 0.0278$ mag using Na I D absorption lines from their high resolution spectroscopy data. Bersten et al. (2014) derived a higher reddening value of $E(B-V)_{\rm host}= 0.17 \pm 0.03$ mag, assuming an intrinsic colour law based on observational samples by the Carnegie Supernova Project. This was supported by Srivastav et al. (2014) from a different analysis. Bersten et al. (2014) also measured the Na I D lines and obtained $E(B-V)_{\rm host}= 0.07$ or 0.22 depending on the model used. An intermediate value $E(B-V)_{\rm host}= 0.08^{+0.07}_{-0.04}$ mag was suggested by Fremling et al. (2016), based on an assumption that the intrinsic colour of iPTF13bvn was similar to that of SN2011dh. This is consistent with all other values within the uncertainties.

The distance to the galaxy also holds a large uncertainty. Many works in the literature use $22.5^{+4.0}_{-3.4}$ Mpc, $\mu = 31.76 \pm 0.36$ for the distance and distance modulus which are taken from Tully et al. (2009). More recent works use the updated distance of $26.8^{+2.6}_{-2.4}$ Mpc, $\mu = 32.14 \pm 0.20$ by Tully et al. (2013), or the mean value of all estimates 25.8 ± 2.3 Mpc, $\mu = 32.05 \pm 0.20$ provided by the NASA/IPAC Extragalactic Database (NED). In this work, we adopt $E(B-V)_{\rm host} = 0.08^{+0.07}_{-0.04}$ mag for the extinction value, and 25.8 ± 2.3 Mpc for the distance to the host galaxy.

4.2.2 Pre-Explosion Image

It was first reported by Cao et al. (2013) that they have identified a progenitor candidate at the location of the SN from an observation made by the HST in 2005. Based on their results, various studies were carried out to construct a progenitor model consistent with this pre-SN source and the light curve of the SN itself. Early works showed that they were consistent with a Wolf-Rayet star progenitor (Cao et al., 2013; Groh et al., 2013), but binary progenitors were also suggested later on (Bersten et al., 2014; Fremling et al., 2014; Srivastav et al., 2014). Eldridge et al. (2015) re-analysed the HST data of the progenitor candidate, and found that the reported magnitude by Cao et al. (2013) was lower than that of their analysis by ~ 0.7 mag. Their new magnitude was supported by other following studies (Kuncarayakti et al., 2015; Folatelli et al., 2016). In Figure 4.1 we compare the fluxes calculated from the reported magnitudes by Cao et al. (2013), Eldridge et al. (2015) and Folatelli et al. (2016). It can be seen that the latter two have some overlaps within the uncertainties, but the three results are rather inconsistent with each other overall. It is not clear why there is such a large discrepancy between the different analyses. It is suggested that the differences of the parameters used in the data reduction may have amplified very small errors (Eldridge et al., 2015). The late-time view of the SN position may help us improve our knowledge of the pre-SN image by refining the background information (Maund et al., 2014).

4.2.3 Light Curve

Another constraint can be placed on the progenitor from the light curve of the SN itself. Although there were very high ejecta mass estimates ($M_{\rm ej} \sim 8{\rm M}_\odot$) in the early works (Cao et al., 2013; Groh et al., 2013), the relatively fast decline in the light curve of iPTF13bvn showed that the ejected mass should have been small. According to hydrodynamical modelling, the ejecta mass was estimated to be $M_{\rm ej} \approx 2{\rm M}_\odot$ which indicates that the progenitor was a $M_{\rm He} \approx 3.5{\rm M}_\odot$ He star (Bersten et al., 2014; Fremling et al., 2014). A simple analytical fit also suggested $M_{\rm ej} \sim 1.5$–$2.2{\rm M}_\odot$ (Srivastav et al., 2014).

These analyses ruled out all single star evolution models. The minimum possible mass achieved by single star models with realistic wind mass-loss rates is $\sim 8{\rm M}_\odot$. The only other way to remove the entire hydrogen envelope up to the observed mass is by binary interactions (in our current understandings).

4.2.4 Other Constraints

There are some attempts to infer the zero-age main sequence (ZAMS) mass from late time spectra. The [O I]$\lambda\lambda 6300, 6343$ emission lines can be used to estimate the mass

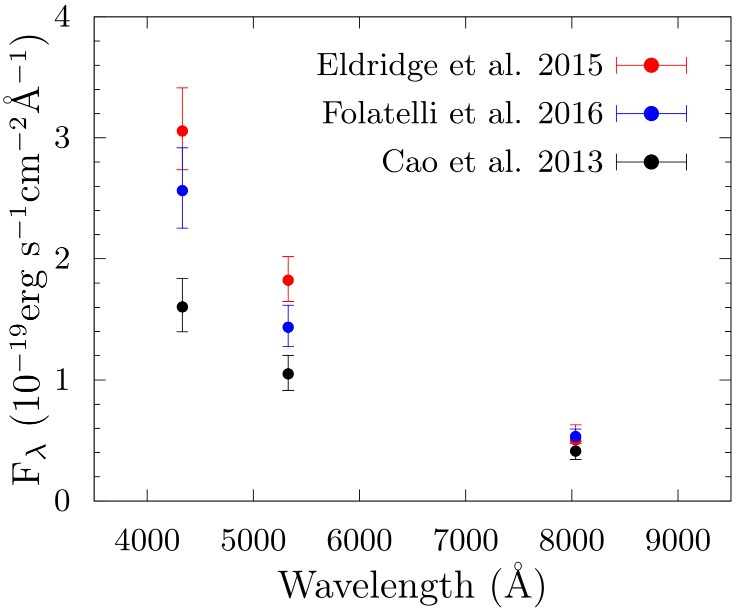

Figure 4.1: Observed pre-SN flux of the location of iPTF13bvn. Each colour shows the reported flux by Eldridge et al. 2015 (red), Folatelli et al. 2016 (blue) and Cao et al. 2013(black).

of ejected oxygen (Jerkstrand et al., 2015). By fitting the late time spectrum with ejecta models, the ejected oxygen mass was estimated to be $\sim 0.3\mathrm{M}_\odot$. Fremling et al. (2016) associated this mass with a star with ZAMS mass $\sim 12\mathrm{M}_\odot$ based on 1D single star nucleosynthesis calculations by Woosley and Heger (2007). Kuncarayakti et al. (2015) derived the ZAMS mass to be $\lesssim$ 15–17$\mathrm{M}_\odot$ using nucleosynthesis models by Nomoto et al. (1997); Limongi and Chieffi (2003); Rauscher et al. (2002). Both values have large uncertainties due to the complexity in modelling the star and explosive nucleosynthesis, but we consider that the latter value is better because the stellar models by Nomoto et al. (1997) are helium star models, and better represent the progenitor of iPTF13bvn than the other models. However, all models do not take into account the possible multidimensional effects such as turbulent mixing in the core, that may change the nucleosynthesis yields significantly (Smith and Arnett, 2014). To quantitatively evaluate the ejected oxygen mass from various progenitor models, hydrodynamic and extensive nucleosynthesis calculations are required, which is much out of the scope of this work. Therefore this constraint should be treated carefully when comparing with stellar models.

Latest observations by Folatelli et al. (2016) have revealed that the progenitor of iPTF13bvn has disappeared, and also placed an upper limit on the brightness of the possible companion. The magnitudes in each band were $m_{\mathrm{F225W}} > 26.4, m_{\mathrm{F435W/F438W}} = 26.62 \pm 0.14, m_{\mathrm{F555W}} = 26.72 \pm 0.08, m_{\mathrm{F814W}} = 26.03 \pm 0.15$ in June 2016. Especially the strict constraint in the F225W band ruled out most luminous companions as predicted in Bersten et al. (2014), and they stated that only late-O type stars with masses $\lesssim 20\mathrm{M}_\odot$ are possible assuming that it is not obscured by newly created dust. Eldridge and Maund (2016) derived a slightly brighter magnitude from the same data, $m_{\mathrm{F438W}} = 26.48 \pm 0.08$ and $m_{\mathrm{F555W}} = 26.33 \pm 0.05$.

4.3 Reconstraining the Progenitor System

4.3.1 Methodology

Using these constraints, we attempt to pin down the position of the progenitor on the HR diagram. We use the reddening law of Cardelli et al. (1989) for the extinction correction, with the standard coefficient $R_{\rm V} = 3.1$ and combining the reddening values from the host galaxy and the Milky way foreground ($E(B-V)_{\rm MW}$= 0.0437 mag; Schlafly and Finkbeiner, 2011). For each combination of luminosity and temperature $(L, T_{\rm eff})$ and assuming that the star can be approximated as a black body[1], we can calculate the flux in each band after applying the extinction correction and giving a distance. If there is a consistent combination of $E(B-V)$ and distance within their uncertainties where all three calculated fluxes fit in the error bars of the observation (see Figure 4.1), we consider the combination $(L, T_{\rm eff})$ is "allowed". This procedure is similar to the selection process of matching models in Eldridge et al. (2015); Eldridge and Maund (2016). However, our selection is more strict since we require to find a combination of distance and extinction value that is consistent for all three bands.

In the same way we can derive a "forbidden" region for the secondary star. We assume that the data obtained by Folatelli et al. (2016) are upper limits. Then for each combination of $(L, T_{\rm eff})$, we calculate the flux in each of the four bands assuming that it is a black body. If the flux in any band exceeds the upper limit, we mark the combination as "forbidden".

4.3.2 HR Diagram Constraints

Figure 4.2 shows the calculated allowed regions for the progenitor on the HR diagram, i.e. the progenitor for iPTF13bvn should have been positioned in the shaded region eight years before the explosion. The size and place of the allowed region strongly depends on which observational data are used. It also depends on the assumed host galaxy properties. For example, in Figure 4.3 we show the same plot but using a smaller distance ($22.5^{+4.0}_{-3.4}$Mpc) to the host galaxy. Smaller luminosities become allowed obviously because of the closer distance assumed. If we take a larger extinction value, the shape of the region will extend to the upper left direction. It should also be noted that the overlapped region is not particularly favoured because the three reported fluxes are not independent observations, but different analyses performed on the same data.

From this analysis only, we can place a stringent constraint on the radius of the progenitor. In Figures 4.2 and 4.3, we have overplotted lines of constant radii. Most parts of the allowed region are within 20–70$\rm R_\odot$. Since the progenitor mass is constrained to very low masses ($\sim 3.5 \rm M_\odot$), the luminosity should not be so high. Therefore, the progenitor had most likely been in the lower right end of the allowed region. This implies that the radius was larger than $\sim 30 \rm R_\odot$.

The forbidden regions for the companion calculated from the post-explosion photometry are shown in Figure 4.4. With the fiducial set of parameters for the host

---

[1] This is a good approximation for low-mass He star progenitors, since they do not have optically thick winds (Yoon et al., 2012). We also assume that the flux is dominated by the primary star in the bands considered here. If the binary companion is on the main sequence, it will be optically fainter than the cool envelope of the low-mass progenitor.

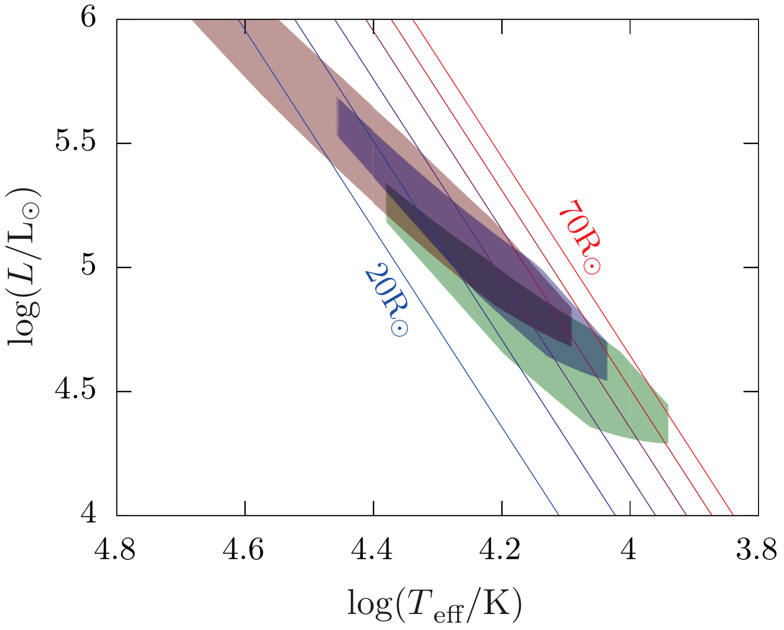

Figure 4.2: Allowed regions of the progenitor of iPTF13bvn on the HR diagram. Colours of the shaded regions show the results that fit the observed magnitudes obtained by Cao et al. (2013, green), Eldridge et al. (2015, red) and Folatelli et al. (2016, blue). Lines correspond to constant radii drawn with intervals of 10 R$_\odot$.

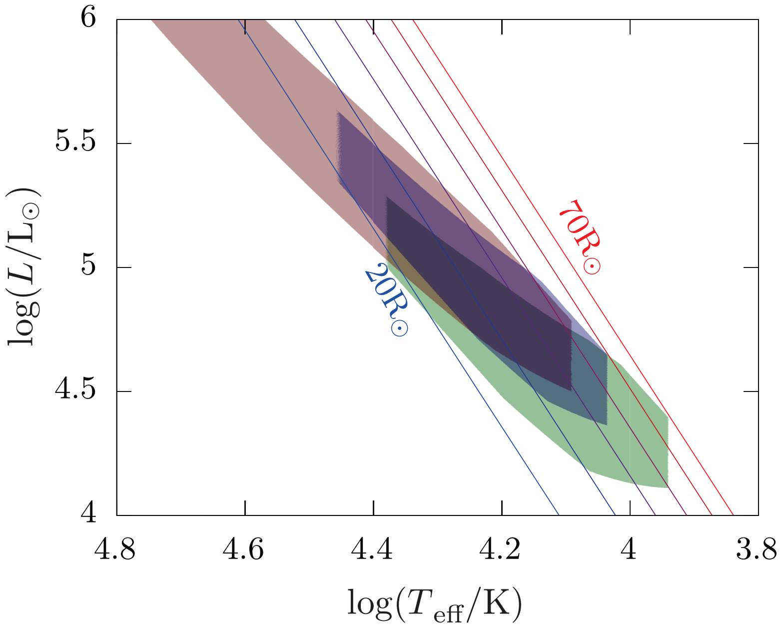

Figure 4.3: Same as Figure 4.2 but calculated using the smaller value ($22.5^{+4.0}_{-3.4}$Mpc) for the distance to the host galaxy.

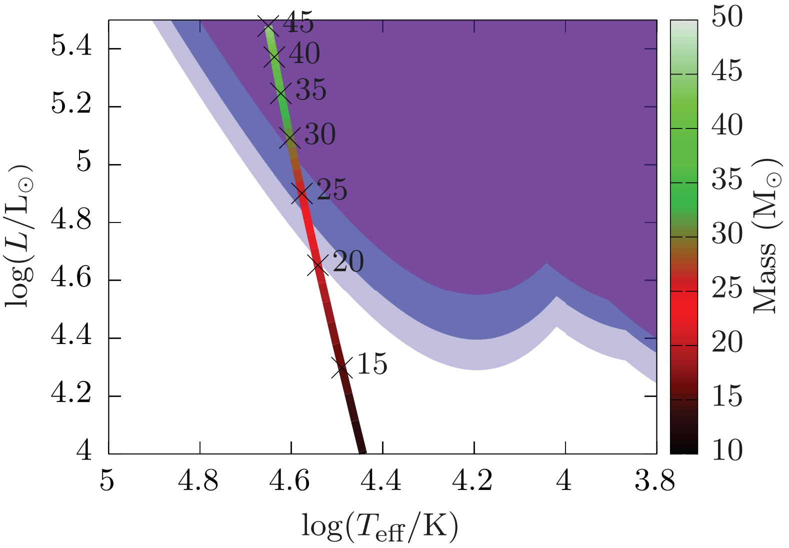

Figure 4.4: Forbidden regions of the possible companion star. calculated from the post-explosion photometry combined with the fiducial parameters for the host galaxy (blue+purple), with a larger extinction value (purple) or with a larger distance (light blue+blue+purple). The line indicates the ZAMS stars coloured according to the mass.

galaxy ($E(B-V)_{\rm host}$= $0.08^{+0.07}_{-0.04}$ mag, 25.8 ± 2.3 Mpc), main sequence stars larger than 23M$_\odot$ can be ruled out. A stricter constraint $m_2 < 20$M$_\odot$ can be placed if the host galaxy is closer ($22.5^{+4.0}_{-3.4}$Mpc), whereas the upper limit goes up to $m_2 < 29$M$_\odot$ if the larger extinction value $E(B-V) = 0.17 \pm 0.03$ is true. It should be noted that these limits are rather overestimated. The line showed in Figure 4.4 is the location of ZAMS stars, but the secondary will at least have an age equivalent to the lifetime of the primary. A star on the main sequence evolves slowly to the upper right in the HR diagram, so stars just outside the forbidden region will slide in eventually. Also, Hirai and Yamada (2015) suggest that the SN ejecta can drive a shock into the companion star, injecting heat to the outskirts of the envelope. The heat excess will puff up the star to larger radii. This can lower the surface temperature temporarily, taking the star to the right on the HR diagram, which will also strengthen the upper constraint. Having these in mind, we consider that the upper limit $m_2 \lesssim 20$M$_\odot$ noted by Folatelli et al. (2016) is reasonable.

As we have seen in the previous section, the progenitor of iPTF13bvn was most likely a ~ 3.5M$_\odot$ He star. Stars that have such a large He core must have had a ZAMS mass of $M_{\rm ZAMS} \gtrsim 10$M$_\odot$. This means that the progenitor should have lost at least $\gtrsim 7$M$_\odot$ of its matter on the course of its evolution. Single star models have been excluded already because strong stellar winds in the Wolf-Rayet phase is not enough to produce such small progenitors (Bersten et al., 2014; Fremling et al., 2014; Srivastav et al., 2014). This leads us to resort to binary evolution models. If the mass was stripped off via stable mass transfer, the companion star should have grown rather large ($18 \lesssim m_2/$M$_\odot \lesssim 45$; Bersten et al., 2014). However, such large companions have been ruled out. The other possible scenario to strip off such a large amount of mass is by experiencing a CE phase. In this way the primary can lose most of its hydrogen envelope, even with relatively small companions. The fact that a CE process is necessary was already suggested by the calculations in Eldridge and Maund (2016). From what we have shown in this section, all the observational facts seem to favour the CE scenario.

4.4 Common Envelope Scenario

We have shown that the progenitor of iPTF13bvn has most likely experienced a CE phase. In this section, we will first briefly review the current status on CE evolution in general. Then we will inspect the CE scenario for the progenitor of iPTF13bvn by modelling the post-CE structures of stars with various ZAMS masses, and checking whether their final position on the HR diagram lies within the allowed region. We use a different treatment for CE evolution from Eldridge et al. (2015); Eldridge and Maund (2016). Using those results, we also discuss the final separation which is strongly related with the CE efficiency and check the ejectability of the envelope.

4.4.1 Common Envelope Evolution

The main focus of CE studies is whether or not the system can eject the envelope. In most population synthesis studies, the outcome is estimated by the "energy formalism" or "alpha-formalism", which is expressed as belows (Webbink, 1984; Iben and Tutukov, 1984).

$$E_{\text{env}} = \alpha_{\text{CE}} \left(-\frac{G m_1 m_2}{a_i} + \frac{G m_{1,c} m_2}{a_f} \right) \tag{4.1}$$

E_{env} is the binding energy of the envelope, G is the gravitational constant, $m_1, m_2, m_{1,c}$ are the masses of the primary, secondary and core of the primary respectively, a_i and a_f are the initial and final separations respectively. It assumes that as the secondary star plunges into the envelope, the orbital energy is somehow transferred to the envelope to unbind it. The mass of the secondary is assumed to be unchanged before and after the CE phase, because the time-scale of the CE phase is much shorter than the thermal time-scale of the secondary, so there will be almost no accretion (Ivanova et al., 2013b; MacLeod and Ramirez-Ruiz, 2015). α_{CE} is a parameter expressing the efficiency of the energy conversion. The value of α_{CE} should be calibrated somehow by observation or theory, but so far there is no guiding principle. Instead, many studies simply take $\alpha_{\text{CE}} = 1$ or leave it as a free parameter to study the dependences of the resulting populations. The binding energy E_{env} is often estimated by

$$E_{\text{env}} = \frac{G m_1 m_{1,\text{env}}}{\lambda R_1} \tag{4.2}$$

where $m_{1,\text{env}} = m_1 - m_{1,c}$ is the envelope mass, and R_1 is the radius of the primary. λ is another parameter introduced to characterize the structure of the star (de Kool, 1990). Although there are several studies deriving a fitting formula for the value of this parameter (Xu and Li, 2010; Wang et al., 2016), many studies combine the uncertainties of the two parameters and simply take $\alpha_{\text{CE}}\lambda = 1$ with no strong reasoning. Given the masses m_1 and m_2, an estimate for the core mass $m_{1,c}$, the initial separation and a value for the parameters, we can calculate the resulting separation a_f of the binary. The criterion for a successful ejection is that both of the post-CE binary components do not overfill their Roche lobes. However, there are still issues regarding the radius of the post-CE remnant (Hall and Tout, 2014).

There are of course some other attempts to understand CE phases such as from observation and simulations. As the secondary plunges into the envelope, it is considered that a small amount of mass is ejected due to the shock created at the interface, and this can be observed as a "luminous red nova". But the typical ejecta mass is very small, making detections difficult due to the low luminosity. The situation has started to change in the past few years, and now there is a rapidly growing number of candidates for the detection of a CE onset (Ivanova et al., 2013a; Chesneau et al., 2014; MacLeod et al., 2016; Blagorodnova et al., 2016). However, much more data are required to be able to constrain CE physics from observation. Hydrodynamical simulations have been performed to investigate the internal physics of a CE phase but the huge dynamical range ($\sim 10^{13}$) makes it extremely computationally expensive. Several groups have already attempted large-scale simulations, but it is still hard to extract general features from the small number of models studied (Ricker and Taam, 2012; Passy et al., 2012; Nandez et al., 2014; Iaconi et al., 2016; Ohlmann et al., 2016a,b).

4.4.2 Post-CE Structure

The progenitor of iPTF13bvn should have a temperature and luminosity in the allowed region shown in Figure 4.2, eight years before the explosion. To see what kinds of stars can end up in this region, we carry out stellar evolution calculations to model the pre-SN state of stars which have experienced CE evolution. All calculations were carried out using the stellar evolution code `MESA` (version 8645; Paxton et al., 2011, 2013, 2015). For convection, we use the mixing length theory, with the Ledoux criterion and a mixing length parameter 1.6. We use the prescription by de Jager et al. (1988) for the wind mass-loss rate. To create post-CE stellar structures, we follow the procedures taken in Ivanova (2011). First, we evolve a star until it enters the hydrogen shell burning phase. Once the stellar radius expands up to a certain value, at which we assume the CE phase kicks in, we search for the mass coordinate of the "maximum compression point" in the hydrogen burning shell $m_{\rm cp}$. This is currently assumed to be the best estimate for the bifurcation point of the core and envelope (Ivanova, 2011; Ivanova et al., 2013b). After that we give an extremely high mass-loss rate of $0.1{\rm M}_\odot{\rm yr}^{-1}$ artificially[2], and wait until the mass drops to $m_{\rm cp}$. Once the mass has dropped to $m_{\rm cp}$, we switch off the artificial mass-loss and evolve the star until it starts burning neon at the centre. A star burning neon will explode within a few more days. The radius at which we start the artificial mass loss is not so important since the time-scale of the expansion is smaller than the time-scale of the core mass growth. This can be checked in Figure 4.5 where we show an example of the evolution of the radius and the core mass in the late stages. The core mass increases by only $\sim 1\%$ during the expansion. Figure 4.5 is for a $17{\rm M}_\odot$ star, but the same applies to all stars in the mass range we used.

In Figure 4.6 we show the evolutionary tracks of our post-CE stars with an initial metallicity $Z = 0.02$. All stars follow similar tracks from ZAMS to the red giant

---

[2] This corresponds to a CE timescale of ~ 100 yr, which is the typical CE timescale.

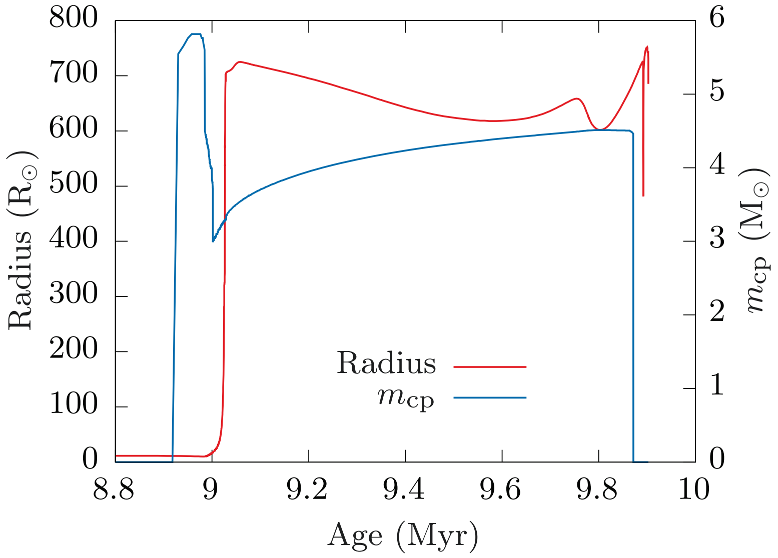

Figure 4.5: Time evolution of the radius and m_{cp} for a $17\mathrm{M}_\odot$ star with metallicity $Z = 0.02$.

phase (dashed line). After that we switch on the artificial mass-loss, and at the end of the CE phase all stars end up on the left end of the HR diagram. Then the stars evolve towards core-collapse. The lighter stars (M_{ZAMS} =15–16$\mathrm{M}_\odot$) evolve from left to right, crossing over the allowed region and then follow very complex paths. This complex evolution is probably not real, so we simply stop our calculation after the track has moved away significantly. The heavier stars (M_{ZAMS} =17–19$\mathrm{M}_\odot$) also evolve with constant luminosity from left to right, but starts to collapse somewhere on the way towards the allowed region. We only plot up to eight years before collapse, since the pre-SN image for iPTF13bvn was taken eight years before explosion. Only the 17$\mathrm{M}_\odot$ model ended up in the allowed region in our mass range. However, the final temperature – or radius – is very sensitive to the details of the calculation such as the mixing length or overshoot parameters or metallicity, so we can not derive a concrete conclusion about the best mass range. For example in Figures 4.7 and 4.8 we show the evolutionary tracks for our lower and higher metallicity models. With lower metallicity the expansion of the stars are smaller than in Figure 4.6, and somewhere between 15 and 16$\mathrm{M}_\odot$ seems to be the matching model. Higher metallicity led to larger expansion, and the mass of the matching models increases.

The ZAMS masses of our matching models are rather heavier than the matching models in Eldridge and Maund (2016). This may be due to the different treatments of the CE evolution. In their `BPASS` code, they use the usual RLOF rate but limit it by $\dot{M} = 10^{-3}\mathrm{M}_\odot$ for the mass-loss rate during CE evolution (Eldridge et al., 2008), and terminate when both stars reside within their Roche lobes. Their choice for the upper limit value is due to numerical reasons, and not motivated physically. A CE phase is a highly dynamical process, and the usual mass-loss rates that were derived assuming nuclear time-scale processes do not describe the dynamical nature of CE evolution well. The lower mass-loss rate will lead to a longer time-scale for the CE phase, giving more time for the core to grow. Together with their different termination criterion, their method will always leave a larger remnant than ours, which may possibly explain

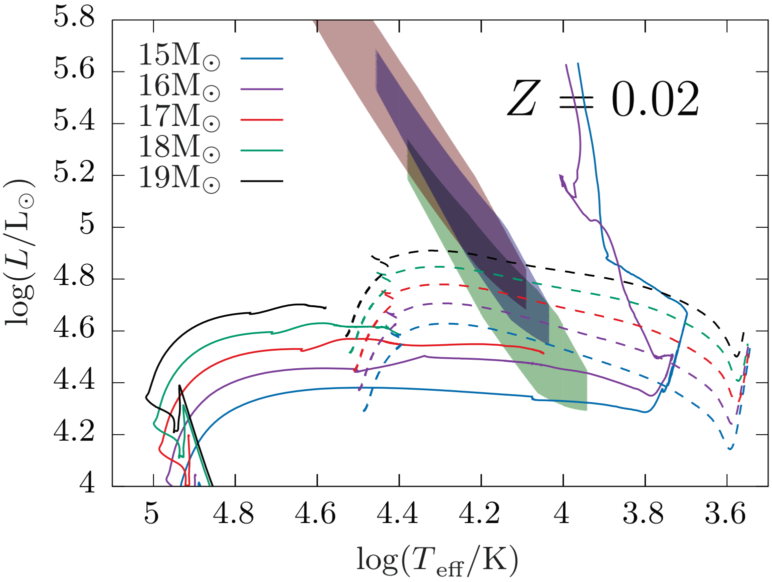

Figure 4.6: Evolutionary tracks of stars with a metallicity $Z = 0.02$ on the HR diagram. Dashed lines are for before the CE phase, and solid lines are for after the CE phase up to eight years before collapse. The shaded regions are taken from Figure 4.2.

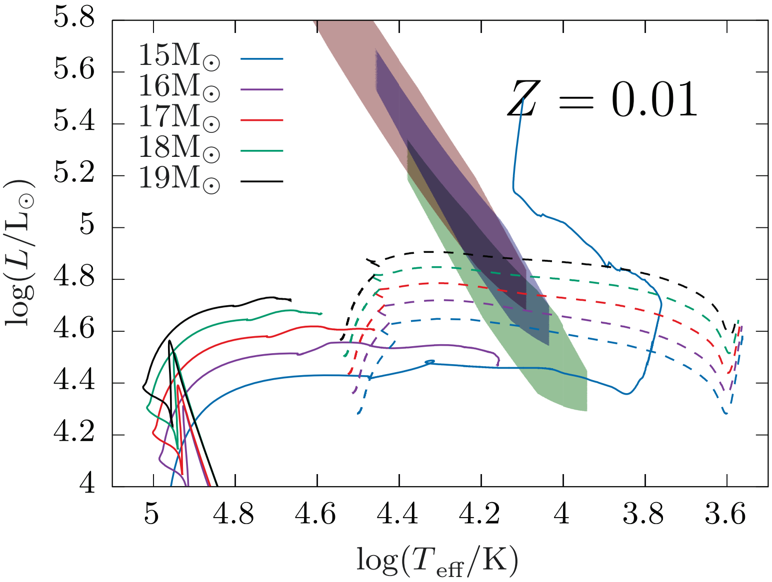

Figure 4.7: Same as Figure 4.6 but with a metallicity $Z = 0.01$.

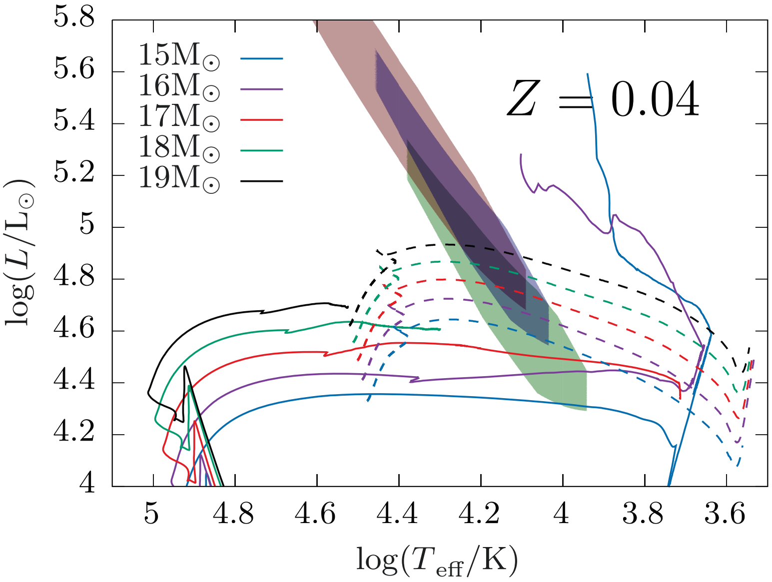

Figure 4.8: Same as Figure 4.6 but with a metallicity $Z = 0.04$.

the discrepancy of the results.

It should also be noticed that the ZAMS masses of our matching models are within the range estimated from the nebular phase oxygen lines. But because in the CE scenario we remove the envelope before the core grows to its full size, the final ejected oxygen may be smaller than the observed values.

Although we have a matching model, the final temperatures in the stellar evolution calculations are not so reliable, so we will not conclude which models are the best. On the other hand, the luminosity is almost constant in the final stages, which is strongly correlated with the core mass. From the lower limit of the luminosity of the allowed region, we can place a rough lower limit $\sim 2.5\mathrm{M}_\odot$ on the core mass of the progenitor.

4.4.3 Pre-CE Separation

Here we will discuss the upper limit to the initial orbital separation of the progenitor system in the context of the CE scenario. There are two pathways known so far to initiate a CE phase. The first is via unstable mass transfer. Once the primary star fills its Roche lobe, a part of the outer envelope of the star will be transferred to the secondary through the inner Lagrangian point. This is the usual Roche lobe overflow. If the mass transfer is unstable, the star will eventually overfill the second Lagrangian point (only the primary component). Then a part of the envelope material will start trickling away from the system. This flow will take away angular momentum, shrinking the orbit even more, leading to a CE phase. The onset of an unstable mass transfer is usually computed by comparing the volume of the star with the primary component of the volume enclosed within the equipotential surface passing through the second

Lagrangian point. The effective radius of this volume R_{L_2}can be approximated by

$$\frac{R_{\mathrm{L}_2}}{a} \approx \frac{0.49q^{2/3}+0.27q-0.12q^{4/3}}{0.6q^{2/3}+\ln(1+q^{1/3})}, \quad q \leqq 1 \tag{4.3}$$

$$\approx \frac{0.49q^{2/3}+0.15}{0.6q^{2/3}+\ln(1+q^{1/3})}, \quad q \geqq 1 \tag{4.4}$$

where a is the binary separation, $q \equiv m_1/m_2$ and m_1, m_2 are the primary and secondary masses (Eggleton, 2011). Thus the criterion for unstable mass transfer will be

$$R > R_{\mathrm{L}_2} \tag{4.5}$$

where R is the radius of the primary. The other path is via Darwin instability (Hut, 1980; Lai et al., 1993). This occurs when the tidal forces extract orbital angular momentum to spin up the stars, but there is not enough angular momentum left in the orbit to do so. The condition for this instability is

$$J_{\mathrm{spin}} > \frac{1}{3} J_{\mathrm{orb}} \tag{4.6}$$

where J_{spin} is the moment of inertia of the primary star and J_{orb} is the moment of inertia of the orbit. J_{orb} can be expressed as $J_{\mathrm{orb}} = \mu a^2$ where $\mu = m_1 m_2/(m_1+m_2)$ is the reduced mass.

In either of the cases, the CE phase will be initiated at the time when the primary star evolves to a red giant, and is rapidly expanding in size. Both the radius and moment of inertia of the star grow rapidly at this stage, and will eventually satisfy one of the criteria above, depending on the secondary mass. If m_2 is relatively large, J_{orb} will be large, so the system is unlikely to be Darwin unstable and thus enters the CE phase via unstable mass transfer. The maximum possible separation for unstable mass transfer to occur can be estimated by

$$a_{\mathrm{max,L}_2} \approx R_{\mathrm{max}} \frac{0.6q^{2/3}+\ln(1+q^{1/3})}{0.49q^{2/3}+0.15} \tag{4.7}$$

where R_{max} is the maximum radius achieved in single star evolution. If m_2 is relatively small, J_{orb} is small and the system will be Darwin unstable before the primary overflows the L_2 point. The maximum possible separation to be Darwin unstable $a_{\mathrm{max,DI}}$ can be estimated by

$$a_{\mathrm{max,DI}} \approx \sqrt{\frac{3J_{\mathrm{spin,max}}}{\mu}} \tag{4.8}$$

where $J_{\mathrm{spin,max}}$ is the maximum moment of inertia obtained in the single evolution models. In Figure 4.9 we show the maximum possible orbital separation as a function of secondary mass. We have used $J_{\mathrm{spin,max}}$ and R_{max} obtained from single star evolution calculations with metallicity $Z = 0.02$. The maximum separation is $\sim$ 1000–1800$\mathrm{R}_\odot$ throughout most of the mass range, which is determined by the L_2 overflow criterion. Larger separations would be possible only if the secondary mass was smaller than $\sim 4\mathrm{M}_\odot$.

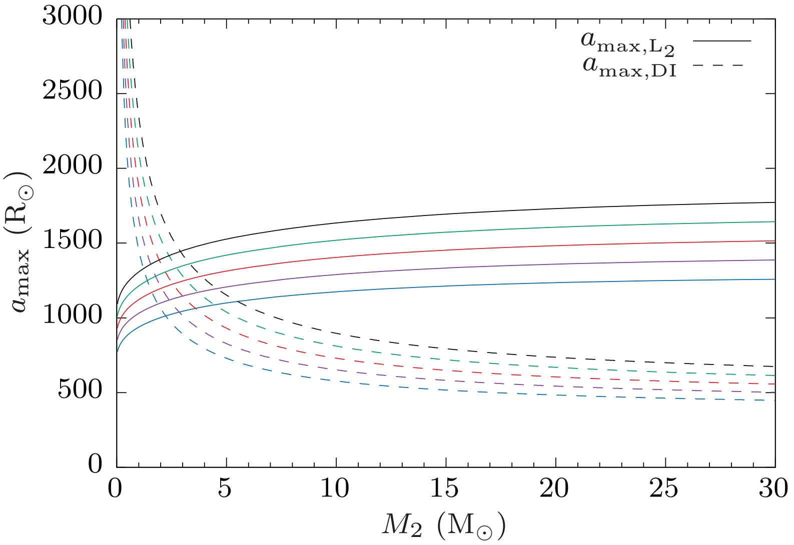

Figure 4.9: Maximum orbital separation as a function of the secondary mass M_2. Line colours express the primary mass, with the same colours as in Figure 4.6

4.4.4 CE Efficiency parameter

We will now constrain the $\alpha_{\rm CE}$ parameter in this system to discuss the ejectability of the envelope. In usual population synthesis calculations, $\alpha_{\rm CE}$ is given by hand, to calculate the final separation a_f. We will go the other way round, and use the constraints on a_f to calculate a lower limit to $\alpha_{\rm CE}$. Eq. 4.1 can be rewritten as

$$\begin{aligned}\alpha_{\rm CE} &= E_{\rm env}\left(-\frac{Gm_1m_2}{a_i}+\frac{Gm_{\rm cp}m_2}{a_f}\right)^{-1} \\ &\geq \frac{E_{\rm env}a_f}{Gm_2m_{\rm cp}} \qquad (4.9)\end{aligned}$$

The inequality can almost be regarded as an equality because the initial separation is usually much larger than the final separation, and thus the first term in the parenthesis can be ignored. We have a rough estimate on $m_{\rm cp}$ from the observed ejecta mass. Therefore the important values that determines $\alpha_{\rm CE}$ are $E_{\rm env}$ and a_f.

The binding energy of the envelope is usually estimated by

$$E_{\rm env} = -\int_{m_{\rm cp}}^{m_1}\left(-\frac{Gm}{r}+\epsilon\right)dm \qquad (4.10)$$

where m_1 is the total mass of the star and ϵ is the specific internal energy. But in order to take into account the relaxation of the core after the mass ejection, it should be calculated by comparing the total binding energies of the star before and after the CE event (Ge et al., 2010).

$$\begin{aligned}E_{\rm env} &= E_{{\rm bind},i} - E_{{\rm bind},f} \\ &= -\int_0^{m_{1,i}}\left(-\frac{Gm}{r}+\epsilon\right)dm + \int_0^{m_{1,f}}\left(-\frac{Gm}{r}+\epsilon\right)dm \qquad (4.11)\end{aligned}$$

Here the integration is taken over the whole star before (first term) and after (second term) the CE phase. For the model CE calculations in section 4.4.2, the values calculated by Eq. 4.10 overestimated the binding energy by $\sim 10\%$. We use the values calculated by Eq. 4.11 in our following discussions.

The final separation is quite uncertain. The closest possible separation is when the post-CE primary star (and of course the secondary) does not overfill its Roche lobe. Using the post-CE radius obtained in the model CE simulations, we can calculate the minimum possible separation by assuming that one of the binary components exactly fills its Roche lobe. This can be expressed as

$$a_{f,\mathrm{min}} = \max\left(\frac{R_f}{f(q)}, \frac{R_2}{f(q^{-1})}\right) \tag{4.12}$$

where R_f is the post-CE radius of the primary star, R_2 is the secondary radius, and $q = m_{\mathrm{cp}}/m_2$. $f(q)$ is a function fitted to the approximate Roche lobe radius (Eggleton, 1983).

$$f(q) \equiv \frac{0.49q^{2/3}}{0.6q^{2/3} + \log(1 + q^{1/3})} \tag{4.13}$$

We can obtain the lower limit to α_{CE} as a function of the secondary mass by plugging in E_{env} and $a_{f,\mathrm{min}}$ into Eq. 4.9. This is shown in the lower panel of Figure 4.10. We have used the ZAMS radius for R_2. The minimum value in our calculations was ~ 0.5, which means that at least half of the orbital energy should be used to eject the envelope. The limit increases as the secondary mass decreases because of the decrease of the energy reservoir in the orbit. If the secondary was $\lesssim 6\mathrm{M}_\odot$, the lower limit exceeds unity, which suggests the presence of an extra energy source to eject the envelope. All models were limited by the secondary star radius filling its Roche lobe. If we consider a compact object as the companion, the final separation will be limited by the post-CE radius of the primary, and $\alpha_{\mathrm{CE,min}}$ will be smaller by a factor of ~ 5.

4.4.5 Deficits of the CE scenario

So far the CE scenario seems successful, since the system can eject the envelope with an efficiency smaller than unity $\alpha_{\mathrm{CE}} < 1$ if the companion was larger than $\sim 6\mathrm{M}_\odot$. However, this scenario has a difficulty in explaining the post-CE evolution of the binary. Since the final radius of the progenitor should be larger than $\sim 30\mathrm{R}_\odot$ (see Figure 4.2 and 4.3), which is much larger than the values of a_f calculated above, it is almost impossible to avoid a second CE phase. The outcome of a CE phase with a naked helium star is not known. But if the binary can successfully eject the envelope again[3], it will surely shrink the orbit even more. The primary will not be able to re-expand to $\sim 30\mathrm{R}_\odot$ this way. Therefore the second CE phase should have failed and the secondary star will have been engulfed by the primary before SN explosion. If the secondary was a main sequence star, there will be a substantial amount of fresh hydrogen injected to the core of the primary. This can significantly alter the appearance of the progenitor, taking it away from the allowed region and also may change the spectral type of the

---

[3] This may lead to the ejection of the whole helium envelope, which may change the spectral type of SN to type Ic.

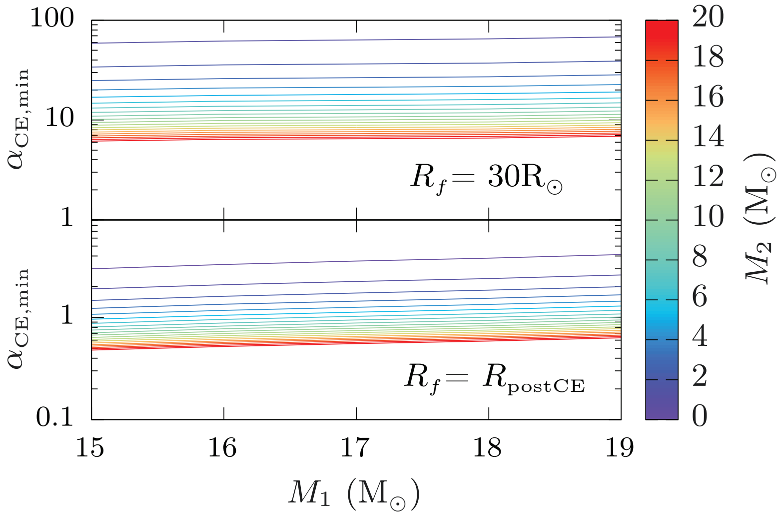

Figure 4.10: Lower limits on the $\alpha_{\rm CE}$ parameter based on the assumption that the secondary never interacted with the primary again (upper panel), or the secondary has already been lost (lower panel).

SN. The mass of the secondary should also be very small in order to keep the ejecta mass smaller than $\lesssim 2M_\odot$. But the first CE phase will not have succeeded in the first place if the mass was so small, unless the $\alpha_{\rm CE}$ parameter is considerably large. Therefore the secondary should avoid the second CE phase or be completely lost before SN. In order to avoid the second CE phase, the post-CE separation should be large enough so that the primary never interacts with the secondary again. In the upper panel of Figure 4.10, we show the minimum $\alpha_{\rm CE}$ required to have a large enough post-CE separation so that the Roche lobe radius for the primary becomes $30R_\odot$. The required value for $\alpha_{\rm CE}$ becomes $\gtrsim 6$ even for the largest possible secondary masses, which is very unlikely even with the consideration of other energy sources such as recombination energy. The primary may have lost its companion because of a third body encounter, but this may also be difficult considering the very tight post-CE orbit. Unless we resolve this problem, the CE scenario should be refuted.

To sum up, the CE scenario is able to reproduce the observed ejecta mass, pre- and post-SN photometry. However, the success of this model requires a significant orbital shrinkage, which will suffer a second CE phase before SN. The second CE phase will ruin the advantages of this model by increasing the ejecta mass and altering the pre-SN photometry. The ejected oxygen mass may also be smaller than the observed amount. Therefore we conclude here that the CE scenario is not suitable to explain the formation of the progenitor of iPTF13bvn.

4.5 Stable Mass Transfer to a Black Hole?

From the previous discussion, the CE scenario seems not to be suitable as the formation scenario of the progenitor of iPTF13bvn. Here we will return to the stable mass transfer scenario again. The reason that we have excluded this scenario in the first place was

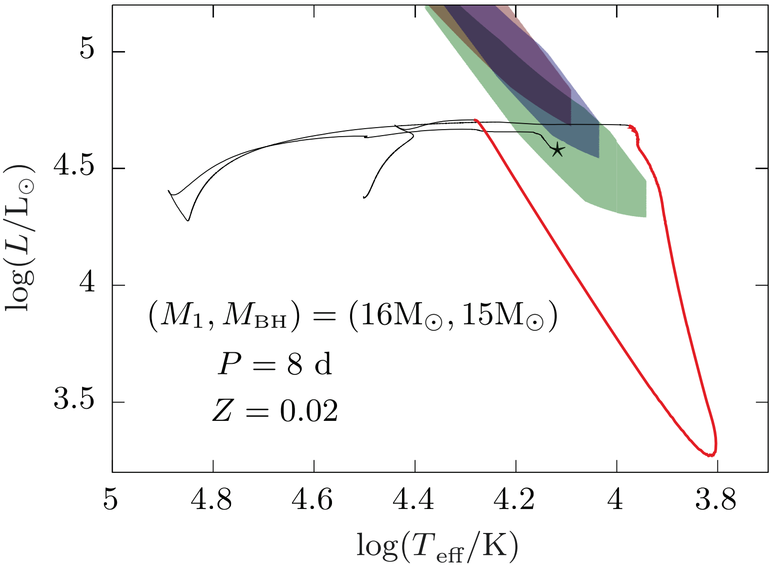

Figure 4.11: Evolutionary track of a $16{\rm M}_\odot$ star with a $15{\rm M}_\odot$ BH companion. The star symbol marks the position eight years before SN. The red part of the curve indicates the mass transfer phase.

the non-detection of a companion. A sufficiently large companion is needed to enable stable mass transfer, and the star will also grow due to the accretion of transferred mass. However, this is only problematic if the companion is on the main sequence. The situation will be completely different if the secondary was a BH, since we can not observe a BH whatever the mass is unless it has an accretion disc around it.

Here we will demonstrate that a binary with a BH component can evolve up to SN without conflicting with any of the observational constraints. We used the binary module in `MESA`, and simulated the evolution of a $16{\rm M}_\odot$ star with a $15{\rm M}_\odot$ BH companion in an 8 day circular orbit. The metallicity is assumed to be $Z = 0.02$. The mass transfer rate was calculated according to the prescription by Kolb and Ritter (1990) and the mass retention on the BH was limited by the Eddington limit. The evolutionary track of the primary is shown in Figure 4.11, overplotted on the allowed region again. This system undergoes a case B mass tranfer, losing most of its hydrogen envelope during this phase. When the remaining hydrogen becomes sufficiently small, the star contracts rapidly and detaches from the BH. Most of the remaining hydrogen is burned in the H burning shell and only $\lesssim 0.04{\rm M}_\odot$ is left by the time of SN. This small amount of hydrogen may be the origin of the weak Hα lines in the early spectra (Fremling et al., 2016). The endpoint of the evolution rests in the allowed region, which makes this system a good candidate for the progenitor of iPTF13bvn. There is almost no change in the mass of the BH, only growing by $\sim 0.017{\rm M}_\odot$, meaning that most of the mass has been lost from the system. The overall evolution of the primary does not change largely even if we increase the mass of the BH up to $\sim 100{\rm M}_\odot$.

This demonstration is only an example of the evolutionary path, and there is a wider range of possible initial parameters. The primary mass should be in the range $\sim$ 14–17${\rm M}_\odot$ to create a He core in the mass range of the observed ejecta mass, create the right amount of oxygen, and have a final luminosity consistent with the pre-SN fluxes. On the other hand, there is no strong constraint on the BH mass because it does not largely affect the evolution of the primary. The only constraint is the lower limit which is roughly ~ 0.8 times the primary mass, to enable stable mass transfer. The initial period range should be roughly 4–20 days for the mass transfer to initiate in case B, although we can not rule out case A mass transferring models[4].

The largest uncertainty in this model is the origin of the BH. For example, the BH could have been an extremely massive star ($\gtrsim 30\mathrm{M}_\odot$), in a relatively wide orbit with a $\sim$ 14–17$\mathrm{M}_\odot$ companion. As the more massive star evolves, it develops a $\gtrsim 15\mathrm{M}_\odot$ He core, and expands to $\sim 2000\mathrm{R}_\odot$. This may initiate a CE episode, and because the core mass is large, the post-CE separation is at moderate distances $\sim 50\mathrm{R}_\odot$. At some point the massive He core will collapse to a BH and then the system will follow an evolution similar to that in the above demonstration. There is no strong support to this scenario, and deeper investigations should be carried out to check the relevance of this model. We will leave this to future works.

Since the ejecta mass is much smaller than the expected BH mass, the system will still be bound after the SN explosion, and the outcome of this model will be a BH-NS binary in a relatively wide orbit ($\sim 100\mathrm{R}_\odot$). Thus we expect that we will not find a companion star in any future observations. The orbital separation is too wide to cause a BH-NS merger in a realistic time-scale, leaving no hope for gravitational wave detection. It will be extremely difficult to confirm our scenario, but the non-detection of a companion star in the next few years can strengthen our hypothesis.

4.6 Conclusions

The observational constraints on the progenitor of iPTF13bvn have been revisited. We evaluated the possible position on the HR diagram and constrained the photospheric radius of the progenitor. The radius should have been in the range $\sim$20–70$\mathrm{R}_\odot$. All studies now agree that the progenitor should have been in a binary system, and expect to be able to detect a companion star in the future. We have derived the upper limit on the remaining secondary star based on the latest observational data of the SN and obtained similar results to previous works ($\sim 20\mathrm{M}_\odot$). But this is probably much smaller if we consider the effects of SN ejecta-companion interaction as discussed in Hirai and Yamada (2015).

We have also reassessed the relevance of the formation scenario of the progenitor via a CE phase. We performed stellar evolution calculations to mimick the post-CE evolutionary tracks just for the donor, and found a model that matches the observational constraints. However, if we consider the energy budget in the CE phase, an extremely large companion or a very high CE efficiency ($\gtrsim 6$) is required to avoid a second CE phase, which is unrealistic. Therefore we conclude that the CE scenario is unlikely to be the formation scenario for the progenitor of iPTF13bvn.

As an alternative model, we considered the evolution of a binary with a BH component. Stable mass transfer from the primary star to a BH can strip off most of the hydrogen envelope up to the edge of the He core. We have demonstrated one example evolutionary track that satisfies all observational constraints. We roughly estimate

---

[4] The mass range discussed here are quite sensitive to the parameters and assumptions applied to the stellar evolution code such as the mixing length, overshoot parameters or convection criteria.

that the mass of the primary should be in the range $\sim$ 14–17$M_\odot$ and the BH should be heavier than 0.8 times the primary mass. The orbital period should be ∼4–20 days.

There is still no quantitative support on the origin of the BH. The system may have experienced a CE phase of a much larger star, but it remains a matter of speculation. We will leave the investigation to future works.

It is almost impossible to confirm our scenario by future observations because the expected outcome is a wide BH-NS binary. However, if there is no detection of a companion star in the coming few years, we believe it will be a strong support of our model.

"Why does the eye see a thing more clearly in dreams than the imagination when awake?"
Leonardo da Vinci (1452–1519)

5

Conclusion and Future Prospects

5.1 Conclusion of this Thesis

I have explored many aspects of supernova in massive binaries using various kinds of numerical simulations. From two dimensional hydrodynamical simulations of supernova ejecta hitting a red supergiant, we have found out that the largest possible mass that can be stripped off a companion in a binary is $\sim$ 25% of its mass. This may be large enough in some cases so as to disrupt the binaries that would have survived without considering ejecta-companion interaction. The unbound mass was roughly proportional to $M_{\rm ub} \propto a^{-4.2}$, which contradicts with the analytical model by Wheeler et al. (1975). We also revealed that the unbound mass is strongly correlated to the impact density, and proposed a simple model that may explain the physics of the mass stripping process.

We have to be careful with this result because the binary system that we simulated in Chapter 2 was highly unlikely to exist in nature. Most exploding stars will have a less evolved star (most likely on the main sequence) as a companion unless we consider very exotic situations. In Chapter 3 we carried out binary evolution simulations to construct a realistic binary system that may represent the progenitor of a specific supernova iPTF13bvn. Then I performed a similar simulation as the previous ejecta-companion interaction simulation on the companion star. Due to the wide separation because of the stable case A mass transfer and the compact nature of the main sequence companion, the impact of ejecta-companion interaction was almost negligible. Although there were noticable changes in the appearance of the companion, the effect was not large enough to change course of the further evolution.

The possible reddening that we have predicted in Chapter 3 was not observed in the latest observations of iPTF13bvn. This observation together with our previous simulation revealed that the original binary evolution scenario was wrong and we need an alternative scenario. In order to construct a model consistent with all observational constraints, I reexamined all the analyses in previous works. Then I inspected the common envelope scenario carefully, finding out that it is almost impossible to explain the formation of the progenitor. I also suggest an alternative scenario involving an X-ray binary-like evolution of a binary with a massive black hole component. Future observations may be able to distinguish between existing models and my new model.

5.2 Towards a more Systematic Study

So far we have only investigated the upper limit, and a specific case for the supernova iPTF13bvn of ejecta-companion interaction. It is already evident from these works that the details of ejecta-companion interaction strongly depend on the structure of the companion star. Therefore, in order to see more general effects of ejecta-companion interaction on populations of binaries, we need to carry out a systematic study. Especially the stripped mass, kick velocity and maximum expansion radius should be known along with their dependences on binary parameters and structure of the companion. As we have seen in Chapter 2, the stripped mass and kick velocities does not agree so well with the analytical estimates by Wheeler et al. (1975). This may be because the mass stripping process is not by momentum transfer like in Wheeler et al. (1975) but rather mass ablation due to shock heating. Thus we need to carry out numerical simulations of the ejecta-companion interaction process with many different initial conditions.

The construction of many initial conditions would have been a painstaking task had it been a few years ago. Now it has become a whole lot easier to carry out binary evolution calculations by using the public stellar evolution code `MESA` (Paxton et al., 2011, 2013, 2015). It is now possible to simulate binary evolution up to core-collapse of the primary within a few hours. As for hydrodynamical simulations, the self-gravity part has been the bottleneck for the computational time. Without speeding up the self-gravity part it is impossible to carry out a systematic study of ejecta-companion interaction considering that our previous simulations took a few weeks per model. For this reason we have constructed a new method to dramatically speed up self-gravitational calculations without exacerbating the numerical errors. The details are explained in the Appendix A. By making use of our new method, the computational time of self-gravitational hydrodynamical simulations can be shortened by orders of magnitude. Now that we have prepared the necessary tools, we can proceed on to systematically study ejecta-companion interaction and make it applicable to population synthesis studies.

If we can accomplish this task, we may be able to better understand the "standard" scenario for compact binary formation. It will also become necessary to understand the long sought common envelope process too. I believe that our new method will enable hydrodynamical simulations of common envelope phases, and together with our ejecta-companion interaction simulations, we will be able to comprehensively understand the whole process towards compact binary formation.

Appendices

"As in nature, all is ebb and tide, all is wave motion, so it seems that in all branches of industry, alternating currents - electric wave motion - will have the sway."
Nikola Tesla (1856–1943)

A
Hyperbolic Self-Gravity Solver

A.1 Introduction

Recent advances in theoretical astrophysics have mostly been led by the rapid progress in supercomputing, of the computers themselves and the numerical techniques. In particular, hydrodynamical simulations coupled with gravity have proved to be a powerful tool to reveal the dynamics of many astrophysical and cosmological phenomena such as supernovae, star formation, relativistic jets, accretion discs, formation of large scale structure etc (Kuiper et al., 2010; Nagakura, 2013; Takahashi et al., 2014; Hosokawa et al., 2015; Tomida et al., 2015; Illenseer and Duschl, 2015; Hirano et al., 2015; Federrath, 2016). Most simulations deal with simplified models, assuming some symmetry and solving equations with reduced dimensions. In some fields, however, there are growing rationale that multidimensional effects can play a key role (Saijo and Kojima, 2008; Couch, 2013), and some phenomena are essentially multidimensional (Sato et al., 2015; Ohlmann et al., 2016a), meaning that numerical simulations also have to be carried out with full dimensionality. This itself can dramatically increase the numerical cost while at the same time, there are some studies where small scale effects can alter the global behaviour (Sawai and Yamada, 2016). In such cases it is necessary to resolve fine structures, making the calculation even more costly. Such computationally expensive calculations have become possible by making full use of state-of-the-art supercomputers, with the aid of a combination of efficient numerical schemes and parallelization technologies. However, computational resources for these large scale simulations are still limited, and it is often difficult to carry out systematic studies.

In astrophysical hydrodynamical simulations, it is usually not the hydrodynamics part that dominates the computational time. Instead, what prevents us from extending calculations to higher dimensions and higher resolutions, is the additional physics such as radiative transfer, nuclear reactions, neutrino transport, self-gravity etc. In order to carry out systematic studies in multi-dimensions, it is mandatory to construct rapid methods to treat these additional features. These additional effects are included by solving the governing equations of that feature and coupling it to the hydrodynamic Euler equations, or by applying approximated models based on feasible assumptions. For the case of self-gravity, the additional basic equation is the Poisson equation:

$$\Delta\phi = 4\pi G\rho \tag{A.1}$$

where Δ is the Laplace operator, ϕ the Newtonian gravitational potential, G the gravitational constant and ρ the mass density. This equation is an elliptic type partial differential equation (PDE) which can only be solved via direct matrix inversions or iterative methods or fast Fourier transform (Hestenes and Stiefel, 1952; Young, 1954; Fedorenko, 1962; Sköllermo, 1975; Black and Bodenheimer, 1975; Robert, 1982; Krebs and Hillebrandt, 1983; van der Vorst, 1992; Müller and Steinmetz, 1995; Huang and Greengard, 1999; Matsumoto and Hanawa, 2003; Ricker, 2008; Couch et al., 2013). Despite the efforts made in the past few decades to construct rapid Poisson solvers (Hestenes and Stiefel, 1952; Young, 1954; Fedorenko, 1962; Sköllermo, 1975; Black and Bodenheimer, 1975; Robert, 1982; Krebs and Hillebrandt, 1983; van der Vorst, 1992; Müller and Steinmetz, 1995; Huang and Greengard, 1999; Matsumoto and Hanawa, 2003; Ricker, 2008; Couch et al., 2013), it still remains the pain in the neck for many astrophysical hydrodynamic simulations. It becomes most problematic in multidimensional simulations with Eulerian schemes, and is sometimes approximated by monopoles even though the hydrodynamics are multidimensional (Hanke et al., 2013; Takahashi et al., 2014; Couch et al., 2015; Sawai and Yamada, 2016). The problem stems from the mathematical character of the equation itself, where the value on each cell depends on information from every other cell. This makes it extremely inefficient for parallelization, due to the huge amount of communication among memories which slows down the whole calculation. The situation gets increasingly worse as the size of the simulation increases.

On the other hand, the equation for general relativity is the Einstein field equations. When formulated as an initial value problem, the Einstein equations indicate that the evolutions of gravitational fields are governed by a hyperbolic equation as long as it initially satisfies the Hamiltonian and momentum constraints (Misner et al., 1973; Alcubierre, 2008). This implies that gravity is essentially hyperbolic, and its evolution only depends on its local neighbourhood. In this paper we propose a new method to circumvent the problems in Newtonian gravity, by incorporating the hyperbolicity of general relativity into the Poisson equation. Our new method can significantly reduce the computational cost of self-gravitational calculations.

Instead of the Poisson equation (A.1), we choose to solve an inhomogeneous wave equation

$$\left(-\frac{1}{c_g^2}\frac{\partial^2}{\partial t^2} + \Delta\right)\phi = 4\pi G\rho \tag{A.2}$$

where we define c_g as the propagation speed of gravitation. This equation was motivated from the essentially hyperbolic nature of gravity in general relativity. It roughly corresponds to the weak field limit of the Einstein equations. The Newtonian limit is achieved by assuming an infinite c_g, which is the cause of the difficulties, but here we just assume it is large, and not take the limit. Similar to electromagnetic fields, this equation will introduce causality, and the solution will therefore be somewhat like a retarded potential (Jackson, 1999). In this way, Eq.(A.2) can easily be parallelized since it is a hyperbolic PDE and only requires communication of memories between neighbouring cells. Our approach seems similar to the method introduced by Black and Bodenheimer (1975); Krebs and Hillebrandt (1983) where they convert the Poisson equation into a parabolic equation. However, the nature of a parabolic PDE and hyperbolic PDE is totally different, thus introducing different advantages and disadvantages to the method.

One important parameter that needs to be set is the value for the gravitation propagation speed c_g. A large enough c_g will give us an equivalent solution to the Poisson equation, which is desired from the Newtonian point of view, but the computational time will be large due to the strict Courant-Friedrichs-Lewy condition. If we take a lower value for c_g, the computation will speed up, but the solution will deviate from that of the Poisson equation because the time derivative becomes comparable with the other terms. Thus the value for c_g should be chosen carefully for each simulation according to the required accuracy and the computational resources available. Yet we show later in this section that c_g can be taken relatively small without affecting the solution, and can dramatically improve the numerical efficiency of self-gravity.

A.2 Numerical Procedure

We performed several calculations to demonstrate the efficiency of our new method. Firstly, we checked how well our new method maintains the equilibrium of a polytrope sphere in two-dimensions (2D) and three-dimensions (3D). Secondly, we simulate the head-on collision of equal mass polytropes in 2D. We use a hydrodynamical code which solves the ideal magnetohydrodynamic equations with the finite volume method, using the HLLD-type approximate Riemann solver (Miyoshi and Kusano, 2005). Since magnetic fields are ignored in our calculations, it is equivalent to using the HLLC scheme. Cylindrical coordinates are used for 2D simulations assuming axisymmetry whereas 3D simulations are carried out in Cartesian coordinates. An ideal gas equation of state with an adiabatic index $\gamma = 5/3$ is used for all calculations. An outgoing boundary condition is used for the outer boundaries.

For self-gravity we solve two different equations; Eq.(A.2) and the Poisson equation, for comparison. An iterative method called the MICCG method (Hestenes and Stiefel, 1952; Robert, 1982) is used to solve the Poisson equation, with boundary values given by multipole expansion. Eq.(A.2) is solved by simple discretization with the aid of the cartoon mesh method (Alcubierre et al., 2001) to simplify the cylindrical geometry in the 2D tests. Robin boundary conditions are applied for the outer boundary (Gustafson, 1998). As for the value of c_g, we normalize it by the characteristic velocity

$$c_g = k_g(c_s + |\boldsymbol{v}|) \tag{A.3}$$

where c_s is the sound speed, $\boldsymbol{v}$ is velocity, and k_g is an arbitrary parameter that should be larger than unity. The timestep condition for the wave equation will become k_g times stricter than for the hydrodynamical part. Although the gravity and hydrodynamical equations should essentially be solved simultaneously, here we choose to solve them on separate timelines. In this way, the wave equation will be solved k_g times during one hydrodynamical timestep, and will reduce the computational cost. Owing to the fact that the wave equation only depends on the density distribution, and since the density distribution does not significantly change during one timestep, this will give sufficient accuracy. It should also be noted that the Courant number used to decide the timesteps for the gravity and hydrodynamical parts do not necessarily need to coincide. If we take larger Courant numbers for the gravity part than the hydrodynamics, the computational cost can be reduced even more. In this paper we simply take both Courant numbers to be 0.3, but the results did not change even for larger Courant numbers such as 0.9.

For the first test calculation, we place a polytrope sphere with a polytropic index $N = 3$ at the centre of the 2D cylindrical grid. The sphere has a mass and radius of $(M, R) = (8M_\odot, 3.75R_\odot)$. The computational domain is taken approximately twice the stellar radius in both radial and longitudinal directions, and divided into $(N_r \times N_z) = (210 \times 280)$ cells. A dilute atmosphere is placed around the star, with a mass negligible compared to the stellar mass. We simply wait for several dynamical times to see whether the star stays in mechanical equilibrium. Two simulations are carried out for comparison, one by solving the Poisson equation throughout (P model), and one by solving Eq.(A.2) with $k_g = 5$ (H model). The initial condition is given by solving the Poisson equation in both cases.

As a demonstration of 3D capabilities, we place the same polytrope sphere at the origin of a three-dimensional Cartesian grid. Plane symmetry is assumed for all three directions, which will leave us with an eighth of the star. The computational domain is taken ~ 1.5 times the stellar radius in each direction, and divided into $(N_x \times N_y \times N_z = 140^3)$ cells. The resolution of the grid is equivalent to the first test calculation. To make it a 3D specific problem, we add random density perturbations with an amplitude of $< 1\%$. This will induce some stellar oscillation modes but overall, the star should stay in a stable state. Since we use a relatively large number of cells, it is extremely difficult to solve the Poisson equation. In fact, it was impossible on our workstation to solve in a realistic timescale, so we interpolate from the exact solution as an initial condition for the gravitational potential instead.

To test a more dynamically evolving case, we place another identical polytrope sphere 4.2×10^{11} cm away from the centre of the region in the longitudinal direction on a 2D cylindrical grid. We assume equatorial symmetry, which mirrors the star on the opposite side. Since we do not give any orbital motions, the two stars will simply fall into each other by the gravitational force of each other, causing a head-on collision. Like in the first test, we carry out the simulation with the two different types of self-gravity for comparison, and call them the P and H models.

A.3 Results

Fig.A.1 shows the density distribution of the initial condition on the left side, and ~ 5 dynamical times later on the right side for the H model. Both panels show almost identical distributions, indicating that hydrostatic equilibrium of the star is well resolved with this grid. The degree of equilibrium can be checked in Fig.A.2, which shows the evolution of central density and the degree of satisfaction of the

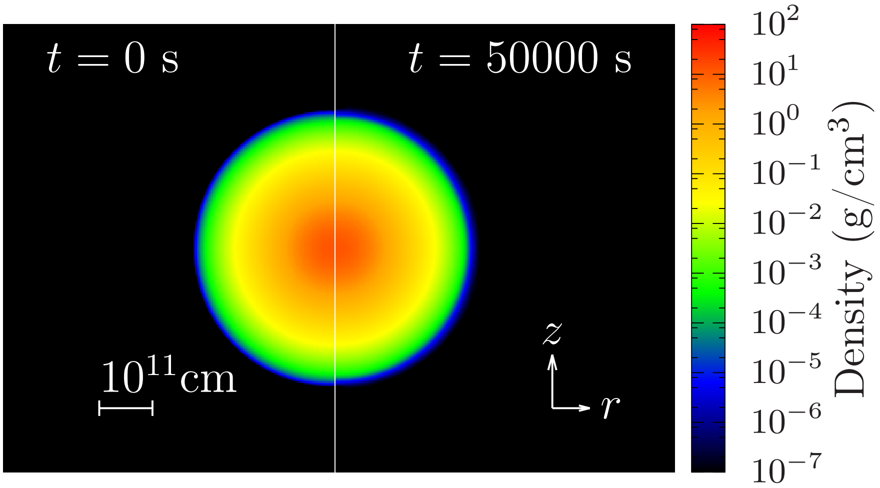

Figure A.1: Density plot for the stationary star test. Left panel: initial condition, Right panel: 5×10^4 s later.

Virial theorem (VC) defined as

$$VC = \frac{W + 3(\gamma - 1)U}{|W|} \tag{A.4}$$

where U and W are the internal and gravitational energies integrated over the bound zones (zones with negative total energy). The initial condition for the polytrope sphere is given simply by interpolation from the exact solution. So as soon as the simulation starts, the star tries to adjust to its equilibrium condition on the discretized grid. This leads to a slow decrease in the central density, but the decline rate is extremely slow and it is safe to assume that the star is resolved properly on this grid, with both methods. There is a roughly dynamical timescale oscillation in the value of VC in both P and H models. But the amplitude is very small and does not grow, which indicates that the star satisfies the virial equilibrium condition throughout the simulation. The computational time was ~ 5 times shorter for the H model than the P model.

Similar results were obtained for the 3D star case, depicted in Fig.A.3. The black lines show the non-perturbed star case, which is simply an extention of the H model calculation to 3D and in different coordinates. It is remarkable that the star remains in virial equilibrium even in 3D, at a degree of $\sim 0.05\%$. The red lines show the evolution of the same star with $\sim 1\%$ random density perturbations. There is no notable difference in the evolution of the central density, only declining $\sim 2\%$ after ~ 5 dynamical times. The fluctuation around virial equilibrium is larger than the non-perturbed model, but does not grow in time, staying in a stably oscillating state at the same timescale as the 2D test.

Fig.A.4 shows the density distribution of the head-on collision simulations with the two different methods at two different times. The upper halves of each panel are results for the P model, and the lower halves are for the H model. It can be seen that the two stars fall into each other, causing a head-on collision, forming a shock at the interface. The stars then merge to become a single star, but a part of the envelope is blown away by the shock. Although the evolution is delayed by $\sim 15\%$ in the H model, the overall behaviour of the dynamics between the two models are quite similar. This

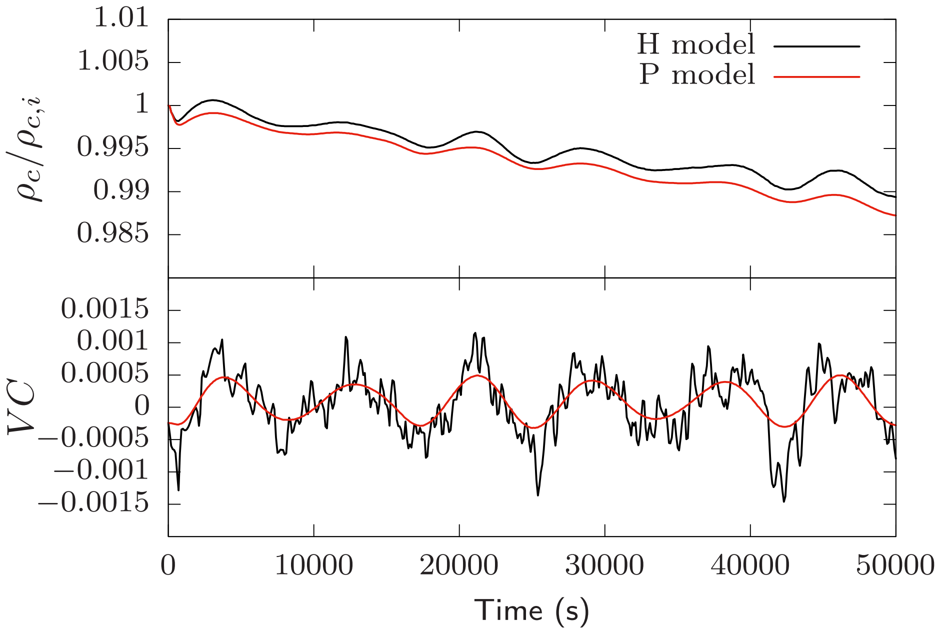

Figure A.2: Evolution of the central density (Upper panel) and degree of satisfaction of Virial theorem (VC, lower panel) in the 2D static star simulations. Density is normalized by the initial central density, and VC is defined in Eq.A.4. Red lines: H model, Black lines: P model.

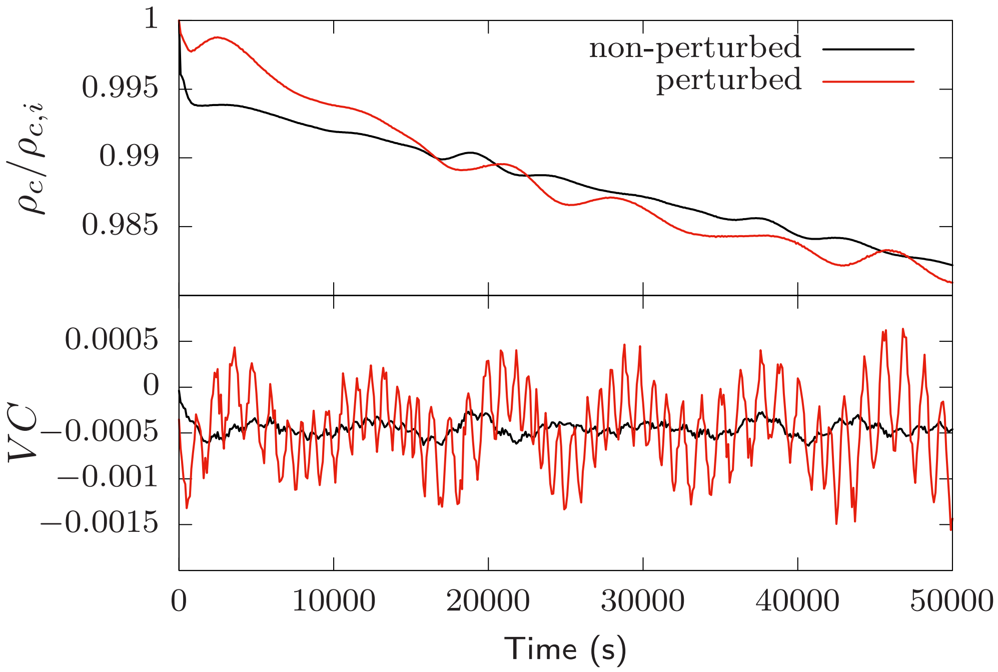

Figure A.3: Evolution of the central density (Upper panel) and degree of satisfaction of Virial theorem (VC, lower panel) in the 3D simulations. Density is normalized by the initial central density, and VC is defined in Eq.A.4. Red lines: perturbed model, Black lines: non-perturbed model.

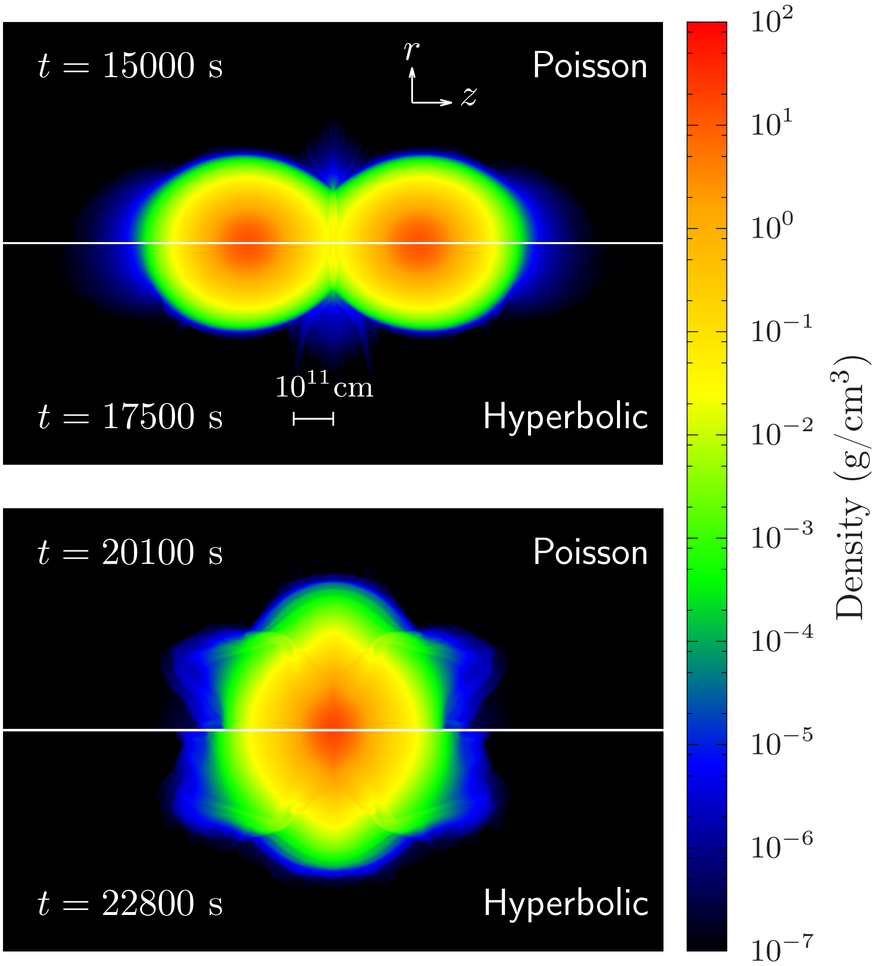

Figure A.4: Snapshots of the density distribution for the head-on collision simulations. Upper halves of each panel; P model, lower halves; H model. The time elapsed are written on the left corners, and white line at the centre shows the coordinate axis.

already indicates that our new method can at least be used for qualitative studies. Moreover, the total computational time of the H model was ~ 30 times shorter than the P model, implying that our new method is most efficient for dynamically evolving gravitational fields. This is because when the gravitational potential is moving, the MICCG method needs more iterations than stationary situations to converge to its solution.

A.4 Discussions

Here we are not interested in the physics of the test calculations carried out, but in the difference between the two methods. Our aim was to produce an efficient method to treat self-gravity, that reproduces the same results as with previous methods which solve the Poisson equation. In this section we quantitatively evaluate the differences between the solution obtained in our simulations by the new method and the solution of the Poisson equation. We focus on the head-on collision simulation, since it had the largest difference and because we are more interested in applying our new method to

Table A.1: Model Descriptions

Model	$r_{\rm max}{}^1$ (cm)	$z_{\rm max}{}^1$ (cm)	$N_r{}^2$	$N_z{}^2$	b.c.[3]	k_g
aD05	6.3×10^{11}	8.4×10^{11}	210	280	Dirichlet	5
aR05	6.3×10^{11}	8.4×10^{11}	210	280	Robin	5
bR05	1.8×10^{12}	2.4×10^{12}	600	800	Robin	5
cR05	3.6×10^{12}	4.8×10^{12}	1200	1600	Robin	5
aR20	6.3×10^{11}	8.4×10^{11}	210	280	Robin	20
bR20	1.8×10^{12}	2.4×10^{12}	600	800	Robin	20
cR20	3.6×10^{12}	4.8×10^{12}	1200	1600	Robin	20

[1] Size of the computational domain in each direction.

[2] Number of zones in each direction.

[3] Boundary conditions. Dirichlet boundaries are applied by multipole expansion.

dynamically evolving systems.

One of the main causes of the difference between the two methods is the boundary condition. For the Poisson solver, we use Dirichlet boundary conditions with values given by multipole expansion, which obtains the exact solution for the Poisson equation for the given density distribution. On the other hand, the boundary condition used in the new method is a Robin boundary, which is equivalent to assuming monopole gravity. Since the higher order terms are non-negligible in the current situation, this boundary condition is inappropriate.

We carry out several additional simulations to quantify the effects of the boundary condition, and seek how to improve the results. The parameters used in our extra simulations are listed in Table A.1. Eq.(A.2) is used for self-gravity in all models. Model aR05 corresponds to the H model explained above. Three different modifications are made to single out the effects of the boundary condition. In the first approach, we apply the Dirichlet boundary condition by multipole expansion as in the P model (aD05). This will directly remove the boundary error, although the calculation becomes heavy and is inappropriate for practical use. Our second approach is to widen the computational domain without changing the resolution (aR05-cR05), which will weaken the multipole effects at the boundary. Finally, we also change the value of k_g to a larger value (aR20-cR20), which should bring our equation closer to the Poisson equation.

We define the relative "error" as

$$\delta\tilde{\phi}(\boldsymbol{r}) := \frac{\phi_{\rm H}(\boldsymbol{r}) - \phi_{\rm P}(\boldsymbol{r})}{\phi_{\rm P}(\boldsymbol{r})} \tag{A.5}$$

$\phi_{\rm H}$ is the gravitational potential calculated with our new method, and $\phi_{\rm P}$ is the solution for the Poisson equation at the given density distribution. Hence the average relative error is

$$\left\langle \delta\tilde{\phi} \right\rangle = \left(\frac{\int_{\rm V} (\delta\tilde{\phi})^2 dV}{\int_{\rm V} dV} \right)^{\frac{1}{2}} \tag{A.6}$$

where the integrals are taken over the entire region.

Fig.A.5 shows the time evolution of the average relative error in each model. All lines fluctuate around a certain value, indicating that the error does not pile up in most cases. The maximum error was $\sim 10\%$ even in our "worst" model (aR05, aR20). This is the cause of the $\sim 15\%$ delay in the collision time. The error was reduced most when the Dirichlet boundary condition was applied (aD05; red dashed line), where the error does not exceed $\sim 0.1\%$ throughout the calculation, and the delay time also became negligible. This is a surprisingly good agreement, and proves that the differences of our method to previous ones only arise from the boundaries. Our hypothesis is further verified by the other simulations with larger computational regions. The relative error is roughly inverse proportional to the number of zones, from $\sim 10\%$ in 5.88×10^4 zones to $\sim 0.003\%$ in 1.92×10^6 zones. The wider the region, the smaller the errors. This is because the relative contribution of the boundary to the computational domain is smaller for wider regions, and also the multipole effects are weakened at the boundary. Another fact to be noted is that the error does not strongly depend on the value of k_g used in the simulation. The average error simply fluctuates around a value determined only by the domain size, at a frequency proportional to $\sim c_g/L$ where L is the size of the domain. In fact, even if we take $k_g = 2$, the overall behaviour is indistinguishable with other models as long as we take a large enough region. At the most turbulent and messy situations like after the collision ($t \gtrsim 20000$ s), the errors rise higher in the lower k_g models because they cannot react fast enough to rapidly evolving systems.

The reason for the oscillations in the errors can be understood by decomposing the gravitational potential into two parts $\phi = \phi_{\mathrm{P}} + \phi_{\mathrm{E}}$. Here we assume that ϕ_{P} is the solution for the Poisson equation ($\Delta\phi_{\mathrm{P}} = 4\pi G\rho$), and ϕ_{E} is the deviation from it. If we plug this in to Eq.(A.2) and use the Poisson equation, we are left with

$$\left(-\frac{1}{c_g^2}\frac{\partial^2}{\partial t^2} + \Delta\right)\phi_{\mathrm{E}} = \frac{1}{c_g^2}\frac{\partial^2}{\partial t^2}\phi_{\mathrm{P}} \tag{A.7}$$

This is the equation which describes the creation and propagation of the error ϕ_{E}. If the initial condition satisfies the Poisson equation, i.e. $\phi_{\mathrm{E}}(t = 0) = 0$, the only errors are generated by the source term on the right hand side and the boundary conditions. Besides the boundary, the source of the error is apparently the second time derivative of the gravitational potential, which is determined by the motion of the density distribution. This is why the error rised at the later times in Fig.A.5 where it was turbulent and messy. Due to the fact that this is a wave equation, any errors that are generated will propagate away out of the boundaries. The creation and propagation of errors is what causes the small oscillations of the errors in all of our test calculations. The amplitudes of the errors are determined by the magnitude of this source term, which can be estimated by combining the Poisson equation, continuity equation and equation of motion. By taking the time derivative of the Poisson equation and using the continuity equation, one can get

$$\frac{\partial}{\partial t}\Delta\phi_{\mathrm{P}} = -4\pi G\nabla\cdot(\rho\boldsymbol{v}) \tag{A.8}$$

and then

$$\frac{\partial}{\partial t}\nabla\phi_{\mathrm{P}} = -4\pi G\rho\boldsymbol{v} \tag{A.9}$$

Similarly by taking the time derivative again and using the equation of motion, one can obtain something like

$$\frac{\partial^2}{\partial t^2}\nabla\phi_{\mathrm{P}} = 4\pi G((\rho\boldsymbol{v}\cdot\nabla)\boldsymbol{v} + \nabla p - \rho\nabla\phi_{\mathrm{P}}) \tag{A.10}$$

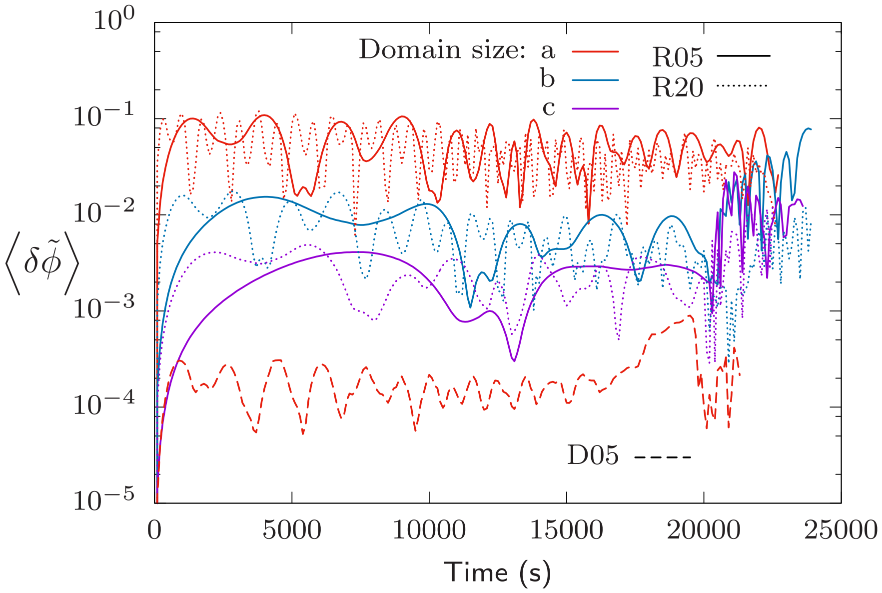

Figure A.5: Time evolution of the average relative error for each model. Colours of the lines denote the domain size as described in Table A.1. Dashed line: aD05 model. Solid lines: $k_g = 5$ models, dotted lines: $k_g = 20$ models.

depending on the physics included. From this equation, it can easily be estimated that

$$\frac{\partial^2}{\partial t^2}\phi_{\mathrm{P}} \sim \mathcal{O}(G\rho(c_s^2 + \boldsymbol{v}^2)) \tag{A.11}$$

So if we normalize Eq.(A.7) by the original Eq.(A.2), we can say that the relative amplitude of the error is roughly

$$\left|\frac{\phi_{\mathrm{E}}}{\phi}\right| \sim \mathcal{O}\left(\frac{c_s^2 + \boldsymbol{v}^2}{c_g^2}\right) \tag{A.12}$$

Provided that c_g is taken larger than the characteristic velocity, or when there is not so much accelerating motion, the right hand side on Eq.(A.7) can be assumed to be sufficiently small.

From the above results, we conclude that our new method can be safely used even for dynamically evolving systems provided that c_g is chosen large enough and the outer boundary condition is given appropriately. Robin boundaries seem to be appropriate for any kind of application due to the fact that gravitational forces can be well approximated by monopoles at large distances from the source. It is also numerically efficient since it only requires information of the neighbouring cell. The only problem is that the boundary should be taken far enough from the source to reduce the errors sufficiently. Larger regions lead to larger computational cost, weakening the advantage of the new method. One possible workaround is to take a wider region only for the gravitational potential, and solving Eq.(A.2) on an extended grid exceeding the region for hydrodynamics. If the density near the hydro boundaries is low enough, or in other words, the total mass inside the region is conserved, it will be possible to approximate that the extended regions are close to vacuum, and calculate the wave equation without the source term. The cost for the wave equation is cheap, thus we can extend the region relatively easily without increasing the total cost. Periodic boundaries are also suitable for this method whenever appropriate. In such cases, the average density of the computational region should be subtracted from the source term of Eq.(A.2).

Fig.A.6 shows the computational time it took until the stars come in contact ($\sim$ 15000 s) for each method. Calculations were carried out on a 172.8 Gflops machine with OpenMP parallelization on 8 threads. It can be seen that the computational time for the gravity part (dashed lines) can be dramatically reduced compared to previous methods, and the benefit becomes more prominent as the scale of the calculation increases. Since our test simulation was dominated by the gravity part with previous methods, the new method improved the overall performance directly. Almost 90% of the computational time was spent on the gravity part using the Poisson solver, whereas the fraction is $\sim 1\%$ with the new method. This is a remarkable improvement, since it is not so common with existing solvers that the time spent on the gravity solver is negligible compared to the hydrodynamics. For other cases where the computational time is dominated by other implementations, the improvement in the gravity part may not be so critical, e.g. in core collapse simulations which implement detailed microphysics, the fraction of time used for computing gravity is typically below $\sim 10\%$, so the reduction of the total time will be at most $\sim 10\%$. The computational time for the gravity part with this method scales linearly to the number of cells, which is much better than previous methods which usually scale as $\mathcal{O}(N^2)$ or $\mathcal{O}(N \log N)$. Multigrid methods are supposed to scale as $\mathcal{O}(N)$ too, but the absolute number of operations are obviously much smaller with the new method and much more simpler. Our method will suit even more on even larger scale simulations parallelized by MPI. In these cases the communication between memories is sometimes the bottleneck, but our new method will not be restricted by this since it does not require intensive communication. It should also be compatible for adaptive mesh refinement or nested grid techniques, and in this way, the outer boundary can be taken far enough without significantly increasing the computational cost.

A.5 Conclusion

A new method has been introduced to treat self-gravity in Eulerian hydrodynamical simulations, by modifying the Poisson equation into an inhomogeneous wave equation. As long as the gravitation propagation speed is taken to be larger than the hydrodynamical characteristic speed, the results agree with solutions for the Poisson equation depending on the boundary condition. If the errors from the boundary are removed in some manner, by applying Dirichlet boundaries or placing the boundary far away, the solution almost perfectly satisfies the Poisson equation. The computational time of the gravity part was reduced by an order of magnitude, and it should become more prominent for larger scale simulations. It is also fully compatible for numerical techniques such as parallelization, nested grids, adaptive mesh refinement, extending its superiority over existent methods.

The sole parameter that needs to be set is c_g, the gravitational propagation speed. This should ideally be taken as the speed of light, but our test simulations suggest that it can be taken to fairly small values as long as it exceeds the characteristic velocity of

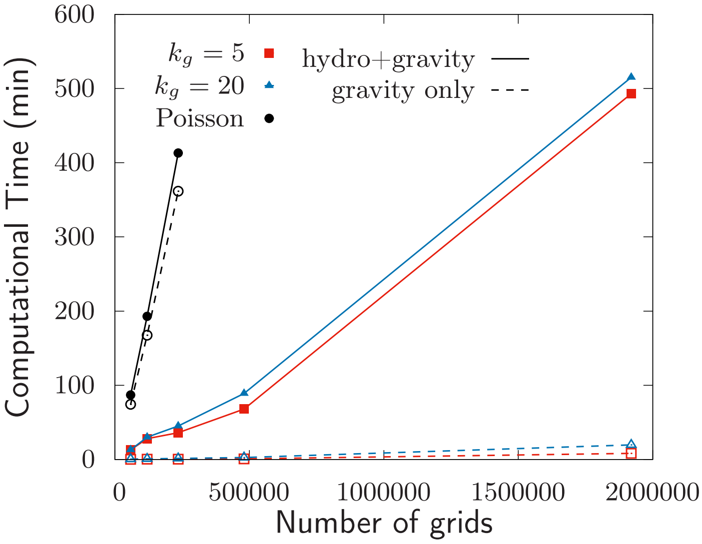

Figure A.6: Computational time until the stars contact for different methods. Square plots: R05 models, Triangle plots: R20 models, Circle plots: same calculation with Poisson solver. Solid lines: total computational time, Dashed lines: time for the gravity part only.

the hydrodynamics. Considering the gain in computational time it is good that we can take it fairly small, but the effects on the errors should be clarified in future studies.

"Those who explore an unknown world are travelers without a map; the map is the result of exploration. The position of their destination is not known to them, and the direct path that leads to it is not yet made."
Hideki Yukawa (1907–1981)

B

The Magnetohydrodynamic Code

Here I will briefly introduce the details of my hydrodynamical code `HORMONE` used in Appendix A.

B.1 Numerical Scheme

The code solves the ideal magnetohydrodynamic (MHD) equations in the conservative form.

$$\frac{\partial \boldsymbol{U}}{\partial t} + \nabla \cdot \boldsymbol{F} = \boldsymbol{S} \tag{B.1}$$

where $\boldsymbol{U}$ contains the conserved variables and $\boldsymbol{F}$ is the flux, and $\boldsymbol{S}$ is the source term.

$$\boldsymbol{U} = \begin{pmatrix} \rho \\ \rho u \\ \rho v \\ \rho w \\ B_x \\ B_y \\ B_z \\ e \end{pmatrix}, \boldsymbol{F_x} = \begin{pmatrix} \rho u \\ \rho u^2 + p_{\mathrm{T}} - B_x^2 \\ \rho v u - B_x B_y \\ \rho w u - B_x B_z \\ 0 \\ B_y u - B_x v \\ B_z u - B_x w \\ (e + p_{\mathrm{T}})u - B_x(uB_x + vB_y + wB_z) \end{pmatrix} \cdots \tag{B.2}$$

Here $\boldsymbol{v} = (u, v, w)$ is the velocity $\boldsymbol{B} = (B_x, B_y, B_z)$ the magnetic field, $p_{\mathrm{T}} = p + \frac{1}{2}(B_x^2 + B_y^2 + B_z^2)$ the total pressure. $\boldsymbol{F_y}$ and $\boldsymbol{F_z}$ are similar to $\boldsymbol{F_x}$. An ideal equation of state is assumed, i.e. $p = (\gamma - 1)\left[e - \frac{1}{2}\rho(u^2 + v^2 + w^2) - \frac{1}{2}(B_x^2 + B_y^2 + B_z^2)\right]$. B_x becomes constant from the divergence free condition $\nabla \cdot \boldsymbol{B} = 0$.

This equation is solved by discretizing the spatial domain into cells. Let us first consider the 1D case ($\boldsymbol{F_y} = \boldsymbol{F_z} = 0$). In Fig.B.1 I show the notations of the discretization. Physical values are assigned at the centre of the cells, and cell interfaces are denoted by half integers. Discretization of the equation is done by considering con-

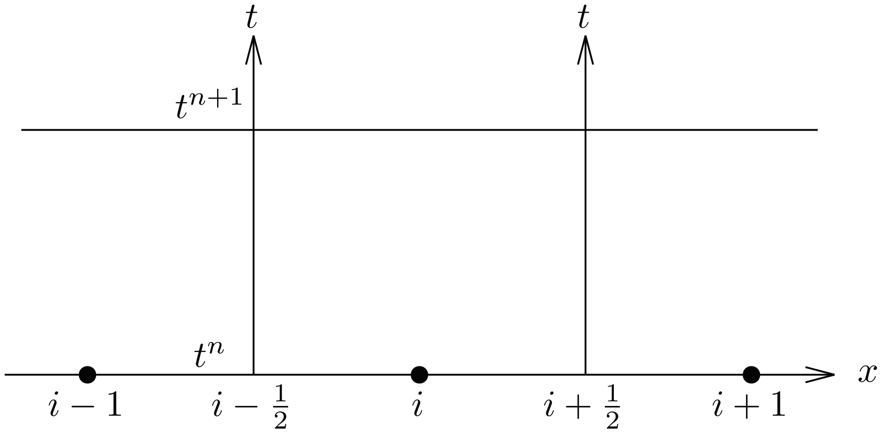

Figure B.1: Notations of the discretization of space and time.

servation laws in space-time. In a one-dimensional case, if we integrate Eq.B.2 over a closed volume in space-time, the conservation law gives us

$$\iint_V \left(\frac{\partial \boldsymbol{U}}{\partial t} + \frac{\partial \boldsymbol{F}}{\partial x} \right) dxdt = \oint (\boldsymbol{U}dx - \boldsymbol{F}(\boldsymbol{U})dt) = 0 \tag{B.3}$$

The first equality is given by Green's theorem. If we the rectangle enclosed by the lines in Fig.B.1 as the control volume, this becomes

$$\begin{aligned}\int_{x_{i-\frac{1}{2}}}^{x_i+\frac{1}{2}} \widetilde{\boldsymbol{U}}(x, t^{n+1})dx = &\int_{x_i-\frac{1}{2}}^{x_i+\frac{1}{2}} \widetilde{\boldsymbol{U}}(x, t^n)dx \\ &+ \int_0^{\Delta t} \boldsymbol{F}\left[\widetilde{\boldsymbol{U}}(x_{i-\frac{1}{2}}, t)\right] dt - \int_0^{\Delta t} \boldsymbol{F}\left[\widetilde{\boldsymbol{U}}(x_{i+\frac{1}{2}}, t)\right] dt\end{aligned} \tag{B.4}$$

where $\Delta t = t^{n+1} - t^n$ is the time interval. By taking small enough time intervals satisfying the Courant-Friedrichs-Lewy (CFL) condition, $\boldsymbol{U}$ can be assumed to be constant along the time direction

$$\widetilde{\boldsymbol{U}}(x_{i-\frac{1}{2}}, t) = \boldsymbol{U}_{i-\frac{1}{2}}(0) = \text{const.} \tag{B.5}$$

$$\widetilde{\boldsymbol{U}}(x_{i-\frac{1}{2}}, t) = \boldsymbol{U}_{i-\frac{1}{2}}(0) = \text{const.} \tag{B.6}$$

Thus the integrals in the second and third terms on the right hand side can be computed easily. Then the values of the variables at the i-th cell and time step $n+1$ can be obtained by

$$\boldsymbol{U}_i^{n+1} = \boldsymbol{U}_i^n + \frac{\Delta t}{\Delta x}\left[\boldsymbol{F}_{i-\frac{1}{2}} - \boldsymbol{F}_{i+\frac{1}{2}}\right] \tag{B.7}$$

where Δx is the spatial interval, $\boldsymbol{U}_i^n \equiv \int_{x_{i-1/2}}^{x_{i+1/2}} \widetilde{\boldsymbol{U}}(x, t^n)dx/\Delta x$ and $\boldsymbol{F}_{i\pm\frac{1}{2}} = \boldsymbol{F}(\boldsymbol{U}_{i\pm\frac{1}{2}}(0))$. Given an appropriate initial condition for $\boldsymbol{U}_i$, all we need is to somehow evaluate the flux $\boldsymbol{F}$ appropriately. The flux is best given by solving the Riemann problems at each interface. Such methods are called "Godunov-type methods". However, obtaining the exact solution of Riemann problems are usually not suitable for practical use where we need to compute fluxes for every cell interface. A common procedure is to solve the Riemann approximately, under some reasonable assumptions. For the flux I use the HLLD approximate Riemann solver, in which it solves the MHD Riemann problem approximately by reducing the number of characteristics based on an assumption that the normal velocity v_x is constant inside the "Riemann fan" (Miyoshi and Kusano, 2005).

The physical values on each side of the cell faces are required to evaluate the flux. Most simply, one can use the cell centre values on each side, assuming that the physical variables are constant throughout the cell. To increase the spatial accuracy, I use Monotone Upwind Schemes for Scalar Conservation Laws (MUSCL) interpolation with a minmod flux limiter to interpolate values at the interfaces (van Leer, 1979). That is,

$$u^L_{i+1/2} = u_i + \frac{1}{2}\Phi(r)(u_i - u_{i-1}), u^R_{i-1/2} = u_i - \frac{1}{2}\Phi(1/r)(u_{i+1} - u_i) \tag{B.8}$$

$$\Phi(r) = \max[0, \min(1, r)] \tag{B.9}$$

where $u^L_{i+1/2}$ and $u^R_{i-1/2}$ expresses the values of the physical variables on the left and right side of the interface respectively. Use of this type of interpolation gives 2nd order accuracy.

For time integration, I use the Total Variation Diminishing (TVD) Runge-Kutta method of the 3rd order, although the code contains a switch to easily change to other orders. In the TVD Runge-Kutta method the integration is divided into several steps, for example

$$\boldsymbol{U}^{(1)} = \boldsymbol{U}^n + \Delta t \boldsymbol{L}(\boldsymbol{U}^n) \tag{B.10}$$

$$\boldsymbol{U}^{(2)} = \frac{3}{4}\boldsymbol{U}^n + \frac{1}{4}\boldsymbol{U}^{(1)} + \frac{1}{4}\Delta t \boldsymbol{L}(\boldsymbol{U}^{(1)}) \tag{B.11}$$

$$\boldsymbol{U}^{n+1} = \frac{1}{3}\boldsymbol{U}^n + \frac{2}{3}\boldsymbol{U}^{(2)} + \frac{2}{3}\Delta t \boldsymbol{L}(\boldsymbol{U}^{(2)}) \tag{B.12}$$

for 3rd order.

For multi-dimensional calculations, we use the unsplit method

and divide the CFL number by the number of dimensions. To ensure the divergence-free condition, I use the hyperbolic divergence cleaning method, or the "9-wave" method (Dedner et al., 2002). This is a simple method that just diffuses and advects $\nabla \cdot \boldsymbol{B}$ by solving an extra set of equations as below.

$$\frac{\partial \boldsymbol{B}}{\partial t} + \nabla \times \boldsymbol{E} + \nabla \phi = 0 \tag{B.13}$$

$$\frac{\partial \phi}{\partial t} + c_h^2 \nabla \cdot \boldsymbol{B} = -\frac{c_h^2}{c_p^2}\phi \tag{B.14}$$

Combining these equations, it simply becomes

$$\frac{\partial^2}{\partial t^2}(\nabla \cdot \boldsymbol{B}) + \frac{c_h^2}{c_p^2}\frac{\partial}{\partial t}(\nabla \cdot \boldsymbol{B}) - c_h^2 \nabla^2 (\nabla \cdot \boldsymbol{B}) = 0 \tag{B.15}$$

Here c_h is an arbitrary parameter that determines the characteristic speed of the artificial waves. It is usually sufficient to take it as $c_h = c_{\text{CFL}}\Delta x/\Delta t$.

I use three types of spatial coordinates; cartesian, cylindrical and spherical. For the cartesian case, the source term $\boldsymbol{S}$When curvilinear coordinates are used, we use variables on a physical basis, and modify the source term to account for the curved coordinates. For cylindrical coordinates $(x_1, x_2, x_3) = (r, \phi.z)$, the source term becomes

$$\boldsymbol{S}_{\mathrm{cyl}} = \left(0, \frac{\rho\tilde{v}_\phi^2 - \tilde{B}_\phi^2}{r} + \frac{p_T}{r}, \frac{\tilde{B}_r\tilde{B}_\phi - \rho\tilde{v}_r\tilde{v}_\phi}{r}, 0, 0, \frac{\Omega_\phi}{r}, 0, 0\right)^{\mathrm{T}} \tag{B.16}$$

and for spherical coordinates $(x_1, x_2, x_3) = (r, \theta, \varphi)$, it becomes

$$\boldsymbol{S}_{\mathrm{sph}} = \begin{pmatrix} 0 \\ \dfrac{\rho\tilde{v}_\theta^2 - \tilde{B}_\theta^2}{r} + \dfrac{\rho\tilde{v}_\varphi^2}{r} + \dfrac{2p_T}{r} \\ \dfrac{\tilde{B}_r\tilde{B}_\theta - \rho\tilde{v}_r\tilde{v}_\theta}{r} + \dfrac{\rho\tilde{v}_\varphi^2 - \tilde{B}_\varphi^2 + p_T}{r}\cot\theta \\ \dfrac{\tilde{B}_\theta\tilde{B}_\varphi - \rho\tilde{v}_\theta\tilde{v}_\varphi}{r}\cot\theta + \dfrac{\tilde{B}_r\tilde{B}_\varphi - \rho\tilde{v}_r\tilde{v}_\varphi}{r} \\ 0 \\ \dfrac{\Omega_3}{r} \\ \dfrac{\Omega_1}{r}\cot\theta - \dfrac{\Omega_2}{r} \\ 0 \end{pmatrix} \tag{B.17}$$

Other physical processes such as radiation transfer, or neutrino transfer can be easily incorporated by adding their contributions in the source term.

only contains contributions from gravity.

$$\boldsymbol{S}_{\mathrm{grav}} = (0, \rho g_x, \rho g_y, \rho g_z, 0, 0, 0, \rho\boldsymbol{v}\cdot\boldsymbol{g})^{\mathrm{T}} \tag{B.18}$$

The gravity term $\boldsymbol{g}$ is obtained by taking the gradients of the gravitational potential ϕ_g which is calculated elsewhere (see Appendix A).

B.2 MICCG method

To include effects of self gravity in the usual way, we need to solve the Poisson equation for gravitational potentials.

$$\Delta\Phi = 4\pi G\rho \tag{B.19}$$

This type of partial differential equation is classified as an elliptic equation from its eigenvalues. In order to solve this numerically, we have to convert this to a finite difference form, and this becomes a large system of linear equations. There are several solvers for these equations, but for calculations in this thesis, we used a method called the modified incomplete Cholesky conjugate gradient (MICCG) method. It is by far one of the fastest and most efficient solvers. Here, we introduce detailed discriptions of the conjugate gradient (CG) method, and show several preconditioning methods used to improve computational efficiency.

B.2.1 Conjugate Gradient Method

CG is the most popular iterative method for solving large systems of linear equations. We consider systems taking the form

$$Ax = b \tag{B.20}$$

where x is the unknown vector, b a known vector, and A a known, square, symmetric, positive-definite matrix. Positive-definite means that it fulfills the following condition.

$$(\boldsymbol{x}, A\boldsymbol{x}) = \boldsymbol{x}^T A\boldsymbol{x} > 0 \tag{B.21}$$

Now, let us define $\boldsymbol{x}^*$ as the solution for eq.B.20. Then we define a function

$$\begin{aligned}
F(\boldsymbol{x}) &= \frac{1}{2}(\boldsymbol{x}-\boldsymbol{x}^*, A(\boldsymbol{x}-\boldsymbol{x}^*)) \\
&= \frac{1}{2}(\boldsymbol{x}-\boldsymbol{x}^*)^T A(\boldsymbol{x}-\boldsymbol{x}^*) \\
&= \frac{1}{2}\left(\boldsymbol{x}^T A\boldsymbol{x} - \boldsymbol{x}^T A\boldsymbol{x}^* - \boldsymbol{x}^{*T} A\boldsymbol{x} + \boldsymbol{x}^{*T} A\boldsymbol{x}^*\right) \\
&= \frac{1}{2}(\boldsymbol{x}, A\boldsymbol{x}) - (\boldsymbol{x}, A\boldsymbol{x}^*) + \frac{1}{2}(\boldsymbol{x}^*, A\boldsymbol{x}^*) \\
&= \frac{1}{2}(\boldsymbol{x}, A\boldsymbol{x}) - (\boldsymbol{x}, \boldsymbol{b}) + \frac{1}{2}(\boldsymbol{x}^*, A\boldsymbol{x}^*)
\end{aligned} \tag{B.22}$$

Because A is a positive-definite matrix, $F(\boldsymbol{x}) \geq 0$, and the equality holds for $\boldsymbol{x}-\boldsymbol{x}^* = 0$, or $F(\boldsymbol{x}^*) = 0$. $F(\boldsymbol{x})$ is a function such that if we differentiate it, it becomes

$$\begin{aligned}
F'(\boldsymbol{x}) &= \left\{\frac{1}{2}\boldsymbol{x}^T A\boldsymbol{x} - \boldsymbol{x}^{\boldsymbol{T}}\boldsymbol{b}\right\}' \\
&= \frac{1}{2}A^T\boldsymbol{x} + \frac{1}{2}A\boldsymbol{x} - \boldsymbol{b} \\
&= A\boldsymbol{x} - \boldsymbol{b}
\end{aligned} \tag{B.23}$$

The second to third equality holds because matrix A is symmetrical. So the problem now, is to find an $\boldsymbol{x}$ that minimizes $F(\boldsymbol{x})$.

We start from an arbitrary solution $\boldsymbol{x}_0$, and take a series of steps towards the real solution until we approach a reasonable one. If we define the kth solution as $\boldsymbol{x}_k$, and the direction of search as $\boldsymbol{p}_k$, our recurrence formula will be

$$\boldsymbol{x}_{k+1} = \boldsymbol{x}_k + \alpha_k \boldsymbol{p}_k \tag{B.24}$$

Substitute this into $F(\boldsymbol{x})$

$$\begin{aligned}
F(\boldsymbol{x}_{k+1}) &= F(\boldsymbol{x}_k + \alpha_k\boldsymbol{p}_k) \\
&= \frac{1}{2}(\boldsymbol{x}_k + \alpha_k\boldsymbol{p}_k - \boldsymbol{x}^*)^T A(\boldsymbol{x}_k + \alpha_k\boldsymbol{p}_k - \boldsymbol{x}^*) \\
&= \frac{1}{2}\left\{(\alpha_k\boldsymbol{p}_k)^T A(\alpha_k\boldsymbol{p}_k) + (\boldsymbol{x}_k - \boldsymbol{x}^*)^T A(\boldsymbol{x}_k - \boldsymbol{x}^*)\right. \\
&\qquad \left. + (\boldsymbol{x}_k - \boldsymbol{x}^*)^T A(\alpha_k\boldsymbol{p}_k) + (\alpha_k\boldsymbol{p}_k)^T A(\boldsymbol{x}_k - \boldsymbol{x}^*)\right\} \\
&= \frac{1}{2}{\alpha_k}^2(\boldsymbol{p}_k, A\boldsymbol{p}_k) + \alpha_k(\boldsymbol{p}_k, A(\boldsymbol{x}_k - \boldsymbol{x}^*)) + F(\boldsymbol{x}_k)
\end{aligned} \tag{B.25}$$

If we define the kth residual as $\boldsymbol{r}_k = \boldsymbol{b} - A\boldsymbol{x}_k$,

$$A(\boldsymbol{x}_k - \boldsymbol{x}^*) = A\boldsymbol{x}_k - A\boldsymbol{x}^* = A\boldsymbol{x}_k - \boldsymbol{b} = -\boldsymbol{r}_k \tag{B.26}$$

so

$$F(\boldsymbol{x}_k) = \frac{1}{2}{\alpha_k}^2(\boldsymbol{p}_k, A\boldsymbol{p}_k) - \alpha_k(\boldsymbol{p}_k, \boldsymbol{r}_k) + F(\boldsymbol{x}_k) \tag{B.27}$$

Now, we find $\alpha_k > 0$ that minimizes $F(\boldsymbol{x}_k)$.

$$\begin{aligned}
&\frac{1}{2}{\alpha_k}^2(\boldsymbol{p}_k, A\boldsymbol{p}_k) - \alpha_k(\boldsymbol{p}_k, \boldsymbol{r}_k) + F(\boldsymbol{x}_k)\\
= \;&\frac{1}{2}(\boldsymbol{p}_k, A\boldsymbol{p}_k)\left\{{\alpha_k}^2 - 2\frac{(\boldsymbol{p}_k, \boldsymbol{r}_k)}{(\boldsymbol{p}_k, A\boldsymbol{p}_k)}\alpha_k + \left(\frac{(\boldsymbol{p}_k, \boldsymbol{r}_k)}{(\boldsymbol{p}_k, A\boldsymbol{p}_k)}\right)^2\right\}\\
&\quad -\frac{1}{2}\frac{(\boldsymbol{p}_k, \boldsymbol{r}_k)^2}{(\boldsymbol{p}_k, A\boldsymbol{p}_k)} + F(\boldsymbol{x}_k)\\
= \;&\frac{1}{2}(\boldsymbol{p}_k, A\boldsymbol{p}_k)\left\{\alpha_k - \frac{(\boldsymbol{p}_k, \boldsymbol{r}_k)}{(\boldsymbol{p}_k, A\boldsymbol{p}_k)}\right\}^2 - \frac{1}{2}\frac{(\boldsymbol{p}_k, \boldsymbol{r}_k)^2}{(\boldsymbol{p}_k, A\boldsymbol{p}_k)} + F(\boldsymbol{x}_k)
\end{aligned} \tag{B.28}$$

To minimize $F(\boldsymbol{x}_k)$, α_k should be

$$\alpha_k = \frac{(\boldsymbol{p}_k, \boldsymbol{r}_k)}{(\boldsymbol{p}_k, A\boldsymbol{p}_k)} \tag{B.29}$$

The next residual would be,

$$\begin{aligned}
\boldsymbol{r}_{k+1} &= \boldsymbol{b} - A\boldsymbol{x}_{k+1}\\
&= \boldsymbol{b} - A(\boldsymbol{x}_k + \alpha_k\boldsymbol{p}_k)\\
&= (\boldsymbol{b} - A\boldsymbol{x}_k) - A\alpha_k\boldsymbol{p}_k\\
&= \boldsymbol{r}_k - \alpha_k A\boldsymbol{p}_k
\end{aligned} \tag{B.30}$$

When two vectors, $\boldsymbol{u}, \boldsymbol{v}$ are A-orthogonal, or conjugate, they satisfy

$$\boldsymbol{u}^T A\boldsymbol{v} = (\boldsymbol{u}, A\boldsymbol{v}) = 0 \tag{B.31}$$

This means that $\boldsymbol{u}^T$ and $A\boldsymbol{v}$ are orthogonal. In the CG method, the direction of search is taken as

$$\begin{gathered}
\boldsymbol{p}_{k+1} = \boldsymbol{r}_{k+1} + \beta_k\boldsymbol{p}_k\\
(\boldsymbol{p}_0 = \boldsymbol{r}_0)
\end{gathered} \tag{B.32}$$

β must be chosen so that $\boldsymbol{p}_k$'s are A-orthogonal to each other. That is,

$$(\boldsymbol{p}_{k+1}, A\boldsymbol{p}_k) = 0 \tag{B.33}$$

So substituting B.32 in to B.33, we get

$$\begin{aligned}
(\boldsymbol{r}_{k+1} + \beta_k\boldsymbol{p}_k, A\boldsymbol{p}_k) = (\boldsymbol{r}_{k+1}, A\boldsymbol{p}_k) + (\beta_k\boldsymbol{p}_k, A\boldsymbol{p}_k) = 0\\
\Rightarrow \beta_k = -\frac{(\boldsymbol{r}_{k+1}, A\boldsymbol{p}_k)}{(\boldsymbol{p}_k, A\boldsymbol{p}_k)}
\end{aligned} \tag{B.34}$$

It is known that $\boldsymbol{r}_k$ are orthogonal, and $\boldsymbol{p}_k$ are A-orthogonal to each other.

$$\begin{aligned}(\boldsymbol{r}_i, \boldsymbol{r}_j) &= 0 \quad i \neq j \qquad \text{(B.35)}\\ (\boldsymbol{p}_i, A\boldsymbol{p}_j) &= 0 \quad i \neq j \qquad \text{(B.36)}\end{aligned}$$

Using these conditions, α_k and β_k become

$$\begin{aligned}\alpha_k &= \frac{(\boldsymbol{p}_k, \boldsymbol{r}_k)}{(\boldsymbol{p}_k, A\boldsymbol{p}_k)}\\ &= \frac{(\boldsymbol{r}_k + \beta_{k-1}\boldsymbol{p}_{k-1}, \boldsymbol{r}_k)}{(\boldsymbol{p}_k, A\boldsymbol{p}_k)}\\ &= \frac{(\boldsymbol{r}_k, \boldsymbol{r}_k)}{(\boldsymbol{p}_k, A\boldsymbol{p}_k)}\\ &= \frac{(\boldsymbol{r}_k, \boldsymbol{r}_k)}{(\boldsymbol{p}_k, A\boldsymbol{p}_k)} \qquad \text{(B.37)}\\ \beta_k &= -\frac{(\boldsymbol{r}_{k+1}, A\boldsymbol{p}_k)}{(\boldsymbol{p}_k, A\boldsymbol{p}_k)}\\ &= -\frac{(\boldsymbol{r}_{k+1}, \frac{1}{\alpha_k}\boldsymbol{r}_k - \frac{1}{\alpha_k}\boldsymbol{r}_{k+1})}{(\boldsymbol{p}_k, A\boldsymbol{p}_k)}\\ &= \frac{1}{\alpha_k}\frac{(\boldsymbol{r}_{k+1}, \boldsymbol{r}_{k+1})}{(\boldsymbol{p}_k, A\boldsymbol{p}_k)}\\ &= \frac{(\boldsymbol{r}_{k+1}, \boldsymbol{r}_{k+1})}{(\boldsymbol{r}_k, \boldsymbol{r}_k)} \qquad \text{(B.38)}\end{aligned}$$

To summarize, the CG method goes as follows:

1. Give an arbitrary initial $\boldsymbol{x}_0$
2. Set the initial residual and searching direction as
    - $\boldsymbol{r}_0 = \boldsymbol{b} - A\boldsymbol{x}_0$
    - $\boldsymbol{p}_0 = \boldsymbol{r}_0$
3. Iterate the following :
    (a) $\alpha_k = \dfrac{(\boldsymbol{r}_k, \boldsymbol{r}_k)}{(\boldsymbol{p}_k, A\boldsymbol{p}_k)}$
    (b) $\boldsymbol{r}_{k+1} = \boldsymbol{r}_k - \alpha_k A\boldsymbol{p}_k$
    (c) $\beta_k = \dfrac{(\boldsymbol{r}_{k+1}, \boldsymbol{r}_{k+1})}{\boldsymbol{r}_k, \boldsymbol{r}_k}$
    (d) $\boldsymbol{p}_{k+1} = \boldsymbol{r}_{k+1} + \beta_k\boldsymbol{p}_k$
4. Continue the iteration until $\boldsymbol{r}_k \leq \varepsilon\boldsymbol{b}$ where ϵ is the relative residual error.

B.2.2 Preconditioning

CG is efficient especially when the matrix A is very sparse, including many 0's. But any arbitrary linear equation system will include many non-zero elements in the matrix A. Preconditioning techniques are used to improve the condition number of a matrix. Suppose we have a regular square matrix C of size n. The original equation B.20 will become

$$C^{-1}A(C^T)^{-1}C^T\boldsymbol{x} = C^{-1}\boldsymbol{b} \tag{B.39}$$

If we take

$$\begin{cases} \tilde{A} \equiv C^{-1}A(C^T)^{-1} \\ \tilde{\boldsymbol{b}} \equiv C^{-1}\boldsymbol{b} \end{cases} \tag{B.40}$$

the problem resolves to the below problem.

$$\begin{aligned} \tilde{A}\tilde{\boldsymbol{x}} &= \tilde{\boldsymbol{b}} \\ C^T\boldsymbol{x} &= \tilde{\boldsymbol{x}} \end{aligned} \tag{B.41}$$

This matrix C is called a "preconditioning matrix", and it is convenient to choose C with the following properties.

1. CC^T is similar to A
2. To a vector $\boldsymbol{v}$, it is easy to calculate $C^{-1}\boldsymbol{v}$ and $(C^T)^{-1}\boldsymbol{v}$

There are several ways to choose a preconditioning matrix, but the one we used was "Cholesky decomposition". Cholesky decomposition is to decompose a matrix as

$$A = LL^T \tag{B.42}$$

where L is a lower triangular matrix. If we write it down using elements, it becomes

$$a_{ij} = \sum_{k=1}^{N} l_{ik}l_{jk} \quad (i, j = 1, ..., N) \tag{B.43}$$

Since L is a lower triangular matrix, all elements are 0 for $i < j$, so

$$a_{ij} = \sum_{k=1}^{min(i,j)} c_{ik}c_{jk} \tag{B.44}$$

Solving this system of equations gives us the lower triangular matrix L. But doing Cholesky decomposition properly is extremely time consuming, so it is necessary to simplify the process. One way is to use modifications to the matrix. Decomposing the matrix A as $A = LDL^T$, not $A = LL^T$, is called the adjusted Cholesky decomposition. Another way is to artificially set certain elements to 0, which means, we define a set G as

$$G_A = \left\{(i, j) \in \{1, 2, ..., N\}^2; a_{ij} \neq 0\right\} \tag{B.45}$$

$$G_A \subset G \tag{B.46}$$

and only leave over elements with subscripts included in this set G when decomposing the matrix A. Other elements can be set to 0. This is called incomplete Cholesky decomposition. There are 4 popular ways of simplifying Cholesky decomposition, and we give brief discriptions of each.

ICCG(1,1) method

Set $G = G_A$. The matrix A will be decomposed as $A = LL^T + R$. R is because L is not an exact Cholesky decomposition. We choose the preconditioning matrix as $C = L$, which gives us

$$A = U^T D U \tag{B.47}$$

where U is an upper triangular matrix and D a diagonal matrix. Let us define the diagonal elements of U as $\tilde{\boldsymbol{a}}_i$, and the sub-diagonal elements as $\tilde{\boldsymbol{b}}_i$,$\tilde{\boldsymbol{c}}_i$, and the diagonal elements of D as $\tilde{\boldsymbol{d}}_i$, which is

$$\begin{array}{lcl} a_i & = & a_{ii} \\ b_i & = & a_{i,i+1} \\ c_i & = & a_{i,i+m} \end{array}$$

Then, the elements of the preconditioning matrix will become

$$\left\{ \begin{array}{lcl} \tilde{d}_i^{-1} & = & \tilde{a}_i = a_i - b_{i-1}^2 \tilde{d}_{i-1} - c_{i-m}^2 \tilde{d}_{i-m} \\ \tilde{b}_i & = & b_i \\ \tilde{c}_i & = & c_i \end{array} \right. \tag{B.48}$$

Other elements are zero.

MICCG(1,1) method

This method is based on the ICCG(1,1) method, with modifications by Gustaffson.

$$\left\{ \begin{array}{lcl} \tilde{d}_i^{-1} & = & \tilde{a}_i = a_i - b_{i-1}^2 \tilde{d}_{i-1} - c_{i-m}^2 \tilde{d}_{i-m} \\ & & \qquad -\alpha(b_{i-1} c_{i-1} \tilde{d}_{i-1} + b_{i-m} c_{i-m} \tilde{d}_{i-m}) \\ \tilde{b}_i & = & b_i \\ \tilde{c}_i & = & c_i \end{array} \right. \tag{B.49}$$

$\alpha < 1$ is a constant. It is usually taken as $\alpha = 0.95$

ICCG(1,2) method

We choose another two lines in the set G, not $G = G_A$.

$$G = \{(i,j); j = i, i \pm 1, i \pm m, i \pm (m-1)\} \tag{B.50}$$

This gives us the elements for the preconditioning matrix as

$$\left\{ \begin{array}{lcl} \tilde{d}_i^{-1} & = & \tilde{a}_i = a_i - \tilde{b}_i^2 \tilde{d}_{i-1} - \tilde{c}_i^2 \tilde{d}_{i-m} - \tilde{e}_i^2 \tilde{d}_{i-m+1} \\ \tilde{b} & = & b_i - \tilde{c}_i \tilde{e}_i \tilde{d}_{i-m} \\ \tilde{c}_i & = & c_i \\ \tilde{e}_i & = & -c_i \tilde{b}_{i-m+1} \tilde{d}_{i-m} \end{array} \right. \tag{B.51}$$

MICCG(1,2) method

Modifications are made to the ICCG(1,2) method by Gustaffson, yet again.

$$\left\{ \begin{array}{lcl} \tilde{d}_i^{-1} & = & \tilde{a}_i = a_i - \tilde{b}_i^2 \tilde{d}_{i-1} - \tilde{c}_i^2 \tilde{d}_{i-m} - \tilde{e}_i^2 \tilde{d}_{i-m+1} \\ & & \qquad -\alpha \left(\tilde{b}_i \tilde{e}_{i+m-2} \tilde{d}_{i-1} + \tilde{b}_{i-m+2} \tilde{e}_i \tilde{d}_{i-m+1} \right) \\ \tilde{b} & = & b_i - \tilde{c}_i \tilde{e}_i \tilde{d}_{i-m} \\ \tilde{c}_i & = & c_i \\ \tilde{e}_i & = & -c_i \tilde{b}_{i-m+1} \tilde{d}_{i-m} \end{array} \right. \tag{B.52}$$

B.2.3 General Form of the MICCG method

The original form of preconditioned CG methods solve B.41, but there are ways to improve the method so that C does not appear so many times.

Now, if we solve $\tilde{A}\tilde{x} = \tilde{b}$ with normal CG methods, it is

1. $\tilde{\boldsymbol{p}}_0 = \tilde{\boldsymbol{r}}_0 = C^{-1}\boldsymbol{b} - C^{-1}A(C^T)^{-1}\tilde{\boldsymbol{x}}$
2. $\alpha_k = \dfrac{(\tilde{\boldsymbol{r}}_k, \tilde{\boldsymbol{r}}_k)}{(\tilde{\boldsymbol{p}}_k, C^{-1}A(C^T)^{-1}\tilde{\boldsymbol{p}}_k)}$
3. $\tilde{\boldsymbol{x}}_{k+1} = \tilde{\boldsymbol{x}}_k + \alpha_k \tilde{\boldsymbol{p}}_k$
4. $\tilde{\boldsymbol{r}}_{k+1} = \tilde{\boldsymbol{r}}_k - \alpha_k C^{-1}A(C^T)^{-1}\tilde{\boldsymbol{p}}_k$
5. $\beta_{k+1} = \dfrac{(\tilde{\boldsymbol{r}}_{k+1}, \tilde{\boldsymbol{r}}_{k+1})}{(\tilde{\boldsymbol{r}}_k, \tilde{\boldsymbol{r}}_k)}$
6. $\tilde{\boldsymbol{p}}_{k+1} = \tilde{\boldsymbol{r}}_{k+1} + \beta_{k+1}\tilde{\boldsymbol{p}}_k$

If we take $\tilde{\boldsymbol{r}}_k = C^{-1}\boldsymbol{r}_k, \tilde{\boldsymbol{p}}_k = C^T\boldsymbol{p}_k$, and with $\tilde{\boldsymbol{x}} = C^T\boldsymbol{x}$

$$\begin{aligned}
C^T\boldsymbol{p}_0 &= C^{-1}\boldsymbol{r}_0 = C^{-1}\boldsymbol{b} - C^{-1}A(C^T)^{-1}C^T\boldsymbol{x} \\
&\Rightarrow CC^T\boldsymbol{p}_0 = \boldsymbol{r}_0 = \boldsymbol{b} - A\boldsymbol{x} && \text{(B.53)} \\
\alpha_k &= \frac{(C^{-1}\boldsymbol{r}_k, C^{-1}\boldsymbol{r}_k)}{(C^T\boldsymbol{p}_k, C^{-1}A(C^T)^{-1}C^T\boldsymbol{p}_k)} = \frac{\boldsymbol{r}_k^T(C^{-1})^TC^{-1}\boldsymbol{r}_k}{\boldsymbol{p}_k^TCC^{-1}A(C^T)^{-1}C^T\boldsymbol{p}_k} \\
&\Rightarrow \alpha_k = \frac{((CC^T)^{-1}\boldsymbol{r}_k, \boldsymbol{r}_k)}{(\boldsymbol{p}_k, A\boldsymbol{p}_k)} && \text{(B.54)} \\
C^T\boldsymbol{x}_{k+1} &= C^T\boldsymbol{x}_k + \alpha_k C^T\boldsymbol{p}_k \\
&\Rightarrow \boldsymbol{x}_{k+1} = \boldsymbol{x}_k + \alpha_k\boldsymbol{p}_k && \text{(B.55)} \\
C^{-1}\boldsymbol{r}_{k+1} &= C^{-1}\boldsymbol{r}_k - \alpha_k C^{-1}A(C^T)^{-1}C^T\boldsymbol{p}_k \\
&\Rightarrow \boldsymbol{r}_{k+1} = \boldsymbol{r}_k - \alpha_k A\boldsymbol{p}_k && \text{(B.56)} \\
\beta_{k+1} &= \frac{(C^{-1}\boldsymbol{r}_{k+1}, C^{-1}\boldsymbol{r}_{k+1})}{(C^{-1}\boldsymbol{r}_k, C^{-1}\boldsymbol{r}_k)} \\
&\Rightarrow \beta_{k+1} = \frac{((CC^T)^{-1}\boldsymbol{r}_{k+1}, \boldsymbol{r}_{k+1})}{((CC^T)^{-1}\boldsymbol{r}_k, \boldsymbol{r}_k)} && \text{(B.57)} \\
C^T\boldsymbol{p}_{k+1} &= C^{-1}\boldsymbol{r}_{k+1} + \beta_{k+1}C^T\boldsymbol{p}_k \\
&\Rightarrow \boldsymbol{p}_{k+1} = (C^T)^{-1}C^{-1}\boldsymbol{r}_{k+1} + \beta_{k+1}\boldsymbol{p}_k \\
&\Rightarrow \boldsymbol{p}_{k+1} = (CC^T)^{-1}\boldsymbol{r}_{k+1} + \beta_{k+1}\boldsymbol{p}_k && \text{(B.58)}
\end{aligned}$$

So now we summarize the generalized form of preconditioned CG methods.

1. $\boldsymbol{r}_0 = \boldsymbol{b} - A\boldsymbol{x}_0$
2. $\boldsymbol{p}_0 = (CC^T)^{-1}\boldsymbol{r}_0$
3. Iterate the following
   - $\alpha_k = \dfrac{((CC^T)^{-1}\boldsymbol{r}_k, \boldsymbol{r}_k)}{(\boldsymbol{p}_k, A\boldsymbol{p}_k)}$

- $\boldsymbol{x}_{k+1} = \boldsymbol{x}_k + \alpha_k \boldsymbol{p}_k$
- $\boldsymbol{r}_{k+1} = \boldsymbol{r}_k - \alpha_k A \boldsymbol{p}_k$
- $\beta_{k+1} = \dfrac{((CC^T)^{-1}\boldsymbol{r}_{k+1}, \boldsymbol{r}_{k+1})}{((CC^T)^{-1}\boldsymbol{r}_k, \boldsymbol{r}_k)}$
- $\boldsymbol{p}_{k+1} = (CC^T)^{-1}\boldsymbol{r}_{k+1} + \beta_{k+1}\boldsymbol{p}_k$

In this way, we do not need precise precondition matrices, but only $(CC^T)^{-1}$.

Acknowledgements

First of all, I would like to express my deep gratitudes to my supervisor Prof. Shoichi Yamada, for all the education he has provided me for this six years. I would never have been able to reach this stage without his persistent kindness and patience for me to learn things. Especially the discussions in lunch seminars and colloquia were extremely valuable to me. I also had the privilege to attend many workshops and conferences which led to many new collaborations and friendships thanks to his financial support.

I am also very grateful for Dr. Hiroki Nagakura for always responding to my discussions and giving me new ideas. His deep knowledge in physics and strong vitality has inspired me so much both in research and social life. I also appreciate Dr. Hidetomo Sawai for providing me his hydrodynamical code that I used in my earlier works, and for teaching me the basics of programming. I also need to acknowledge my collaborators Dr. Hirotada Okawa and Dr. Kotaro Fujisawa for the fruitful advices in my work.

My life in Yamada lab. would never have been better without my senior colleagues, Dr. Shun Furusawa, Dr. Kazuya Takahashi, Dr. Yu Yamamoto, Dr. Wakana Iwakami, Dr. Ko Nakamura, Dr. Motoyuki Saijo and Dr. Nobutoshi Yasutake. They have always been my role models and I enjoyed all the enthusiastic scientific and non-scientific talks with them. I also thank Toshiki Nakanishi, Yuki Okamoto and Takahiro Ono for helping out each other in getting our masters and bachelors degree. All my junior colleagues in Yamada lab and all the members of Maeda lab have been helpful too. I also cannot forget to appreciate our secretaries Mrs. Yoshie Sato and Mrs. Haruko Yoshimura for caring for us like their own children.

Finally, I thank all my parents, sister, brother and friends for all their support in my daily lives.

This work was supported by the Grants-in-Aid for the Scientific Research from the Ministry of Education, Culture, Sports, Science, and Technology (MEXT) of Japan (NoS. 24740165, and 24244036), the HPCI Strategic Program of MEXT, MEXT Grant-in-Aid for Scientific Research on Innovative Areas “New Developments in Astrophysics Through Multi-Messenger Observations of Gravitational Wave Sources” (Grant Number A05 24103006), Research Grant for Young Scientists, Early Bird Program from Waseda Research Institute for Science and Engineering, and the JSPS Research fellowship for young scientists (DC2, No 16J07613).

Bibliography

Abbott, B. P., Abbott, R., Abbott, T. D., Abernathy, M. R., Acernese, F., Ackley, K., Adams, C., Adams, T., Addesso, P., Adhikari, R. X., and et al.: 2016a, The Astrophysical Journal Letters **818**, L22

Abbott, B. P., Abbott, R., Abbott, T. D., Abernathy, M. R., Acernese, F., Ackley, K., Adams, C., Adams, T., Addesso, P., Adhikari, R. X., and et al.: 2016b, Physical Review Letters **116(24)**, 241103

Abbott, B. P., Abbott, R., Abbott, T. D., Abernathy, M. R., Acernese, F., Ackley, K., Adams, C., Adams, T., Addesso, P., Adhikari, R. X., and et al.: 2016c, Physical Review Letters **116(6)**, 061102

Aitken, R. G.: 1918, The binary stars

Alcubierre, M.: 2008, Introduction to 3+1 numerical relativity, Vol. 2, Oxford University Press Oxford

Alcubierre, M., Brügmann, B., Holz, D., Takahashi, R., Brandt, S., Seidel, E., Thornburg, J., and Ashtekar, A.: 2001, International Journal of Modern Physics D **10**, 273

Antoniadis, J., Freire, P. C. C., Wex, N., Tauris, T. M., Lynch, R. S., van Kerkwijk, M. H., Kramer, M., Bassa, C., Dhillon, V. S., Driebe, T., Hessels, J. W. T., Kaspi, V. M., Kondratiev, V. I., Langer, N., Marsh, T. R., McLaughlin, M. A., Pennucci, T. T., Ransom, S. M., Stairs, I. H., van Leeuwen, J., Verbiest, J. P. W., and Whelan, D. G.: 2013, Science **340**, 448

Barbon, R., Ciatti, F., and Rosino, L.: 1979, Astronomy & Astrophysics **72**, 287

Belczynski, K., Dominik, M., Bulik, T., O'Shaughnessy, R., Fryer, C., and Holz, D. E.: 2010, The Astrophysical Journal Letters **715**, L138

Belczynski, K., Kalogera, V., and Bulik, T.: 2002, The Astrophysical Journal **572**, 407

Benvenuto, O. G., Bersten, M. C., and Nomoto, K.: 2013, The Astrophysical Journal **762**, 74

Benvenuto, O. G. and De Vito, M. A.: 2003, Monthly Notices of the Royal Astronomical Society **342**, 50

Bergfors, C., Brandner, W., Janson, M., Daemgen, S., Geissler, K., Henning, T., Hippler, S., Hormuth, F., Joergens, V., and Köhler, R.: 2010, Astronomy & Astrophysics **520**, A54

Bersten, M. C., Benvenuto, O. G., Folatelli, G., Nomoto, K., Kuncarayakti, H., Srivastav, S., Anupama, G. C., Quimby, R., and Sahu, D. K.: 2014, The Astronomical Journal **148**, 68

Black, D. C. and Bodenheimer, P.: 1975, The Astrophysical Journal **199**, 619

Blagorodnova, N., Kotak, R., Polshaw, J., Kasliwal, M. M., Cao, Y., Cody, A. M., Doran, G. B., Elias-Rosa, N., Fraser, M., Fremling, C., Gonzalez-Fernandez, C., Harmanen, J., Jencson, J., Kankare, E., Kudritzki, R.-P., Kulkarni, S. R., Magnier, E., Manulis, I., Masci, F. J., Mattila, S., Nugent, P., Ochner, P., Pastorello, A., Reynolds, T., Smith, K., Sollerman, J., Taddia, F., Terreran, G., Tomasella, L., Turatto, M., Vreeswijk, P., Wozniak, P., and Zaggia, S.: 2016, ArXiv e-prints

Bodenheimer, P., Burkert, A., Klein, R. I., and Boss, A. P.: 2000, Protostars and Planets IV p. 675

Burgasser, A. J., Reid, I. N., Siegler, N., Close, L., Allen, P., Lowrance, P., and Gizis, J.: 2007, Protostars and Planets V pp 427–441

Cao, Y., Kasliwal, M. M., Arcavi, I., Horesh, A., Hancock, P., Valenti, S., Cenko, S. B., Kulkarni, S. R., Gal-Yam, A., Gorbikov, E., Ofek, E. O., Sand, D., Yaron, O., Graham, M., Silverman, J. M., Wheeler, J. C., Marion, G. H., Walker, E. S., Mazzali, P., Howell, D. A., Li, K. L., Kong, A. K. H., Bloom, J. S., Nugent, P. E., Surace, J., Masci, F., Carpenter, J., Degenaar, N., and Gelino, C. R.: 2013, The Astrophysical Journal Letters **775**, L7

Cardelli, J. A., Clayton, G. C., and Mathis, J. S.: 1989, The Astrophysical Journal **345**, 245

Cheng, A.: 1974, Astrophysics & Space Science **31**, 49

Chesneau, O., Millour, F., De Marco, O., Bright, S. N., Spang, A., Banerjee, D. P. K., Ashok, N. M., Kamiński, T., Wisniewski, J. P., Meilland, A., and Lagadec, E.: 2014, Astronomy & Astrophysics **569**, L3

Chevalier, R. A.: 1986, Highlights of Astronomy **7**, 599

Chini, R., Hoffmeister, V. H., Nasseri, A., Stahl, O., and Zinnecker, H.: 2012, Monthly Notices of the Royal Astronomical Society **424**, 1925

Couch, S. M.: 2013, The Astrophysical Journal **775**, 35

Couch, S. M., Chatzopoulos, E., Arnett, W. D., and Timmes, F. X.: 2015, ApJL **808**, L21

Couch, S. M., Graziani, C., and Flocke, N.: 2013, The Astrophysical Journal **778(2)**, 181

De Greve, J.-P. and De Loore, C.: 1977, Astrophysics and Space Science **50**, 75

de Jager, C., Nieuwenhuijzen, H., and van der Hucht, K. A.: 1988, A & A Supplements Series **72**, 259

de Kool, M.: 1990, The Astrophysical Journal **358**, 189

De Loore, C. W. H. and Doom, C. (eds.): 1992, Structure and evolution of single and binary stars, Vol. 179 of Astrophysics and Space Science Library

de Vries, N., Portegies Zwart, S., and Figueira, J.: 2014, Monthly Notices of the Royal Astronomical Society **438**, 1909

Dedner, A., Kemm, F., Kröner, D., Munz, C.-D., Schnitzer, T., and Wesenberg, M.: 2002, Journal of Computational Physics **175**, 645

Delgado, A. J. and Thomas, H.-C.: 1981, Astronomy & Astrophysics **96**, 142

Demorest, P. B., Pennucci, T., Ransom, S. M., Roberts, M. S. E., and Hessels, J. W. T.: 2010, Nature **467**, 1081

Dick, S.: 2013, Discovery and Classification in Astronomy: Controversy and Consensus, Cambridge University Press

Duchêne, G. and Kraus, A.: 2013, Annual Review of Astronomy and Astrophysics **51**, 269

Duquennoy, A. and Mayor, M.: 1991, Astronomy & Astrophysics **248**, 485

Edwards, D. A. and Pringle, J. E.: 1987, Monthly Notices of the Royal Astronomical Society **229**, 383

Eggleton, P.: 2011, Evolutionary Processes in Binary and Multiple Stars

Eggleton, P. P.: 1983, The Astrophysical Journal **268**, 368

Eldridge, J. J., Fraser, M., Maund, J. R., and Smartt, S. J.: 2015, Monthly Notices of the Royal Astronomical Society **446**, 2689

Eldridge, J. J., Izzard, R. G., and Tout, C. A.: 2008, Monthly Notices of the Royal Astronomical Society **384**, 1109

Eldridge, J. J. and Maund, J. R.: 2016, Monthly Notices of the Royal Astronomical Society **461**, L117

Elias, J. H., Matthews, K., Neugebauer, G., and Persson, S. E.: 1985, The Astrophysical Journal **296**, 379

Ensman, L. and Woosley, S. E.: 1987, in Bulletin of the American Astronomical Society, Vol. 19 of Bulletin of the American Astronomical Society, p. 757

Eyer, L., Holl, B., Pourbaix, D., Mowlavi, N., Siopis, C., Barblan, F., Evans, D. W., and North, P.: 2013, Central European Astrophysical Bulletin **37**, 115

Federrath, C.: 2016, Monthly Notices of the Royal Astronomical Society **457**, 375

Fedorenko, R.: 1962, USSR Computational Mathematics and Mathematical Physics **1(4)**, 1092

Filippenko, A. V.: 1988, The Astronomical Journal **96**, 1941

Filippenko, A. V.: 1997, Annual Review of Astronomy and Astrophysics **35**, 309

Folatelli, G., Van Dyk, S. D., Kuncarayakti, H., Maeda, K., Bersten, M. C., Nomoto, K., Pignata, G., Hamuy, M., Quimby, R. M., Zheng, W., Filippenko, A. V., Clubb, K. I., Smith, N., Elias-Rosa, N., Foley, R. J., and Miller, A. A.: 2016, The Astrophysical Journal Letters **825**, L22

Foley, R. J., Challis, P. J., Chornock, R., Ganeshalingam, M., Li, W., Marion, G. H., Morrell, N. I., Pignata, G., Stritzinger, M. D., Silverman, J. M., Wang, X., Anderson, J. P., Filippenko, A. V., Freedman, W. L., Hamuy, M., Jha, S. W., Kirshner, R. P., McCully, C., Persson, S. E., Phillips, M. M., Reichart, D. E., and Soderberg, A. M.: 2013, The Astrophysical Journal **767**, 57

Fox, O. D., Azalee Bostroem, K., Van Dyk, S. D., Filippenko, A. V., Fransson, C., Matheson, T., Cenko, S. B., Chandra, P., Dwarkadas, V., Li, W., Parker, A. H., and Smith, N.: 2014, The Astrophysical Journal **790**, 17

Fremling, C., Sollerman, J., Taddia, F., Ergon, M., Fraser, M., Karamehmetoglu, E., Valenti, S., Jerkstrand, A., Arcavi, I., Bufano, F., Elias Rosa, N., Filippenko, A. V., Fox, D., Gal-Yam, A., Howell, D. A., Kotak, R., Mazzali, P., Milisavljevic, D., Nugent, P. E., Nyholm, A., Pian, E., and Smartt, S.: 2016, Astronomy & Astrophysics **593**, A68

Fremling, C., Sollerman, J., Taddia, F., Ergon, M., Valenti, S., Arcavi, I., Ben-Ami, S., Cao, Y., Cenko, S. B., Filippenko, A. V., Gal-Yam, A., and Howell, D. A.: 2014, Astronomy & Astrophysics **565**, A114

Fryxell, B. A. and Arnett, W. D.: 1981, The Astrophysical Journal **243**, 994

Fuhrmann, K. and Chini, R.: 2015, The Astrophysical Journal **809**, 107

Gaia Collaboration: 2016, ArXiv e-prints

Gal-Yam, A.: 2012, Science **337**, 927

Garcia, E. V., Dupuy, T. J., Allers, K. N., Liu, M. C., and Deacon, N. R.: 2015, The Astrophysical Journal **804**, 65

Ge, H., Hjellming, M. S., Webbink, R. F., Chen, X., and Han, Z.: 2010, The Astrophysical Journal **717**, 724

Geldzahler, B. J., Pauls, T., and Salter, C. J.: 1980, Astronomy & Astrophysics **84**, 237

Goodwin, S. P.: 2013, Monthly Notices of the Royal Astronomical Society **430**, L6

Goodwin, S. P., Kroupa, P., Goodman, A., and Burkert, A.: 2007, Protostars and Planets V pp 133–147

Groh, J. H., Georgy, C., and Ekström, S.: 2013, Astronomy & Astrophysics **558**, L1

Gustafson, K.: 1998, Contemporary Mathematics **218**, 432

Hall, P. D. and Tout, C. A.: 2014, Monthly Notices of the Royal Astronomical Society **444**, 3209

Hanke, F., Müller, B., Wongwathanarat, A., Marek, A., and Janka, H.-T.: 2013, The Astrophysical Journal **770**, 66

Hayashi, C.: 1961, Publications of the Astronomical Society of Japan 13

Herschel, W.: 1802, Philosophical Transactions of the Royal Society of London Series I **92**, 477

Hestenes, M. R. and Stiefel, E.: 1952, Journal of Research of the National Bureau of Standards **49(6)**, 409

Hirai, R., Sawai, H., and Yamada, S.: 2014, The Astrophysical Journal **792**, 66

Hirai, R. and Yamada, S.: 2015, The Astrophysical Journal **805**, 170

Hirano, S., Zhu, N., Yoshida, N., Spergel, D., and Yorke, H. W.: 2015, The Astrophysical Journal **814**, 18

Horn, J.: 1971, Bulletin of the Astronomical Institutes of Czechoslovakia **22**, 37

Hosokawa, T., Hirano, S., Kuiper, R., Yorke, H. W., Omukai, K., and Yoshida, N.: 2015, ArXiv e-prints

Huang, J. and Greengard, L.: 1999, SIAM Journal on Scientific Computing **21(4)**, 1551

Hulse, R. A. and Taylor, J. H.: 1975, The Astrophysical Journal Letters **195**, L51

Hurley, J. R., Tout, C. A., and Pols, O. R.: 2002, Monthly Notices of the Royal Astronomical Society **329**, 897

Hut, P.: 1980, Astronomy & Astrophysics **92**, 167

Iaconi, R., Reichardt, T., Staff, J., De Marco, O., Passy, J.-C., Price, D., Wurster, J., and Herwig, F.: 2016, Monthly Notices of the Royal Astronomical Society

Iben, Jr., I. and Tutukov, A. V.: 1984, The Astrophysical Journal **284**, 719

Illenseer, T. F. and Duschl, W. J.: 2015, Monthly Notices of the Royal Astronomical Society **450**, 691

Ivanova, N.: 2011, The Astrophysical Journal **730**, 76

Ivanova, N., Justham, S., Avendano Nandez, J. L., and Lombardi, J. C.: 2013a, Science **339**, 433

Ivanova, N., Justham, S., Chen, X., De Marco, O., Fryer, C. L., Gaburov, E., Ge, H., Glebbeek, E., Han, Z., Li, X.-D., Lu, G., Marsh, T., Podsiadlowski, P., Potter, A., Soker, N., Taam, R., Tauris, T. M., van den Heuvel, E. P. J., and Webbink, R. F.: 2013b, The Astronomy and Astrophysics Review **21**, 59

Jackson, J. D.: 1999, Classical electrodynamics, Wiley

Janson, M., Bergfors, C., Brandner, W., Kudryavtseva, N., Hormuth, F., Hippler, S., and Henning, T.: 2014, The Astrophysical Journal **789**, 102

Janson, M., Hormuth, F., Bergfors, C., Brandner, W., Hippler, S., Daemgen, S., Kudryavtseva, N., Schmalzl, E., Schnupp, C., and Henning, T.: 2012, The Astrophysical Journal **754**, 44

Jerkstrand, A., Ergon, M., Smartt, S. J., Fransson, C., Sollerman, J., Taubenberger, S., Bersten, M., and Spyromilio, J.: 2015, Astronomy & Astrophysics **573**, A12

Jones, S., Hirschi, R., Pignatari, M., Heger, A., Georgy, C., Nishimura, N., Fryer, C., and Herwig, F.: 2015, Monthly Notices of the Royal Astronomical Society **447**, 3115

Kalogera, V., Belczynski, K., Kim, C., O'Shaughnessy, R., and Willems, B.: 2007, Physics Reports **442**, 75

Kasen, D.: 2010, The Astrophysical Journal **708**, 1025

Kinugawa, T., Inayoshi, K., Hotokezaka, K., Nakauchi, D., and Nakamura, T.: 2014, Monthly Notices of the Royal Astronomical Society **442**, 2963

Kippenhahn, R. and Weigert, A.: 1967, Zeitschrift für Astrophysik **65**, 251

Kippenhahn, R. and Weigert, A.: 1990, Stellar Structure and Evolution

Kolb, U. and Ritter, H.: 1990, Astronomy & Astrophysics **236**, 385

Kopal, Z.: 1959, Close binary systems

Kouwenhoven, M. B. N., Brown, A. G. A., Portegies Zwart, S. F., and Kaper, L.: 2007, Astronomy & Astrophysics **474**, 77

Kouwenhoven, M. B. N., Brown, A. G. A., Zinnecker, H., Kaper, L., and Portegies Zwart, S. F.: 2005, Astronomy & Astrophysics **430**, 137

Kraus, A. L. and Hillenbrand, L. A.: 2007, The Astronomical Journal **134**, 2340

Krebs, J. and Hillebrandt, W.: 1983, A & A **128**, 411

Kruszewski, A.: 1966, Advances in Astronomy and Astrophysics, Vol. 4

Kuiper, R., Klahr, H., Beuther, H., and Henning, T.: 2010, The Astrophysical Journal **722**, 1556

Kuncarayakti, H., Maeda, K., Bersten, M. C., Folatelli, G., Morrell, N., Hsiao, E. Y., González-Gaitán, S., Anderson, J. P., Hamuy, M., de Jaeger, T., Gutiérrez, C. P., and Kawabata, K. S.: 2015, Astronomy & Astrophysics **579**, A95

Kurganov, A. and Tadmor, E.: 2000, Journal of Computational Physics **160**, 241

Lai, D., Rasio, F. A., and Shapiro, S. L.: 1993, The Astrophysical Journal Letters **406**, L63

Lauterborn, D.: 1970, Astronomy & Astrophysics **7**, 150

Law, N. M., Kulkarni, S. R., Dekany, R. G., Ofek, E. O., Quimby, R. M., Nugent, P. E., Surace, J., Grillmair, C. C., Bloom, J. S., Kasliwal, M. M., Bildsten, L., Brown, T., Cenko, S. B., Ciardi, D., Croner, E., Djorgovski, S. G., van Eyken, J., Filippenko, A. V., Fox, D. B., Gal-Yam, A., Hale, D., Hamam, N., Helou, G., Henning, J., Howell, D. A., Jacobsen, J., Laher, R., Mattingly, S., McKenna, D., Pickles, A., Poznanski, D., Rahmer, G., Rau, A., Rosing, W., Shara, M., Smith, R., Starr, D., Sullivan, M., Velur, V., Walters, R., and Zolkower, J.: 2009, Publications of the Astronomical Society of Pacific **121**, 1395

Limongi, M. and Chieffi, A.: 2003, The Astrophysical Journal **592**, 404

Liu, Z.-W., Kromer, M., Fink, M., Pakmor, R., Röpke, F. K., Chen, X. F., Wang, B., and Han, Z. W.: 2013a, The Astrophysical Journal **778**, 121

Liu, Z.-W., Pakmor, R., Seitenzahl, I. R., Hillebrandt, W., Kromer, M., Röpke, F. K., Edelmann, P., Taubenberger, S., Maeda, K., Wang, B., and Han, Z. W.: 2013b, The Astrophysical Journal **774**, 37

Livne, E., Tuchman, Y., and Wheeler, J. C.: 1992, The Astrophysical Journal **399**, 665

Lubow, S. H. and Shu, F. H.: 1975, The Astrophysical Journal **198**, 383

MacLeod, M., Macias, P., Ramirez-Ruiz, E., Grindlay, J., Batta, A., and Montes, G.: 2016, ArXiv e-prints

MacLeod, M. and Ramirez-Ruiz, E.: 2015, The Astrophysical Journal Letters **798**, L19

Maeda, K., Hattori, T., Milisavljevic, D., Folatelli, G., Drout, M. R., Kuncarayakti, H., Margutti, R., Kamble, A., Soderberg, A., Tanaka, M., Kawabata, M., Kawabata, K. S., Yamanaka, M., Nomoto, K., Kim, J. H., Simon, J. D., Phillips, M. M., Parrent, J., Nakaoka, T., Moriya, T. J., Suzuki, A., Takaki, K., Ishigaki, M., Sakon, I., Tajitsu, A., and Iye, M.: 2015, The Astrophysical Journal **807**, 35

Maeder, A.: 1981, Astronomy & Astrophysics **99**, 97

Mandel, I. and de Mink, S. E.: 2016, Monthly Notices of the Royal Astronomical Society

Marchant, P., Langer, N., Podsiadlowski, P., Tauris, T. M., and Moriya, T. J.: 2016, Astronomy & Astrophysics **588**, A50

Marietta, E., Burrows, A., and Fryxell, B.: 2000, The Astrophysical Journal Supplement Series **128**, 615

Matsumoto, T. and Hanawa, T.: 2003, The Astrophysical Journal **583(1)**, 296

Maund, J. R., Reilly, E., and Mattila, S.: 2014, Monthly Notices of the Royal Astronomical Society **438**, 938

Maund, J. R., Smartt, S. J., Kudritzki, R. P., Podsiadlowski, P., and Gilmore, G. F.: 2004, Nature **427**, 129

Meyer, F. and Meyer-Hofmeister, E.: 1983, Astronomy & Astrophysics **121**, 29

Michell, J.: 1767, Philosophical transactions **57**, 234

Minkowski, R.: 1941, Publications of the Astronomical Society of the Pacific **53**, 224

Misner, C. W., Thorne, K. S., and Wheeler, J. A.: 1973, Gravitation, Macmillan

Miyoshi, T. and Kusano, K.: 2005, J. Comput. Phys. **208**, 315

Morton, D. C.: 1960, The Astrophysical Journal **132**, 146

Müller, E. and Steinmetz, M.: 1995, Comput. Phys. Commun. **89**, 45

Nagakura, H.: 2013, The Astrophysical Journal **764**, 139

Nandez, J. L. A., Ivanova, N., and Lombardi, Jr., J. C.: 2014, The Astrophysical Journal **786**, 39

Nomoto, K.: 1982, The Astrophysical Journal **253**, 798

Nomoto, K., Hashimoto, M., Tsujimoto, T., Thielemann, F.-K., Kishimoto, N., Kubo, Y., and Nakasato, N.: 1997, Nuclear Physics A **616**, 79

Ohlmann, S. T., Röpke, F. K., Pakmor, R., and Springel, V.: 2016a, ApJL **816**, L9

Ohlmann, S. T., Röpke, F. K., Pakmor, R., Springel, V., and Müller, E.: 2016b, Monthly Notices of the Royal Astronomical Society **462**, L121

O'Leary, R. M., Meiron, Y., and Kocsis, B.: 2016, arXiv:1602.02809

Paczyński, B.: 1966, Acta Astronomica **16**, 231

Paczyński, B.: 1971, Annual Review of Astronomy and Astrophysics **9**, 183

Paczyński, B. and Sienkiewicz, R.: 1972, Acta Astronomica **22**, 73

Pan, K.-C., Ricker, P. M., and Taam, R. E.: 2010, The Astrophysical Journal **715**, 78

Pan, K.-C., Ricker, P. M., and Taam, R. E.: 2012, The Astrophysical Journal **760**, 21

Pan, K.-C., Ricker, P. M., and Taam, R. E.: 2013, The Astrophysical Journal **773**, 49

Passy, J.-C., De Marco, O., Fryer, C. L., Herwig, F., Diehl, S., Oishi, J. S., Mac Low, M.-M., Bryan, G. L., and Rockefeller, G.: 2012, The Astrophysical Journal **744**, 52

Pastorello, A., Mattila, S., Zampieri, L., Della Valle, M., Smartt, S. J., Valenti, S., Agnoletto, I., Benetti, S., Benn, C. R., Branch, D., Cappellaro, E., Dennefeld, M., Eldridge, J. J., Gal-Yam, A., Harutyunyan, A., Hunter, I., Kjeldsen, H., Lipkin, Y., Mazzali, P. A., Milne, P., Navasardyan, H., Ofek, E. O., Pian, E., Shemmer, O., Spiro, S., Stathakis, R. A., Taubenberger, S., Turatto, M., and Yamaoka, H.: 2008, Monthly Notices of the Royal Astronomical Society **389**, 113

Pastorello, A., Smartt, S. J., Mattila, S., Eldridge, J. J., Young, D., Itagaki, K., Yamaoka, H., Navasardyan, H., Valenti, S., Patat, F., Agnoletto, I., Augusteijn, T., Benetti, S., Cappellaro, E., Boles, T., Bonnet-Bidaud, J.-M., Botticella, M. T., Bufano, F., Cao, C., Deng, J., Dennefeld, M., Elias-Rosa, N., Harutyunyan, A., Keenan, F. P., Iijima, T., Lorenzi, V., Mazzali, P. A., Meng, X., Nakano, S., Nielsen, T. B., Smoker, J. V., Stanishev, V., Turatto, M., Xu, D., and Zampieri, L.: 2007, Nature **447**, 829

Paxton, B., Bildsten, L., Dotter, A., Herwig, F., Lesaffre, P., and Timmes, F.: 2011, The Astrophysical Journal Supplement Series **192**, 3

Paxton, B., Cantiello, M., Arras, P., Bildsten, L., Brown, E. F., Dotter, A., Mankovich, C., Montgomery, M. H., Stello, D., Timmes, F. X., and Townsend, R.: 2013, The Astrophysical Journal Supplement Series **208**, 4

Paxton, B., Marchant, P., Schwab, J., Bauer, E. B., Bildsten, L., Cantiello, M., Dessart, L., Farmer, R., Hu, H., Langer, N., Townsend, R. H. D., Townsley, D. M., and Timmes, F. X.: 2015, The Astrophysical Journal Supplement Series **220**, 15

Petrie, R. M.: 1960, Annales d'Astrophysique **23**, 744

Pijloo, J. T., Caputo, D. P., and Portegies Zwart, S. F.: 2012, Monthly Notices of the Royal Astronomical Society **424**, 2914

Plavec, M., Ulrich, R. K., and Polidan, R. S.: 1973, Publications of the Astronomical Society of the Pacific **85**, 769

Podsiadlowski, P.: 2003, ArXiv Astrophysics e-prints

Podsiadlowski, P., Joss, P. C., and Hsu, J. J. L.: 1992, The Astrophysical Journal **391**, 246

Podsiadlowski, P., Langer, N., Poelarends, A. J. T., Rappaport, S., Heger, A., and Pfahl, E.: 2004, The Astrophysical Journal **612**, 1044

Portegies Zwart, S. F. and McMillan, S. L. W.: 2000, The Astrophysical Journal Letters **528**, L17

Poveda, A., Allen, C., and Parrao, L.: 1982, The Astrophysical Journal **258**, 589

Raghavan, D., McAlister, H. A., Henry, T. J., Latham, D. W., Marcy, G. W., Mason, B. D., Gies, D. R., White, R. J., and ten Brummelaar, T. A.: 2010, The Astrophysical Journal Supplement Series **190**, 1

Rauscher, T., Heger, A., Hoffman, R. D., and Woosley, S. E.: 2002, The Astrophysical Journal **576**, 323

Ricker, P. M.: 2008, The Astrophysical Journal Supplement Series **176(1)**, 293

Ricker, P. M. and Taam, R. E.: 2012, The Astrophysical Journal **746**, 74

Ritter, H.: 1988, Astronomy & Astrophysics **202**, 93

Robert, Y.: 1982, Linear Algebra and its Applications **48**, 105

Roche, É.: 1873, Essai sur la constitution et l'origine du système solaire, Vol. 8 of Mèmoires de l'Acadèmie des sciences et lettres de Montpellier, p. 235

Saijo, M. and Kojima, Y.: 2008, Physical Review D **77(6)**, 063002

Sana, H., de Mink, S. E., de Koter, A., Langer, N., Evans, C. J., Gieles, M., Gosset, E., Izzard, R. G., Le Bouquin, J.-B., and Schneider, F. R. N.: 2012, Science **337**, 444

Sana, H., Le Bouquin, J.-B., Lacour, S., Berger, J.-P., Duvert, G., Gauchet, L., Norris, B., Olofsson, J., Pickel, D., Zins, G., Absil, O., de Koter, A., Kratter, K., Schnurr, O., and Zinnecker, H.: 2014, The Astrophysical Journal Supplement Series **215**, 15

Sato, Y., Nakasato, N., Tanikawa, A., Nomoto, K., Maeda, K., and Hachisu, I.: 2015, The Astrophysical Journal **807**, 105

Savonije, G. J.: 1978, Astronomy & Astrophysics **62**, 317

Sawai, H. and Yamada, S.: 2016, The Astrophysical Journal **817**, 153

Sawai, H., Yamada, S., Kotake, K., and Suzuki, H.: 2013, The Astrophysical Journal **764**, 10

Schlafly, E. F. and Finkbeiner, D. P.: 2011, The Astrophysical Journal **737**, 103

Schlegel, E. M.: 1990, Monthly Notices of the Royal Astronomical Society **244**, 269

Seward, F. D., Charles, P. A., Foster, D. L., Dickel, J. R., Romero, P. S., Edwards, Z. I., Perry, M., and Williams, R. M.: 2012, The Astrophysical Journal **759**, 123

Shappee, B. J., Kochanek, C. S., and Stanek, K. Z.: 2013, The Astrophysical Journal **765**, 150

Sköllermo, G.: 1975, Mathematics of Computation **29(131)**, 697

Smith, N. and Arnett, W. D.: 2014, The Astrophysical Journal **785**, 82

Smith, N., Li, W., Filippenko, A. V., and Chornock, R.: 2011, Monthly Notices of the Royal Astronomical Society **412**, 1522

Soberman, G. E., Phinney, E. S., and van den Heuvel, E. P. J.: 1997, Astronomy & Astrophysics **327**, 620

Srivastav, S., Anupama, G. C., and Sahu, D. K.: 2014, Monthly Notices of the Royal Astronomical Society **445**, 1932

Sukhbold, T. and Woosley, S. E.: 2014, The Astrophysical Journal **783**, 10

Takahashi, K., Yamada, S., and Yamada: 2014, Journal of Plasma Physics **80**, 255

Thorne, K. S. and Zytkow, A. N.: 1977, The Astrophysical Journal **212**, 832

Tokovinin, A.: 2014, The Astronomical Journal **147**, 87

Tokovinin, A. A.: 1997, A & A Supplements Series **124**, 75

Tomida, K., Okuzumi, S., and Machida, M. N.: 2015, The Astrophysical Journal **801**, 117

Tout, C. A., Aarseth, S. J., Pols, O. R., and Eggleton, P. P.: 1997, Monthly Notices of the Royal Astronomical Society **291**, 732

Tully, R. B., Courtois, H. M., Dolphin, A. E., Fisher, J. R., Héraudeau, P., Jacobs, B. A., Karachentsev, I. D., Makarov, D., Makarova, L., Mitronova, S., Rizzi, L., Shaya, E. J., Sorce, J. G., and Wu, P.-F.: 2013, The Astronomical Journal **146**, 86

Tully, R. B., Rizzi, L., Shaya, E. J., Courtois, H. M., Makarov, D. I., and Jacobs, B. A.: 2009, The Astronomical Jounal **138**, 323

van den Heuvel, E. P. J.: 1976, in P. Eggleton, S. Mitton, and J. Whelan (eds.), Structure and Evolution of Close Binary Systems, Vol. 73 of IAU Symposium, p. 35

van der Vorst, H. A.: 1992, SIAM J. Sci. Stat. Comput. **13(2)**, 631

van Leer, B.: 1979, Journal of Computational Physics **32**, 101

Vanbeveren, D., Mennekens, N., and De Greve, J. P.: 2012, Astronomy & Astrophysics **543**, A4

Wang, C., Jia, K., and Li, X.-D.: 2016, Research in Astronomy and Astrophysics **16**, 126

Ward-Duong, K., Patience, J., De Rosa, R. J., Bulger, J., Rajan, A., Goodwin, S. P., Parker, R. J., McCarthy, D. W., and Kulesa, C.: 2015, Monthly Notices of the Royal Astronomical Society **449**, 2618

Webbink, R. F.: 1984, The Astrophysical Journal **277**, 355

Webbink, R. F.: 1985, Stellar evolution and binaries, p. 39

Wellstein, S. and Langer, N.: 1999, Astronomy & Astrophysics **350**, 148

Wheeler, J. C. and Harkness, R. P.: 1986, in B. F. Madore and R. B. Tully (eds.), NATO Advanced Science Institutes (ASI) Series C, Vol. 180 of NATO Advanced Science Institutes (ASI) Series C, pp 45–54

Wheeler, J. C., Harkness, R. P., Barker, E. S., Cochran, A. L., and Wills, D.: 1987, The Astrophysical Journal Letters **313**, L69

Wheeler, J. C., Lecar, M., and McKee, C. F.: 1975, The Astrophysical Journal **200**, 145

Wheeler, J. C. and Levreault, R.: 1985, The Astrophysical Journal Letters **294**, L17

Woosley, S. E. and Heger, A.: 2007, Physics Reports **442**, 269

Woosley, S. E., Heger, A., and Weaver, T. A.: 2002, Reviews of Modern Physics **74**, 1015

Xu, X.-J. and Li, X.-D.: 2010, The Astrophysical Journal **716**, 114

Yoon, S.-C., Gräfener, G., Vink, J. S., Kozyreva, A., and Izzard, R. G.: 2012, Astronomy & Astrophysics **544**, L11

Young, D.: 1954, Transactions of the American Mathematical Society **76(1)**, 92

Young, P. A. and Fryer, C. L.: 2007, The Astrophysical Journal **664**, 1033

Ziółkowski, J.: 1969, Astrophysics and Space Science **3**, 14

早稲田大学　博士（理学）　学位申請　研究業績書

（2017 年　1 月　現在）

種 類 別	題名、　発表・発行掲載誌名、　発表・発行年月、　連名者（申請者含む）
論文	Title：○Formation Scenario of the Progenitor of iPTF13bvn Revisited Journal：Monthly Notices of the Royal Astronomical Society, Volume 466, Issue 4, p.3775 Publication date：January, 2017 Authors：Ryosuke Hirai
	Title：Hyperbolic self-gravity solver for large scale hydrodynamical simulations Journal：Physical Review D, Volume 93, Issue 8, id.083006 Publication date：April, 2016 Authors：Ryosuke Hirai, Hiroki Nagakura, Hirotada Okawa & Kotaro Fujisawa
	Title：○Possible Signatures of Ejecta-Companion Interaction in iPTF 13bvn Journal：The Astrophysical Journal, Volume 805, article id. 170, 7 pp. Publication date：June, 2015 Authors：Ryosuke Hirai & Shoichi Yamada
	Title：○The Outcome of Supernovae in Massive Binaries; Removed Mass, and its Separation Dependence Journal：The Astrophysical Journal, Volume 792, article id. 66, 15 pp. Publication date：September, 2014 Authors：Ryosuke Hirai, Hidetomo Sawai & Shoichi Yamada
講演 （口頭）	Title：Revisiting the Formation Scenario of the Progenitor of iPTF13bvn Conference：International Molecule-type Workshop "Transient Universe in the Big Survey Era: Understanding the Nature of Astrophysical Explosive Phenomena" Date：January, 2017 Authors：Ryosuke Hirai
	Title：iPTF13bvn の連星親星モデル Conference：第 29 回理論懇シンポジウム Date：December, 2016 Authors：Ryosuke Hirai
	Title：超新星 iPTF13bvn の連星親星モデル Conference：連星系・変光星・低温度星研究会 2016 Date：October, 2016 Authors：Ryosuke Hirai
	Title：流体力学シミュレーションにおける高速自己重力計算手法の提案 Conference：日本天文学会秋季年会 2016 Date：September, 2016 Authors：Ryosuke Hirai, Hiroki Nagakura, Hirotada Okawa, Kotaro Fujisawa

早稲田大学　博士（理学）　学位申請　研究業績書

種類別	題名、　発表・発行掲載誌名、　発表・発行年月、　連名者（申請者含む）
	Title：Lessons on binary star evolution from iPTF13bvn Conference：2nd NAOJ-ECT* Workshop on "Many Riddles About Core-Collapse Supernovae: 1 Bethe and Beyond" (MRACCS) Date：June-July, 2016 Authors：Ryosuke Hirai Title：Towards the Formation of Binary Neutron Stars Conference：Numazu Workshop 2015: Challenges of modeling supernovae with nuclear data Date：September, 2015 Authors：Ryosuke Hirai Title：Ejecta-Companion interaction in iPTF 13bvn Conference：F.O.E. Fifty-One Erg Date：June, 2015 Authors：Ryosuke Hirai & Shoichi Yamada Title：超新星爆発前後での連星系の生存可能性 Conference：日本天文学会春季年会 2015 Date：March, 2015 Authors：Ryosuke Hirai, Hidetomo Sawai & Shoichi Yamada Title：中性子星連星の形成に向けた超新星爆発後の連星系の生存可能性 Conference：新学術領域 A04/05 班合同合宿 Date：January, 2015 Authors：Ryosuke Hirai & Shoichi Yamada Title：大質量連星系内での超新星爆発 Conference：第 2 回 DTA シンポジウム Date：October, 2014 Authors：Ryosuke Hirai Title：大質量連星系内での超新星爆発が伴星に与える影響とそのパラメータ依存性 Conference：日本天文学会秋季年会 2014 Date：September, 2014 Authors：Ryosuke Hirai, Hidetomo Sawai & Shoichi Yamada Title：大質量連星系における超新星爆発とその伴星への影響 Conference：第 44 回　天文・天体物理若手　夏の学校 Date：July, 2014 Authors：Ryosuke Hirai Title：連星系中の超新星爆発が伴星に与える影響 Conference：連星天文学研究会 Date：February, 2014 Authors：Ryosuke Hirai, Hidetomo Sawai & Shoichi Yamada

早稲田大学　博士（理学）　学位申請　研究業績書

種 類 別	題名、　発表・発行掲載誌名、　発表・発行年月、　連名者（申請者含む）
	Title：大質量連星系における超新星爆発が伴星に与える影響 Conference：日本天文学会秋季年会 2013 Date：September, 2013 Authors：Ryosuke Hirai, Hidetomo Sawai & Shoichi Yamada Title：大質量連星系における超新星爆発が伴星に与える影響 Conference：第 43 回 天文・天体物理若手　夏の学校 Date：July, 2013 Authors：Ryosuke Hirai, Hidetomo Sawai & Shoichi Yamada Title：連星系中の超新星爆発 Conference：第 42 回 天文・天体物理若手　夏の学校 Date：August, 2012 Authors：Ryosuke Hirai, Hidetomo Sawai & Shoichi Yamada
講演 （ポスター）	Title：自己重力流体シミュレーションにおける高速自己重力計算手法 Conference：第 46 回 天文・天体物理若手　夏の学校 Date：July, 2016 Authors：Ryosuke Hirai, Hiroki Nagakura, Hirotada Okawa & Kotaro Fujisawa Title：超新星爆発によって共通外層状態が誘発される可能性について Conference：第 28 回理論懇シンポジウム Date：December, 2015 Authors：Ryosuke Hirai, Tomoya Kinugawa & Shoichi Yamada Title：iPTF 13bvn における伴星の観測的特徴 Conference：第 27 回理論懇シンポジウム Date：December, 2014 Authors：Ryosuke Hirai & Shoichi Yamada Title：Supernovae in Massive Binaries and their Impact on the Companion Conference：Binary systems, their evolution and environments Date：September, 2014 Authors：Ryosuke Hirai, Hidetomo Sawai & Shoichi Yamada Title：Supernovae in Massive Binaries and its Impact on the Companion Conference：Multi-Messengers from Core-Collapse Supernovae(MMCOCOS) Date：December, 2013 Authors：Ryosuke Hirai, Hidetomo Sawai & Shoichi Yamada

早稲田大学　博士（理学）　学位申請　研究業績書

種 類 別	題名、　発表・発行掲載誌名、　発表・発行年月、　連名者（申請者含む）
その他 （セミナー）	Title：Hyperbolic Self-Gravity Solver and Beyond Seminar：京都大学宇宙物理学教室セミナー Date：July, 2016 Authors：Ryosuke Hirai Title：大質量連星系内の超新星爆発が伴星へ与える影響とその観測可能性 Seminar：東京大学茂山研究室セミナー Date：January, 2016 Authors：Ryosuke Hirai Title：Ejecta-Companion Interaction in Massive Star Binaries Seminar：KEK Theory Seminar Date：July, 2015 Authors：Ryosuke Hirai Title：大質量連星系内の超新星爆発が伴星へ与える影響とその観測可能性 Seminar：京都大学天体核物理学教室コロキウム Date：June, 2015 Authors：Ryosuke Hirai Title：大質量連星系内の超新星爆発が伴星へ与える影響とその観測可能性 Seminar：京都大学宇宙物理学教室セミナー Date：June, 2015 Authors：Ryosuke Hirai Title：Supernovae in Massive Binaries and its Impact on the Companion Seminar：理化学研究所天体ビッグバン研究室セミナー Date：April, 2014 Authors：Ryosuke Hirai
その他 （講演）	Title：大質量連星系内での超新星爆発によって熱された伴星が引き起こす様々な現象 Event：2015 年度 若手研究者研究成果報告会　理工研シンポジウム Date：March, 2016 Authors：Ryosuke Hirai Title：宇宙物理学とその応用　～他分野との共同研究に向けて～ Event：理工総研アーリーバードプログラム 2015 年度第一回バードミーティング Date：June, 2015 Authors：Ryosuke Hirai Title：連星系と超新星爆発 Event：早稲田大学系属早稲田実業学校 課外特別授業 第一回早実 OB･OG 大学院生講義 Date：June, 2015 Authors：Ryosuke Hirai